DEVICES: COMMERCIAL USE O

Annual Report

to

Aeronautics and Space Administration
Langley Research Center
Hampton, VA 23665-5225

July 3, 1991 - July 2, 1992

Gene Haertling

-Shiung Hsi
Shang Li

August

Department of Ceram
College of Engineering

SUPERCONDUCTIVITY DEVICES: COMMERCIAL USE OF SPACE

Annual Report

to

National Aeronautics and Space Administration
Langley Research Center
Hampton, VA 23665-5225

Period: July 3, 1991 - July 2, 1992

Principal Investigator:
Gene Haertling

Supporting Investigators:
Chi-Shiung Hsi
Guang Li

Contract No. NAG-1-1301

August 28, 1992

CLEMSON
UNIVERSITY

Department of Ceramic Engineering
College of Engineering

I. Introduction

The high Tc (>95K) superconducting ceramic materials, initially developed in 1987, are now being extensively investigated for a variety of engineering applications. These applications include such devices as conducting links, rotating and linear bearings, sensors, filters, switches, high Q cavities, magnets and motors. Some of these devices take advantage of the material's ability to lose all electrical resistance at a critical temperature (Tc) while others make use of the repulsion forces generated between the magnetic field of a permanent magnet and a superconductor which is cooled below its Tc; i.e., the Meissner effect.

A device involving the first of these effects; i.e., the loss of resistance at the onset of superconductivity, has been under development at Clemson University under the sponsorship of NASA Langley for the last three years. Known as a low thermal conductivity superconducting grounding link for the SAFIRE program, this device has undergone a full year of real time testing and has shown promise of meeting some of the design specifications.

A companion device to the grounding link in the SAFIRE application is the data link between the detectors and the preamps. In contrast to the former device which is a single conductor, the data link consists of a large number of electrically isolated leads of very small cross section which are designed to carry an electrical signal yet keep the thermal losses to a bare minimum. This application is obviously more demanding from a technical standpoint than the grounding link because the technologies involved in processing and fabricating small, multiple-leaded devices is considerably more complicated. Much of the work reported in this annual work involves (1) the preparation and processing of the high temperature (105K) 2223 Bi-Sr-Ca-Cu-O phase in relatively pure form, (2) the development of suitable substrate materials for the BSCCO, (3) screen printing of both 2223 BSCCO and 123 YBCO materials on the substrates and (4) evaluation of the resulting superconducting properties.

In addition to this device, development is also being carried out on the development of solid-state electromechanical actuators which can be used in a number of applications in space such as cryopump motors, anti-vibration active structures and telescope mirror correctors. Considering any of these applications, the key to the successful development of a device is the successful development of a ceramic material which can produce maximum displacement per volt input. This is especially true of the cryocooler pump application where size, efficiency and reliability are of prime consideration. This report describes the work accomplished toward this goal in the first year; i.e., (1) a review of the present state of the art in actuator technology, (2) the fabrication and processing of high strain PBZT electrostrictive materials and (3) the testing and evaluation of these electrostrictive materials.

The report is divided into two parts with Part I dealing with the processing and screen printing of the superconducting BSCCO and 123 YBCO materials, and Part II reporting on the electromechanical actuator work.

Part I.

Annual Report

SUPERCONDUCTIVITY DEVICES: COMMERCIAL USE OF SPACE

Screen Printed Y and Bi-Based Superconductors

to

National Aeronautics and Space Administration
Langley Research Center
Hampton, VA 23665-5225

Principal Investigator:
Gene H. Haertling -Clemson University

Supporting Investigator:
Chi-Shiung Hsi -Clemson University

Contract No: NAG-1-1301

August, 1992

Abstract

High T_c superconducting thick film were prepared by a screen printing process. Y-based ($YBa_2Cu_3O_{7-x}$) superconducting thick films were printed on 211/ Al_2O_3, SNT/Al_2O_3, and YSZ substrates. Because of poor adhesion of the superconductor thick films to 211/ Al_2O_3 and SNT/Al_2O_3 substrates, relatively low T_c and J_c values were obtained from the films printed on these substrates. Critical temperatures (T_c) of $YBa_2Cu_3O_{7-x}$ thick films deposited on 211/ Al_2O_3 and SNT/Al_2O_3 substrates were about 80 K. The critical current densities (J_c) of these films were less than 2 A/cm^2. Higher T_c and J_c $YBa_2Cu_3O_{7-x}$ thick films were printed on YSZ substrates. A $YBa_2Cu_3O_{7-x}$ thick film with T_c=86.4 and J_c= 50.4 A/cm^2 was prepared by printing the film on YSZ substrate and firing at 990^{0}C for 10 minutes. Multiple-lead samples were also prepared on the YSZ substrates. The multiple-lead samples showed lower T_c and/ or J_c values than those of the plain samples.

The electrical properties of $YBa_2Cu_3O_{7-x}$ thick films were determined by the microstructures of the films. The $YBa_2Cu_3O_{7-x}$ thick films printed on the YSZ substrates, which had the best properties among the films printed on the three different kinds of substrates, had the highest density and the best particle interconnection. The $YBa_2Cu_3O_{7-x}$ thick films with preferred orientation in (001) direction were obtained on the YSZ substrates. Cracks, which retarded the properties of the films, were found from the films deposited on the YSZ substrates. Currently, a MSZ (Magnesium Stabilized Zirconia) substrate, which had higher thermal expansion coefficient than the YSZ substrate, is used as substrate for the $YBa_2Cu_3O_{7-x}$ thick film in order to eliminate the cracks on the film.

Bi-based superconductor thick films were printed on polycrystalline MgO and YSZ substrates. Interactions between BSCCO thick films and the YSZ substrates were observed. Various buffer layer materials were applied onto the substrates in order to avoid the interactions between the BSCCO thick films and the ZrO_2-based substrates. So far, A BSCCO printed on MgO substrate with T_c=89K was obtained. The J_c of the film was lower than 0.1 A/cm^2 by reason of poor interconnectivity of the BSCCO particles.

I. Introduction.

Among all the possible applications of high T_c superconductors, electric wiring, high information density data transmission lines, magnetic shielding, and hybrid technology will probably be the first high T_c components to be used. Sintering the high T_c superconductor with a large volume and area is necessary for these applications. Thick film technology, which can be applied under normal atmospheric conditions, is a promising method to achieve such components. Several thick film fabrication methods have recently been proposed and demonstrated, e.g., screen printing, molten oxide process, rapid quench method, tape casting , and spray pyrolysis.

A $YBa_2Cu_3O_{7-x}$ superconductor grounding link for an infrared detector on the SAFIRE program has been successfully developed by tape casting technology at Clemson University. In this application, the superconducting link provides a low noise, low thermal conductivity connection from the sensitive atmospheric detector at 4K and pre-amplifier at 80K. This serves to conserve the helium in space and will extend the life of mission. A companion device to the grounding link, in the SAFIRE program, is the data link between the detector and the pre-amplifier. The data link involves a large number of electrically isolated leads of very small cross section which are designed to reduce the thermal losses to a bare minimum. The screen printing method as mentioned above is considered to be the most practical thick film process to fabricate the data link, because it is relatively simple, easy to pattern, and a low cost technique.

Films which were deposited by the screen printing process had numerous problems, the most serious of which was poor superconductivity. The properties of the copper oxide superconducting films were highly sensitive to the substrate materials[1]. Random orientation of the crystallities and poor interconnectivity were considered to be the reasons for the low values of T_c and J_c of the films.

In this report, yittria-based and Bi-based superconducting thick films printed on various substrates are discussed according to the types of the superconductor materials used.

II. $YBa_2Cu_3O_{7-x}$ Thick Films.

II.1 Introduction.

$YBa_2Cu_3O_{7-x}$ superconductor thick films had been made on different substrates with T_c between 43 and 90 K, as listed in Appendix I. Figure 1 shows the variation of T_c values of the $YBa_2Cu_3O_{7-x}$ thick films on different substrates obtained from previous work[1-17] by other investigators. The films printed on Al_2O_3 based substrates, which included polycrystalline alumina and sapphire, showed lower T_c values and larger T_c variations. The films on alumina substrates had a higher relative magnetic susceptibility change than those on YSZ(Yttrium Stabilized Zirconia), MgO, 211 (Y_2BaCuO_5), and $SrTiO_3$ substrates[1]. This was due to the strong reaction between Al_2O_3 and the $YBa_2Cu_3O_{7-x}$ superconductor. The films printed on MgO and $SrTiO_3$ substrates also had large T_c variations. More consistent results, which had higher T_c values and smaller T_c value deviations, were obtained from the ZrO_2 based and 211 substrates. Ranking the substrates without a buffer layer, the best results from all of the reported literatures were on the ZrO_2 or 211 substrates, followed in order of increasing difficulty of preparation, MgO, spinel, $SrTiO_3$, Al_2O_3, and sapphire. Therefore, YSZ and 211 were used as substrate materials in this project. In order to compare the results on YSZ and 211 substrates, a new substrate made by $SrCO_3$, Nb_2O_5, and TiO_2 in the composition of $Sr_{0.875}(Ti_{0.75}Nb_{0.25})O_3$ was used as a substrate material in the project.

Cracks were found on $YBa_2Cu_3O_{7-x}$ superconductor thick films by Stastny[1]. This was due to the weak-link contact of the $YBa_2Cu_3O_{7-x}$ grains and thermal expansion mismatch between the $YBa_2Cu_3O_{7-x}$ thick film and substrates[1]. No or poor adhesion of the films were found when the films were printed on Al_2O_3 and YSZ substrates and fired at temperature below 950°C in O_2 atmosphere[3,13]. Adhesion between the $YBa_2Cu_3O_{7-x}$ thick film and the substrate was improved by adding Ag or Ag_2O to the superconductor[5,11]. Cracking was prevented when Ag was added to the $YBa_2Cu_3O_{7-x}$ thick films, owing to the strength imparted by the Ag[18]. Superconducting properties and

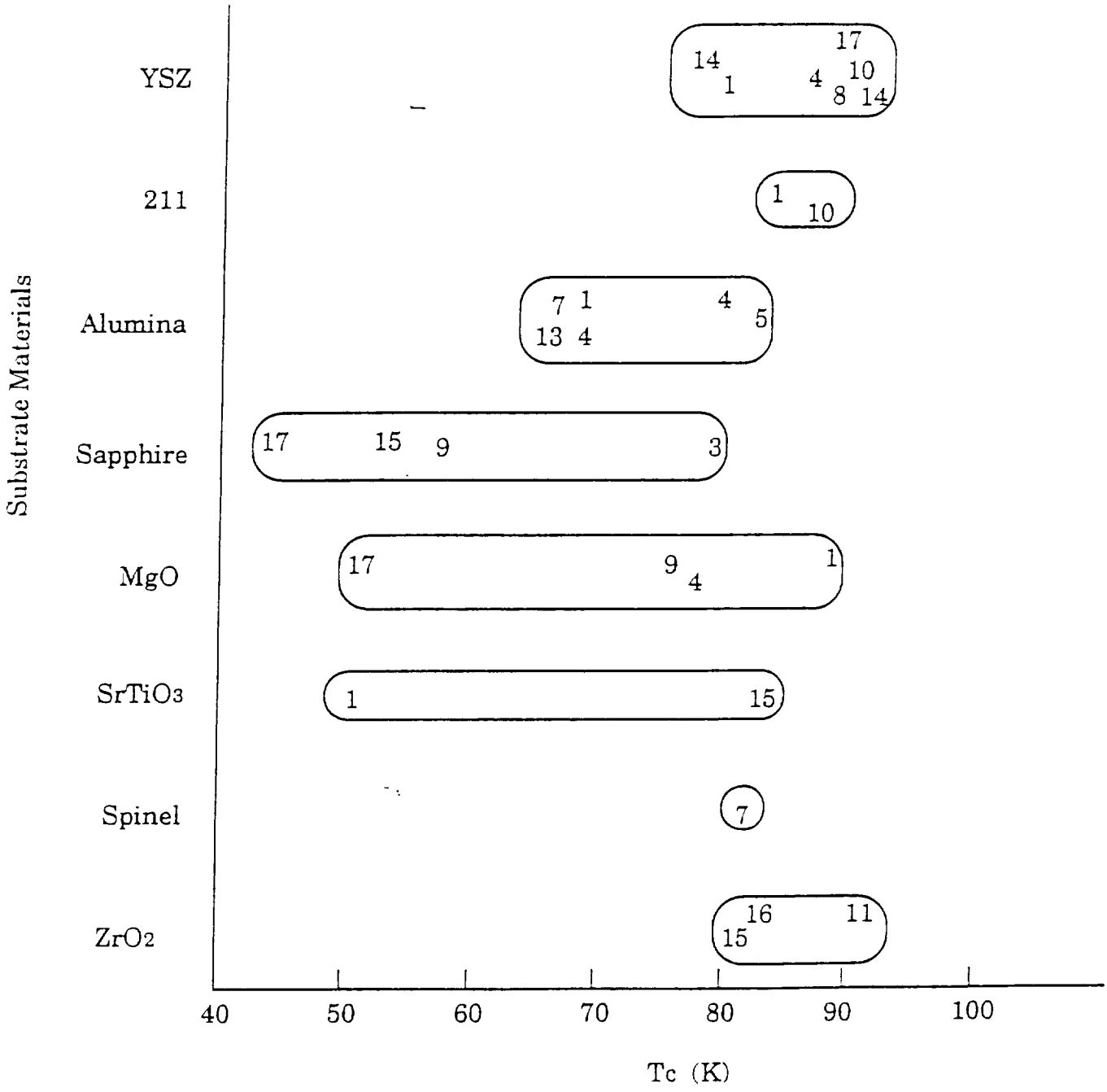

Figure 1: Variations of T_c value of $YBa_2Cu_3O_{7-x}$ superconductor thick films on different substrates. The numbers in the figure indicate the references used in this report.

density of the thick films were also enhanced by the Ag or Ag_2O addition[5,11,14]. In this project the $YBa_2Cu_3O_{7-x}$ thick films with different Ag_2O additions were prepared.

The properties of the $YBa_2Cu_3O_{7-x}$ thick films were also determined by the microstructures of the films. Superconducting $YBa_2Cu_3O_{7-x}$ thick films printed on YSZ substrates with (001) preferred orientation had been obtained by the melting process. The formation mechanism of the preferred orientation was caused by the interface reaction and established by Tabuchi et.al.[17], as shown in Appendix II. In this report, the influence of the films' microstructure to their electrical properties are also discussed.

II.2 Experimental Procedure.

Figure 2 shows the fabrication process of $YBa_2Cu_3O_{7-x}$ superconductor thick films.

The YSZ, 211, and SNT substrates were prepared by tape casting. Because 211 and SNT substrates showed higher tan ∂ and/or poor mechanical strength, a polycrystalline alumina substrate was used to support these substrates. The 211 and SNT tapes were wet with toluene to bond them to Al_2O_3 substrates. The 211 substrate was sintered at 1150°C for 4 hours, whereas the SNT substrate was sintered at 1270°C for 4 hours. After sintering, both the 211 and SNT exhibited good adhesion to the alumina substrates. The YSZ substrate, with 8 wt% Y_2O_3, was sintered at 1520°C for 5 hours.

The $YBa_2Cu_3O_{7-x}$ raw powder was prepared by an ordinary solid state reaction method. High purity Y_2O_3, $BaCO_3$, and CuO were wet mixed and then calcined at 900°C for 5 hours. The calcined powder was annealed at 450°C for 12 hours before it was cooled down to room temperature. This calcination process was repeated for three times. After calcining, $YBa_2Cu_3O_{7-x}$ powder was ground, and then mixed with 10 to 30 wt% Ag_2O. $YBa_2Cu_3O_{7-x}$ paste was prepared by mixing the powder with a liquid organic medium. Before the paste was prepared, any interactions between $YBa_2Cu_3O_{7-x}$ powder and the organic medium was

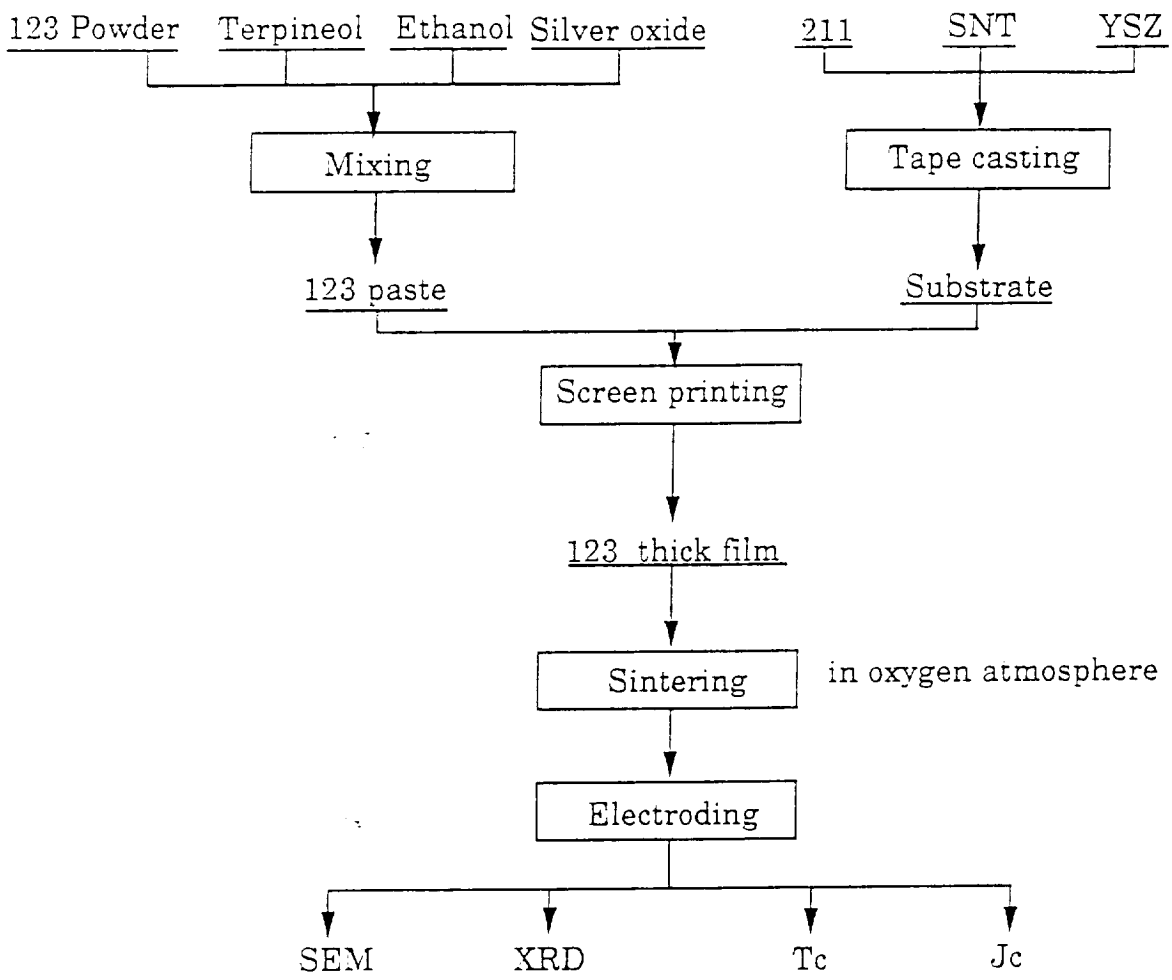

Figure 2: Fabrication process of $YBa_2Cu_3O_{7-x}$ superconductor thick films.

observed by a leaching test. In the test, 4 g of the powder was mixed with 4 g of a liquid organic medium. The mediums examined were propylene glycol, terpineol, ethanol, toluene, and trichloroethylene. After three days aging, propylene glycol became blue. This might be caused from the leaching of copper ions from the $YBa_2Cu_3O_{7-x}$ powder. However, trichloroethylene, toluene, ethanol, and terpineol remained clear. Therefore, terpineol, ethanol, and toluene were used as solvents in paste preparation. The $YBa_2Cu_3O_{7-x}$ paste was prepared by mixing the powder, terpineol, ethanol, and toluene in 30:5:1:1 ratios. In order to increase adhesion of the green film, 10 wt% of binder (Metoramic Science Inc., B73305), was added to the paste.

After the substrates and $YBa_2Cu_3O_{7-x}$ paste were prepared, the films were deposited on the substrates by printing the paste through a 200 mesh stainless steel screen. Two kinds of patterns, single and multi-lead, were printed on the substrates. The single sample size was 1 cm wide and 4 cm long. The multi-lead sample had 15 lines, as shown in Figure 3. The size of each line was 20 mils width and 1500 mils length. The space between each line was 20 mils. Films were sintered at 900 to 990°C for 5 minutes to 4 hours, in oxygen atmosphere. Electroding conditions, as determined in the previous project (Contract No. NAG-1-820), were used to apply the electrodes to the thick films.

Critical temperature of the sample showing zero resistance, T_c, was measured by the four-point method. The T_c of the single film was measured with a constant current of 1 mA. The multi-lead sample's T_c was measured at 100 μA current. The J_c of the films, both single and multi-lead type, were measured at 1 μV /cm level at 77K. Film thicknesses were measured by Tencor, Alpha-step 200. Microstructure of the $YBa_2Cu_3O_{7-x}$ thick film was observed by SEM (JEOL IC848). The crystal structure of the film was analyzed with a SCINTAG diffractometer.

II.3 Results and Discussions.

II.3.1 $YBa_2Cu_3O_{7-x}$ films printed on 211/Al_2O_3 and SNT/Al_2O_3 substrates.

$YBa_2Cu_3O_{7-x}$ thick films printed on 211/Al_2O_3 substrates showed poor adhesion to the substrates when they were fired at temperatures lower than

ORIGINAL PAGE
BLACK AND WHITE PHOTOGRAPH

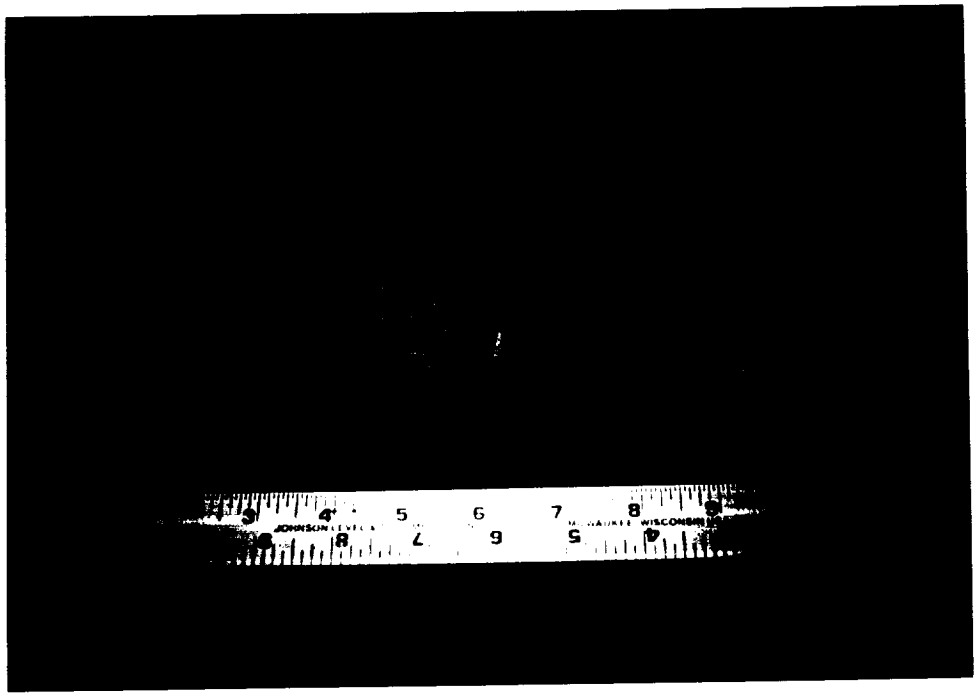

Figure 3: Multiple-lead $YBa_2Cu_3O_{7-x}$ superconductor samples (A), Sintered YSZ substrates (B), and YSZ green tapes (C).

940°C. The poor adhesion of the film printed on the $211/Al_2O_3$ substrate was due to high porosity of the substrate, as shown in Figure 4. Adding Ag_2O to the $YBa_2Cu_3O_{7-x}$ films improved their adhesion to the substrates. When 30 wt% Ag_2O was added to the films, the $YBa_2Cu_3O_{7-x}$ superconducting thick films with good adhesion to the $211/Al_2O_3$ substrates were obtained. The $YBa_2Cu_3O_{7-x}$ films showed zero resistance at 80K with 1 mA measuring current, as listed in Table 1. Figure 4 shows the microstructure of the $YBa_2Cu_3O_{7-x}$ thick film printed on $211/Al_2O_3$ substrate and fired at 920°C for 60 minutes. The film had a small grain size and high porosity. Poor linking between the $YBa_2Cu_3O_{7-x}$ particles was observed in this sample. Because of the weak links between the $YBa_2Cu_3O_{7-x}$ particles, the $YBa_2Cu_3O_{7-x}$ thick films printed on the $211/Al_2O_3$ substrates had much lower T_c and J_c values than those of $YBa_2Cu_3O_{7-x}$ pellet or tape. The $YBa_2Cu_3O_{7-x}$ thick film was composed of 211 green phase after being fired at temperature higher than 940°C, as shown in Figure 5.

Table 1: The preparation conditions and properties of $YBa_2Cu_3O_{7-x}$ screen printed thick films on $211/Al_2O_3$ and SNT/Al_2O_3 substrates.

Substrate	Sintering Temp.	Sintering Time	T_c(K)	J_c(A/cm^2)	Ag(%)
$211/Al_2O_3$	900°C	4 hours	~80	-	30
$211/Al_2O_3$	910°C	2 hours	~80	-	30
$211/Al_2O_3$	920°C	1 hours	80	0.2	30
$211/Al_2O_3$	920°C	2 hours	80	1.0	30
SNT/Al_2O_3	950°C	10 min.	80	-	20
SNT/Al_2O_3	950°C	20 min.	82.6	1.8	20
SNT/Al_2O_3	950°C	10 min.	80.9	1	20

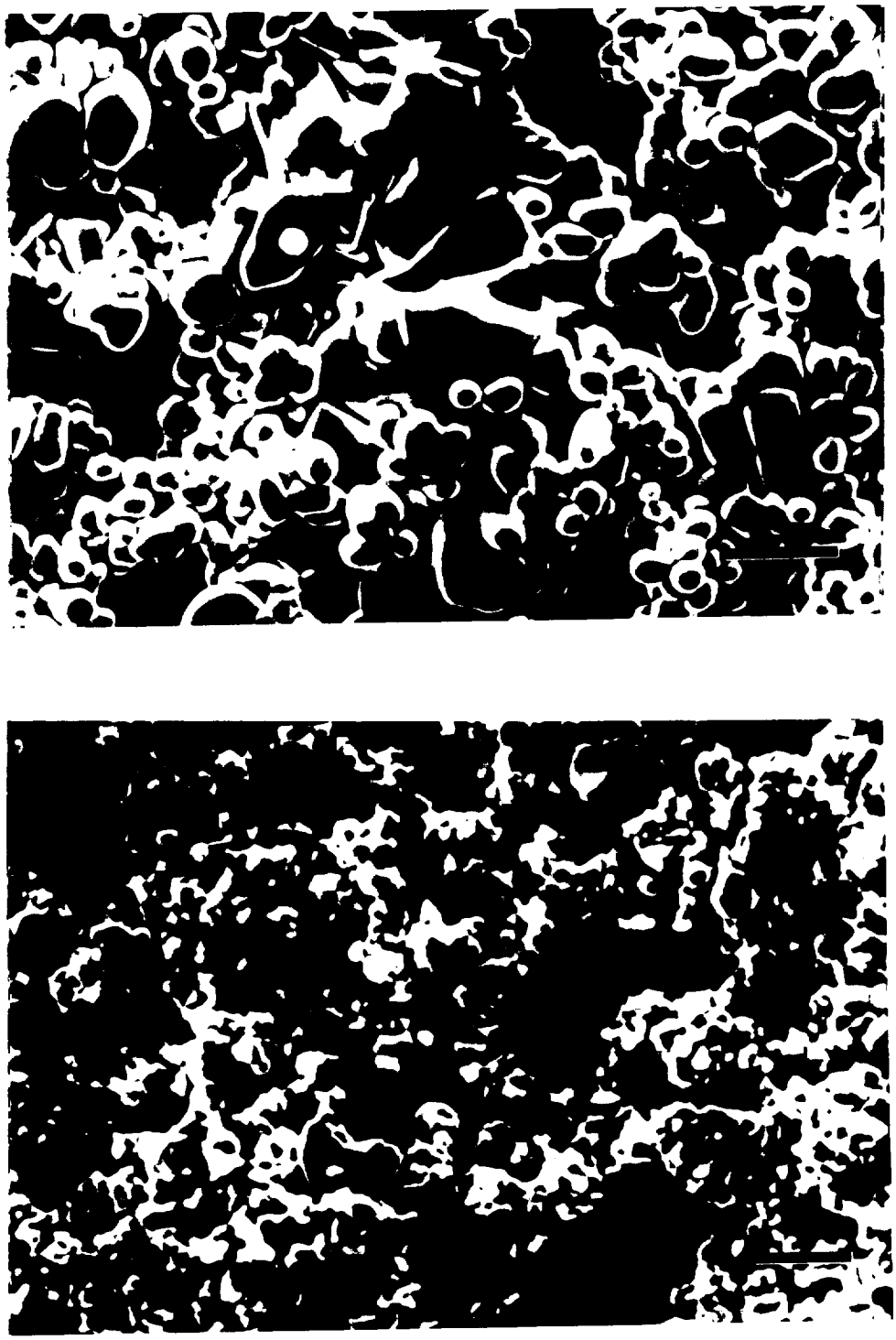

Figure 4: Microstructures of Y_2BaCuO_5/Al_2O_3 substrate(top) and $YBa_2Cu_3O_{7-x}$ thick film with 30% Ag_2O on Y_2BaCuO_5/Al_2O_3 substrate. Bars equal to 10 μm.

Figure 5: Formation of Y_2BaCuO_5 green phase on the $YBa_2Cu_3O_{7-x}$ thick film printed on the $211/Al_2O_3$ substrate, the film was fired at 940°C for 60 minutes. Bar equals to 10 μm.

Films fired on the SNT/Al_2O_3 substrates had better adhesion than those fired on 211/Al_2O_3 substrates. Smaller additions of Ag_2O were necessary for films fired on SNT/Al_2O_3 substrates because of improved film adhesion to the substrates. The T_c and J_c values of the $YBa_2Cu_3O_{7-x}$ films on SNT/Al_2O_3 substrates are listed in Table 1. These films had T_c values between 80 and 82.6 K at 1 mA measuring current. The highest J_c of the films on the SNT/Al_2O_3 substrates was 1.8 A/cm^2, which was fired at 950°C for 20 minutes.

The SNT/Al_2O_3 substrate had higher density than the 211/Al_2O_3 substrate, as shown in Figure 6. Better adhesion of the $YBa_2Cu_3O_{7-x}$ films printed on SNT/Al_2O_3 substrates than those on 211/Al_2O_3 substrates was believed to be due to the decrease porosity of the substrates. The films printed on the SNT/Al_2O_3 substrates also had larger grain size and better interconnectivity between $YBa_2Cu_3O_{7-x}$ particles than those of the films on 211/Al_2O_3 substrates. Improving the interconnectivity of the $YBa_2Cu_3O_{7-x}$ particles of the thick films on SNT/Al_2O_3 substrates enhanced the films' superconducting properties, as listed in Table 1.

II.3.1.2 $YBa_2Cu_3O_{7-x}$ thick films printed on YSZ substrates.

YSZ substrates provided the best adhesion to the $YBa_2Cu_3O_{7-x}$ thick films among the three kinds of the substrates used in this project. Table 2 lists the T_c and J_c values of $YBa_2Cu_3O_{7-x}$ thick films printed on YSZ substrates. Ten or twenty weight percent of Ag_2O was added to the films. The films with 10 wt% Ag_2O had T_c values between 81.2 and 86.1 K and J_c values between 2.6 and 15.2 A/cm^2. The T_c values of the films prepared at the same conditions varied with the film thickness. Since a constant current was applied during measuring, a thicker sample had lower current density than that of a thinner sample. Higher T_c values were obtained from the thicker samples which were subjected to lower current density[19]. Samples had higher J_c values when their film thicknesses were in the range between 18 and 30 μm. The superconducting properties, T_c and J_c, of the samples were enhanced by increasing the silver content. When 20 wt% of Ag_2O was added to the $YBa_2Cu_3O_{7-x}$ thick film, the T_c value of the film was 84.4 K or higher. A J_c value of 50.4 A/cm^2 was obtained from a 20 wt% Ag_2O

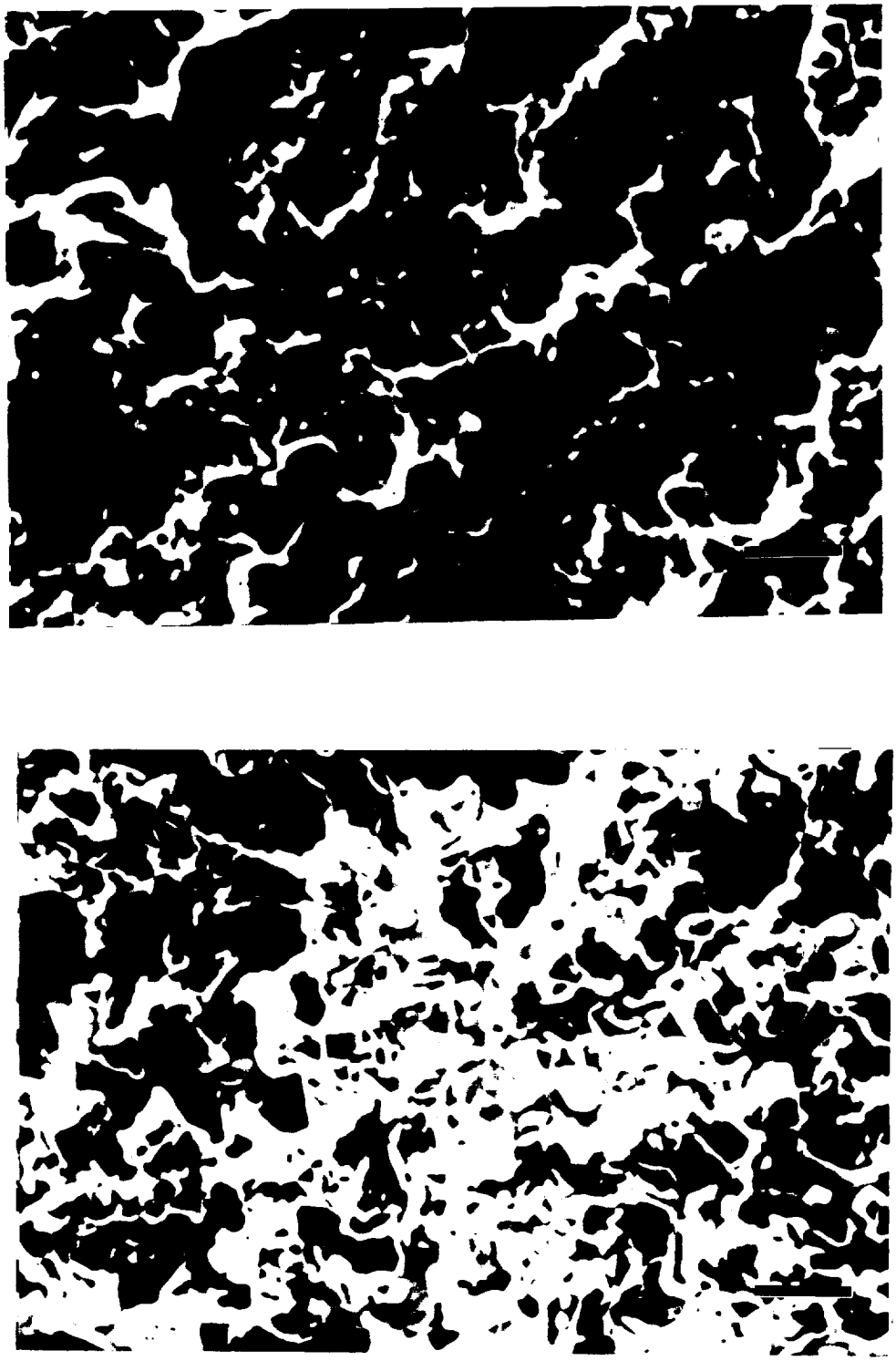

Figure 6: Microstructure of SNT/Al_2O_3 substructure (top) and $YBa_2Cu_3O_{7-x}$ superconductor thick film with 20wt% Ag_2O on SNT/Al_2O_3 substrate (bottom). Bars equal to 10μm.

sample fired at 990°C for 10 minutes. Among the films printed on 211/Al_2O_3, SNT/Al_2O_3, and YSZ substrates, the films printed on the YSZ substrates had the highest density and the best particles interconnectivity, as shown in Figure 7. They also had the best superconducting properties among those samples. The $YBa_2Cu_3O_{7-x}$ thick films with 10% Ag_2O had more crack than the films with 20% Ag_2O, as shown in Figure 7 and Appendix III. Trans-grain cracks were found on the $YBa_2Cu_3O_{7-x}$ thick films with 10% Ag_2O. This was due to the thermal expansion mismatching between the films and the substrates. The thermal expansion coefficient of the YSZ substrate used in this project was 8 x 10^{-6} K^{-1}, as shown in Appendix IV. However, the $YBa_2Cu_3O_{7-x}$ superconductor had thermal expansion coefficient from 12 to 14 x 10^{-6} K^{-1}[25]. Thus, the $YBa_2Cu_3O_{7-x}$ thick film printed on YSZ substrate was in a tension condition and was being subjected to that force during cooling. Little or no cracking was observed on the films with 20% Ag_2O, which had larger grain sizes than that of the films with 10% Ag_2O. The large grains of the films with 20% Ag_2O was instrumental in to avoiding cracks during cooling.

The x-ray diffraction pattern of the film with 10% Ag_2O and fired at 980°C form 10 minuted, which had granular microstructure, presented random crystal orientation, as shown in Figure 8. When the films with 20% Ag_2O were fired at 990°C for more than 5 minutes or at 980°C for 40 minutes, melted microstructures were observed from those samples, as shown in Figure 9 and Appendix V. Partial preferred orientation of the crystals in the (001) direction of $YBa_2Cu_3O_{7-x}$ were obtained from the films with melted microstructures, as shown in Figure 10. The films with preferred orientation had relatively higher J_c values than that of the films with random orientation. However, cracks were found on the films with melted microstructures. The cracks on the samples with melted microstructures caused the J_c of the samples to decrease. In order to eliminate the cracks on the films, higher thermal expansion substrates must be used. Currently, a MSZ (Magnesium Stabilized Zirconia),which has higher thermal expansion coefficient than the YSZ substrate, as shown in Appendix VI, is being used in this project.

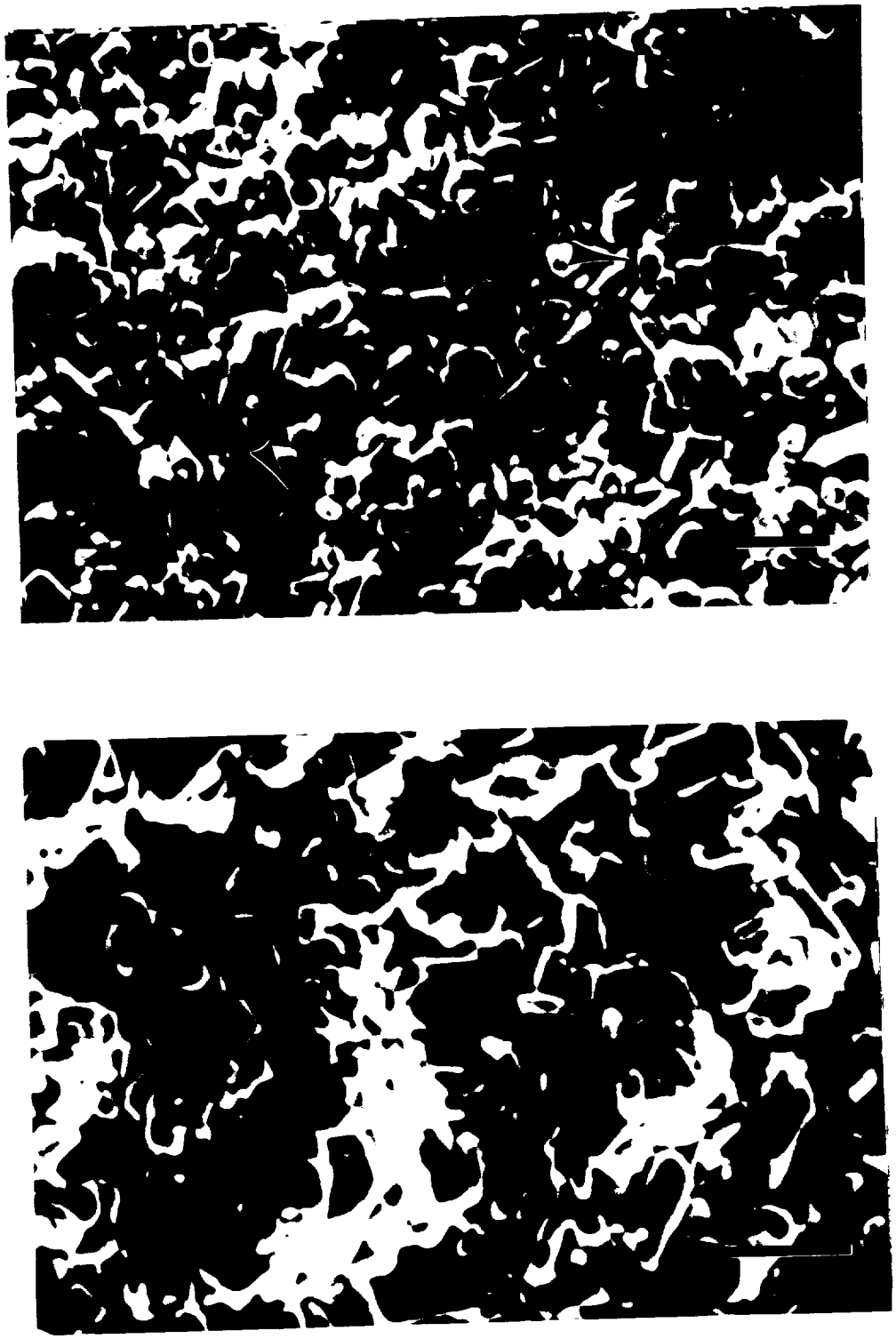

Figure 7: Microstructure of $YBa_2Cu_3O_{7-x}$ superconductor thick films with 10 (top) and 20wt% (bottom) Ag_2O on YSZ substrates. The films were fired at 980°C for 10 minutes. Bars equal to 10 μm.

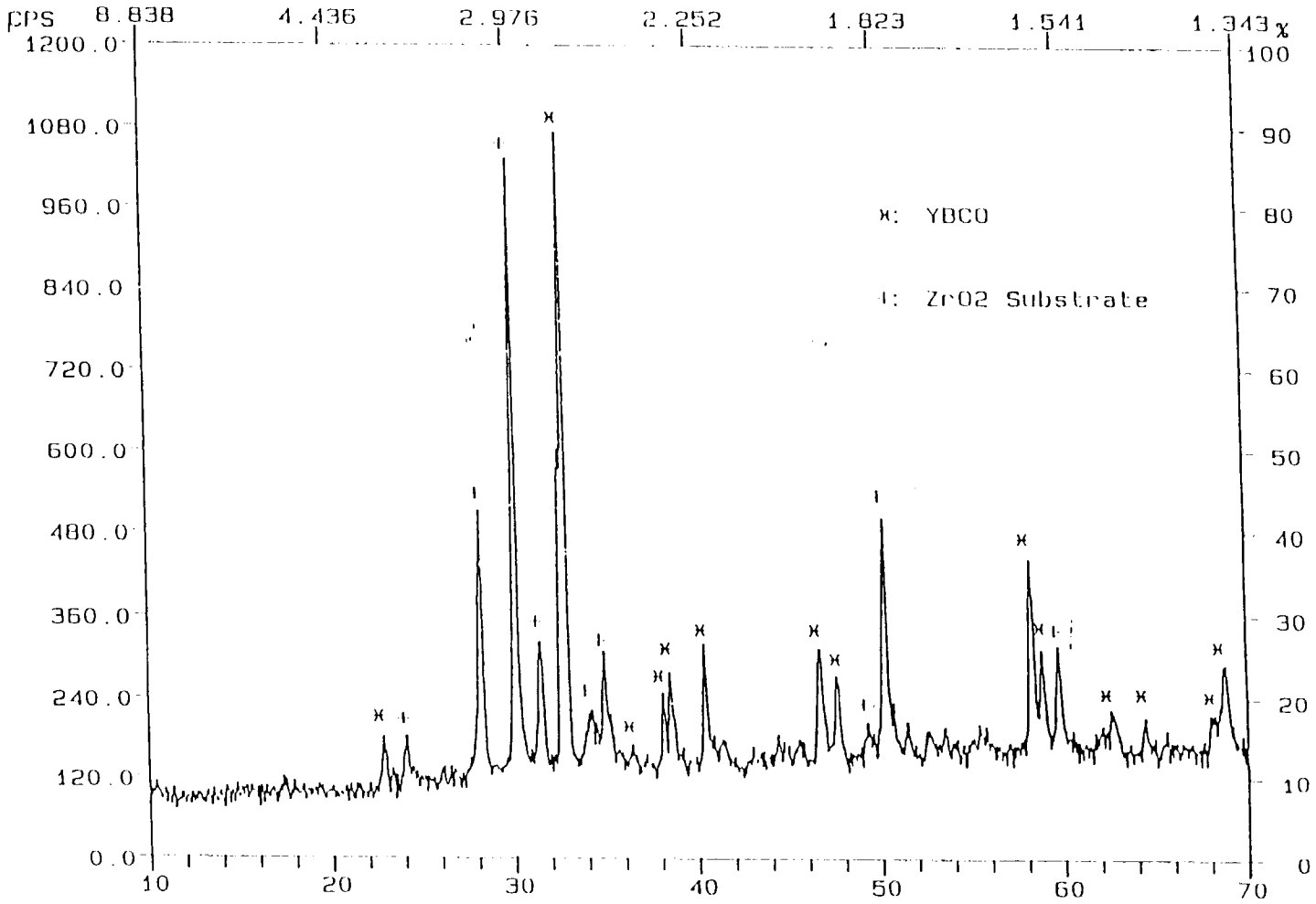

Figure 8: X-ray diffraction pattern of a $YBa_2Cu_3O_{7-x}$ superconductor thick film with 20wt% Ag_2O. The film was deposited on a YSZ substrate and fired at 980°C for 10 minutes.

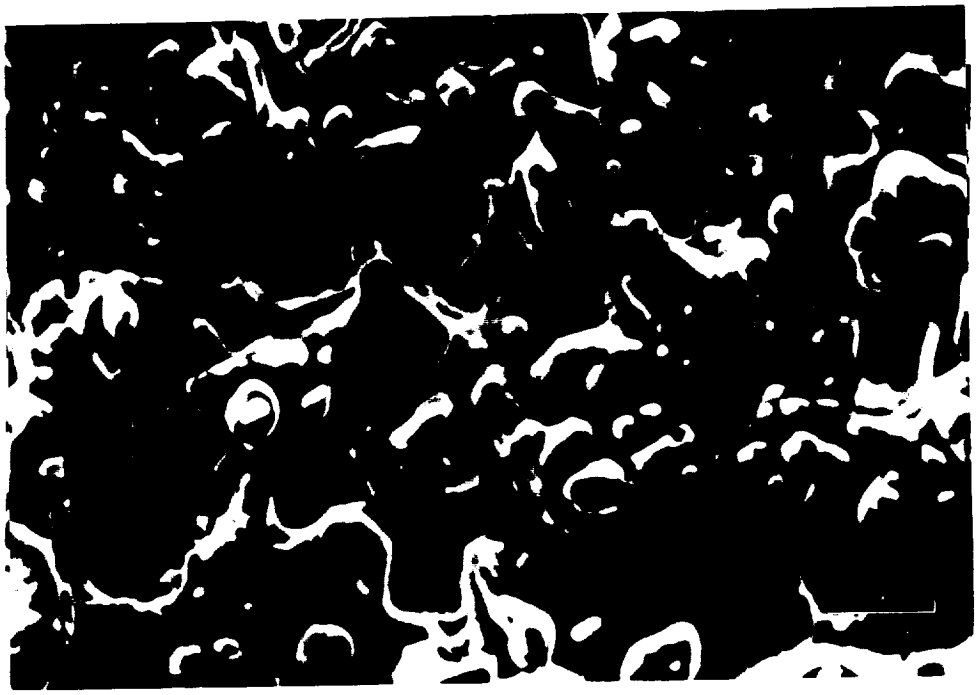

Figure 9: Microstructure of a $YBa_2Cu_3O_{7-x}$ superconductor thick film with 20wt% Ag_2O on YSZ substrate. The film was fired at 990°C for 5 minutes. Bar equals to 10 μm.

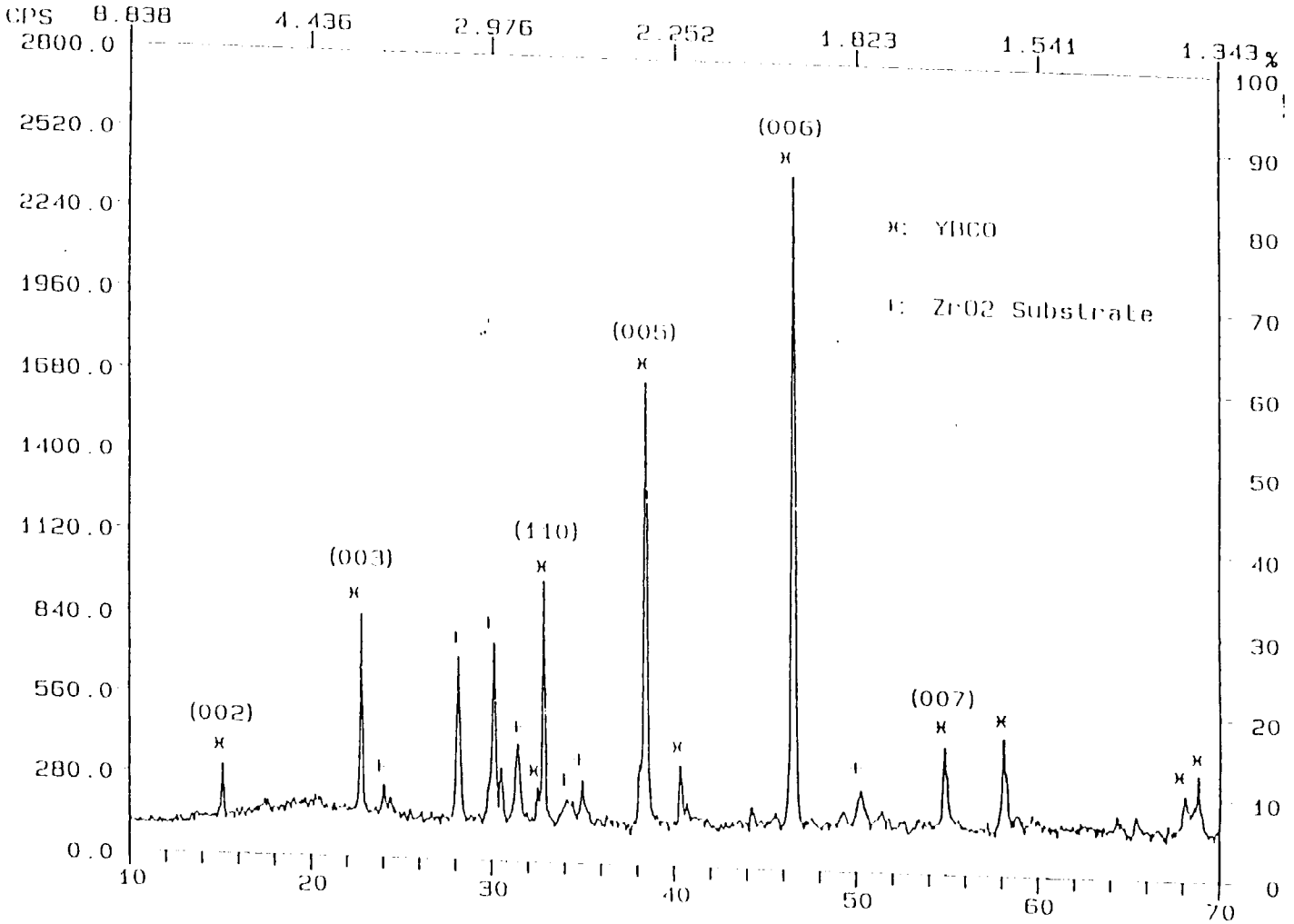

Figure 10: X-ray diffraction pattern of a $YBa_2Cu_3O_{7-x}$ superconductor thick film with 20wt% Ag_2O. The film was deposited on a YSZ substrate and fired at 990^{0}C for 5 minutes.

Table 2: The preparation conditions and properties of $YBa_2Cu_3O_{7-x}$ screen printed thick films on YSZ substrates.

Sintering Temp.	Sintering Time	T_c(K)	J_c(A/cm^2)	Thickness	Ag(%)
950°C	60 min.	82.4	2.6	24 μm	10
970°C	10 min.	83.7	3.3	30 μm	10
970°C	60 min.	84.0	15.2	18 μm	10
970°C	60 min.	84.9	6.1	29 μm	10
980°C	10 min.	82.4	4.6	14 μm	10
980°C	10 min.	84.4	1.8	54 μm	10
980°C	30 min.	84.9	11.9	18 μm	10
980°C	30 min.	81.2	2.7	13 μm	10
990°C	5 min.	86.1	8.4	23 μm	10
990°C	10 min.	85.0	7.72	21 μm	10
970°C	60 min.	86.3	7.7	20 μm	20
980°C	10 min.	84.4	8.0	17 μm	20
980°C	30 min.	84.4	16	13 μm	20
980°C	40 min.	86.5	49.8	08 μm	20
990°C	10 min.	86.4	50.4	12 μm	20
960°C	10 min.	85.8	-	-	20

II.3.2 $YBa_2Cu_3O_{7-x}$ multiple-lead films.

Multiple-lead thick films with 10 wt% Ag_2O were fabricated on YSZ substrates. The films fired at 980°C for 10 minutes had a T_c value of 82 K at 100 μA measuring current as shown in Figure 11. The J_c of each line at 77 K was 0.9 A/cm^2. The T_c of this sample was in the same range as the single samples fired at the same conditions. The J_c of the film, however, was about five times lower than the single sample. The multiple-lead film fired at 970°C for 60 minutes was

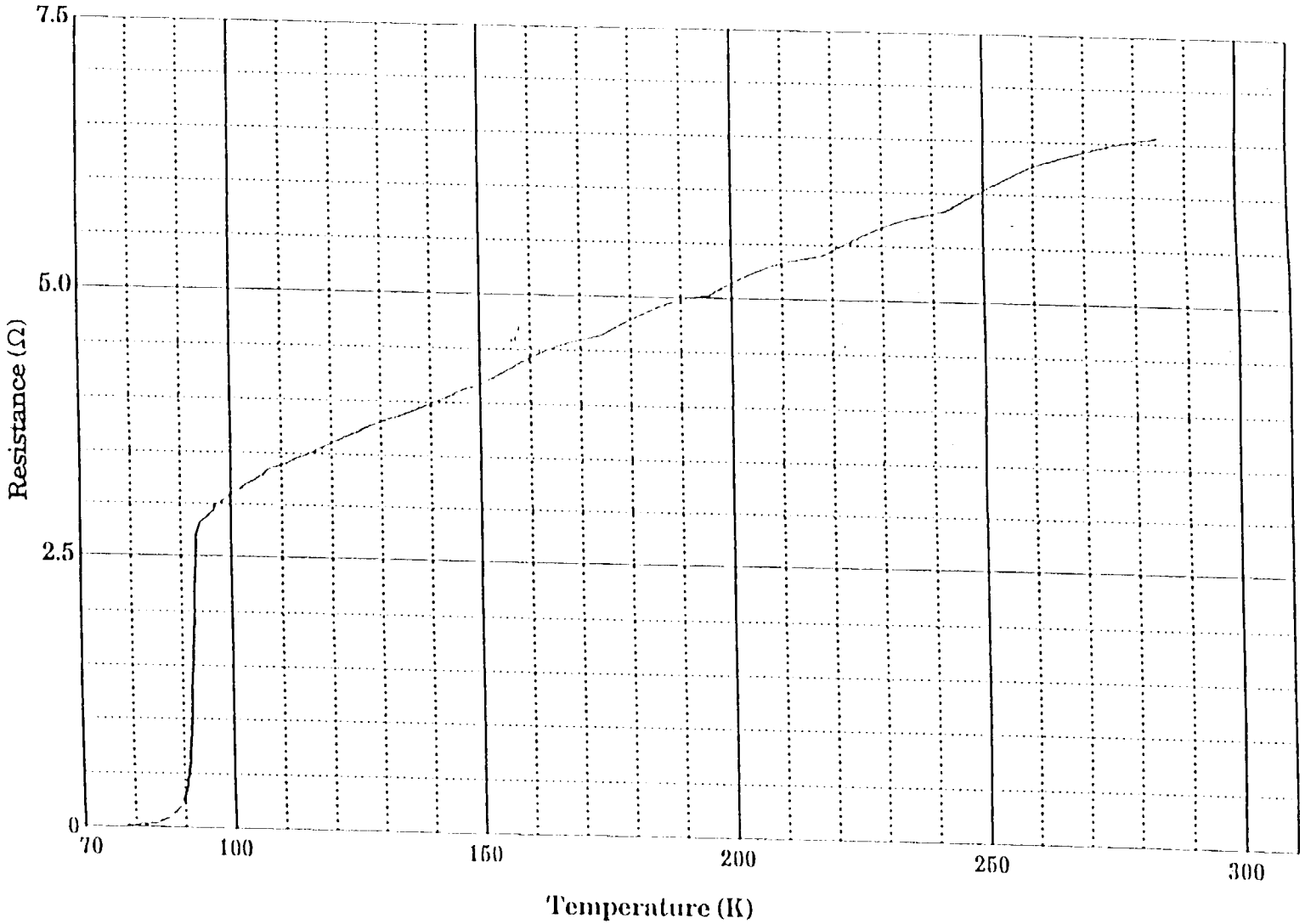

Figure 11: T_c curve of a $YBa_2Cu_3O_{7-x}$ multiple-lead sample. The resistance was measured at a 100 μA constant current.

not in a superconducting state at 77 K with a 100μA measuring current. When the measuring current decreased to 10 μA, the sample showed zero resistance at 80.2 K. This was because of the relatively low J_c values of the sample. The sample fired at 970°C for 1 hour had serious cracking, as shown in Figure 7. The cracking yielded lower T_c and J_c values than those of the former sample, although it had a more dense film than the former. Since increasing the silver addition in the $YBa_2Cu_3O_{7-x}$ thick film was found to enhance the superconducting properties of the films, $YBa_2Cu_3O_{7-x}$ multiple-lead samples with 20 wt% Ag_2O is presently being printed on the YSZ substrate.

III. BSCCO Thick Films.

III.1 Introduction.

Phase transformation of BSCCO superconductor from high-T_c phase (2223) to low-T_c phase (2212) makes fabrication of BSCCO thick films more complex than that of Y-based thick film. Different compositions of lead doped BSCCO powders have been used in thick film processes, as listed in Appendix VII. Because long heat treatment time is necessary to obtain pure 2223 phase thick films and interactions occur between the BSCCO material and the substrate, a pure 2223 phase BSCCO powder is preferred to be used as a raw material to make a paste in the screen printing process. An undesirable insulating material (yellow-green in color) was found in the films fired on sapphire and YSZ substrate[17]. So far, the highest T_c value of the BSCCO thick films on YSZ substrates published was 72K[17]. Both single crystal and polycrystalline MgO substrates were noted to be the best substrate materials for BSCCO thick films[17,20,21,23].

However, the MgO substrate has much higher thermal conductivity than the stabilized ZrO_2 substrate[26]. Since the high thermal conductivity of the substrate will increase the evaporation rate of the liquid helium in the SAFIRE program, the ZrO_2 based material is considered to be the best substrate material for the program.

In this research, the MgO and the ZrO_2 based substrates were used.

The MgO substrate was used to investigate the best heat treatment conditions of the BSCCO thick films. In order to avoid the interaction between the BSCCO thick film and the ZrO_2-based substrate, various buffer layer materials were applied to the stabilized ZrO_2 substrate.

III.2 Experimental Procedure.

Two kinds of BSCCO powders of 2223 composition were prepared; i.e., (1) solid state reaction and (2) oxalate co-precipitation. In the solid state reaction method, Bi_2O_3, $SrCO_3$, $CaCO_3$, CuO, and PbO were mixed in distilled water and then dried at 110°C for 12 hours. The dry powder was calcined at 850°C for 30 hours, cooled to room temperature and crushed in a mortar and pestle. The powder was calcined with these conditions for four times before it was made into a paste. In the oxalate co-precipitation process, a clear precursor solution was prepared by mixing bismuth acetate, calcium acetate, strontium acetate, copper acetate, and lead subacetate in a methanol solution. Acetic acid and ammonium hydroxide were used to adjust the pH value of the solution. The precursor solution was slowly poured into a stirring oxalic acid / methanol solution, which produced a BSCCO oxalate co-precipitant. The co-precipitant was dried in a vacuum dryer for 8 hours. Dried BSCCO oxalate was calcined at 600°C for 6 hours to burn off the oxalate hydrocarbons. After the oxalate burned off, the BSCCO powder was further calcined at 830°C for 24 hour for 2 times.

A BSCCO paste was prepared by mixing BSCCO calcined powder with terpineol, ethanol, and toluene in 30:7:1:1 ratios. BSCCO thick films were printed on the MgO polycrystalline substrate by the same procedure used in the $YBa_2Cu_3O_{7-x}$ thick film process. Screen printed BSCCO thick films were fired at temperatures between 830 to 855°C for different times.

III.3 Results and Discussion.

III.3.1 Powder Characterization.

BSCCO powders prepared by the solid state reaction and co-precipitation methods were characterized by measuring the T_c curve of a sintered pellet and the X-ray diffraction patterns of powders. Figure 12 shows the T_c curve of a

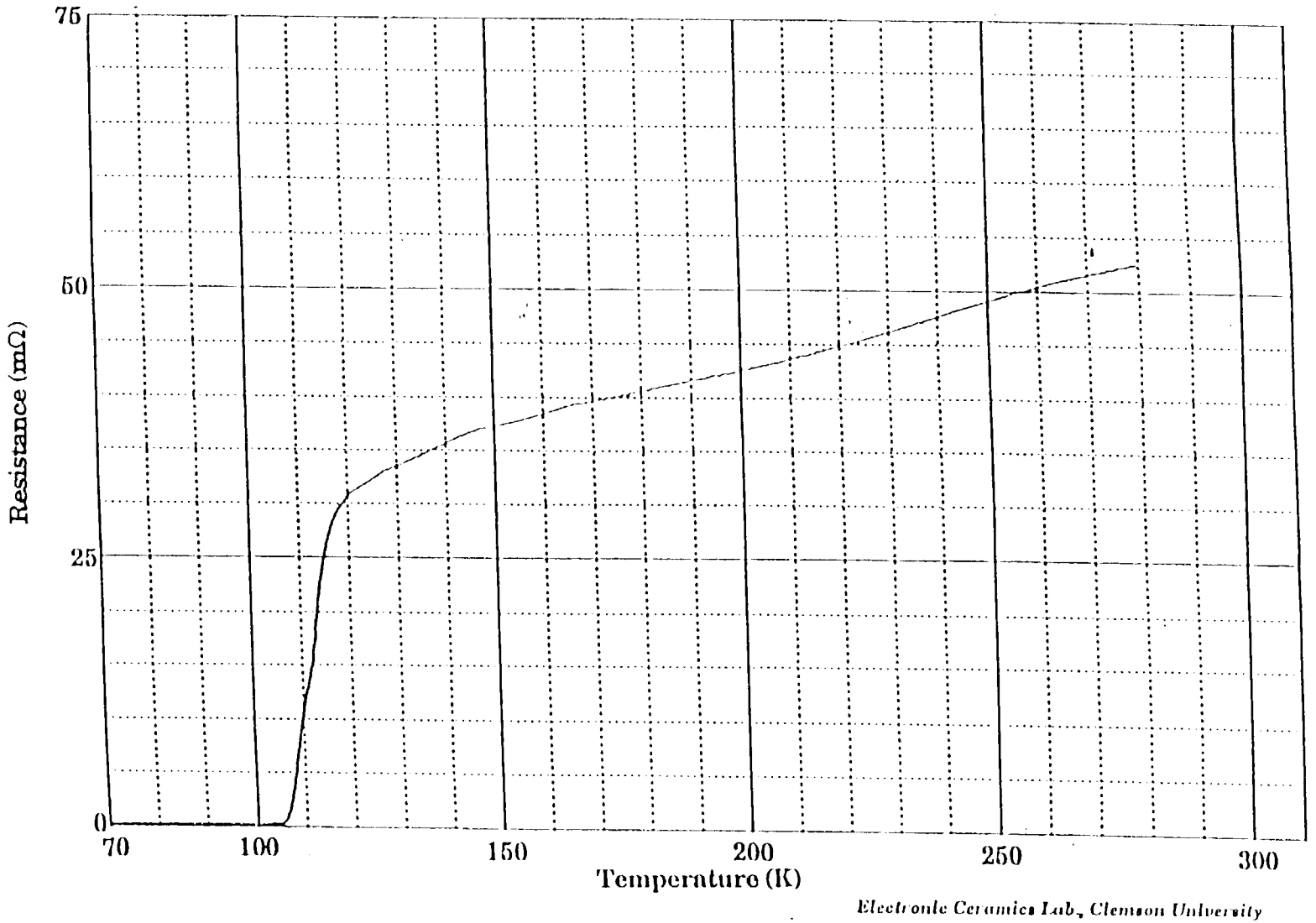

Figure 12: T_c curve of a BSCCO superconductor sintered pellet. The pellet was prepared by solid state reaction powder.

sintered pellet prepared from the solid state reaction powder. The pellet had a T_c of 103 K. Two steps were found in the T_c curve between the onset and offset temperatures. Both low and high-T_c phases were found in the four times calcined oxide powder, as shown in Figure 13. Only one step was found in the T_c curve of the oxalate prepared pellet, as shown in Figure 14, indicating a homogeneous, single phase 2223 material. This sample had a T_c=105.7 K and J_c= 141 A/cm^2. Presently, different calcination conditions for the oxalate co-precipitated powder are under investigation in order to achieve the best calcination conditions for this powder.

III.3.2 BSCCO Thick Film.

Figure 15 shows the T_c curve of a BSCCO screen printed thick film prepared by four times calcined powder. The film was fired at 845^{o}C for 1 hour. Two steps, as found in the T_c curve of the four times calcined pellet, were observed from this curve. The film was not in the superconducting state at 77 K with 1 mA measuring current. When the measuring current was decreased to 0.62 mA, the film show zero resistance at 77 K. Therefore, this film had a relatively low critical current density (J_c) . The films prepared by co-precipitated powder were printed on MgO substrates and fired at 840^o and 845^{o}C for different times. The film fired at 845^{o}C for 30 minutes had a T_c at 86.5K at 20μA measuring current, as shown in Figure 16. When the heat treatment time was increased to 60 minutes, the T_c of the film increased to 89.0K, as shown in Figure 17. Figure 18 presents the T_c curve of the film heat treated at 845^{o}C for 120 minutes, the T_c of the film decreased to 85.4K. When the BSCCO thick film was fired at 840^{o}C for 360 minutes, the film had T_c at 88.0K, as given in Figure 19. The heat treatment temperature at 840^{o}C, thus, was considered to be a critical heat treatment temperature of the BSCCO thick film. At or lower than that temperature, the BSCCO thick films had a slow reaction rate with substrate materials. This heat treatment critical temperature was also observed in the films printed on YSZ substrates. The film printed on YSZ substrate became a semiconducting layer when it was fired at 850^{o}C for 5

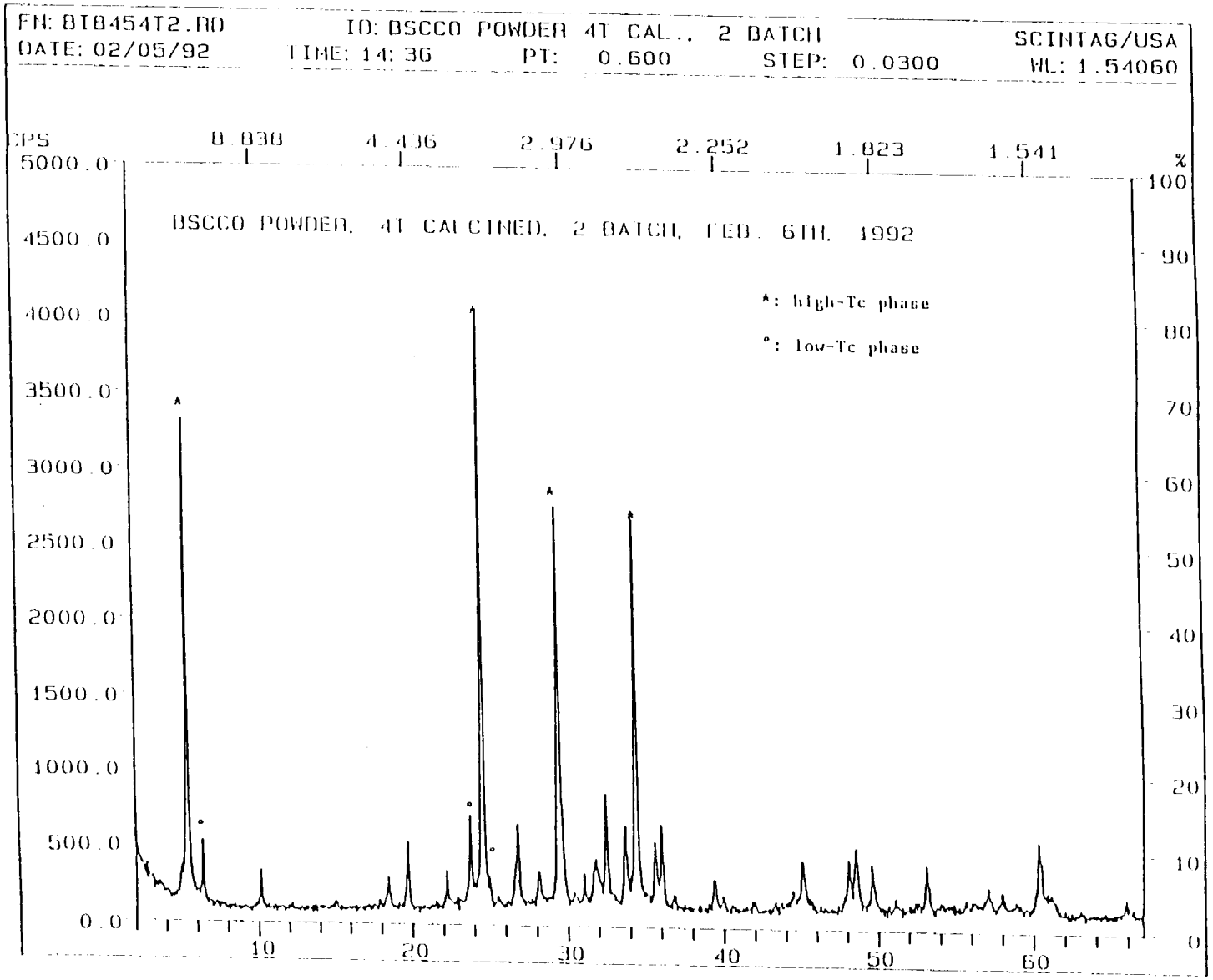

Figure 13: X-ray diffraction pattern of a solid state reaction powder after four times calcined at 845^{o}C for 30 hours.

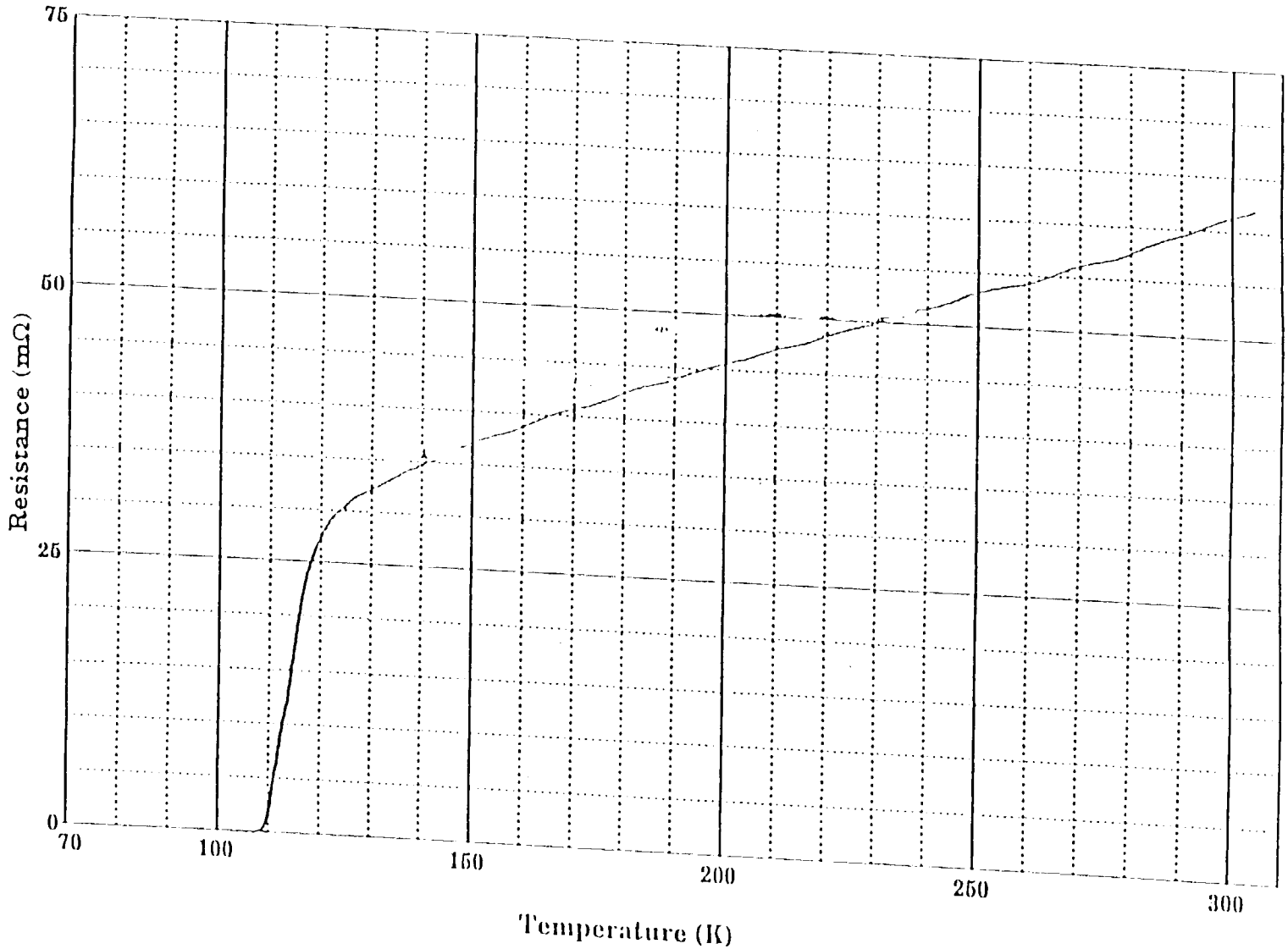

Figure 14: T_c curve of a BSCCO superconductor sintered pellet. The pellet was prepared by oxalate co-precipitated powder and sintered at 850^{0}C for 30 hours.

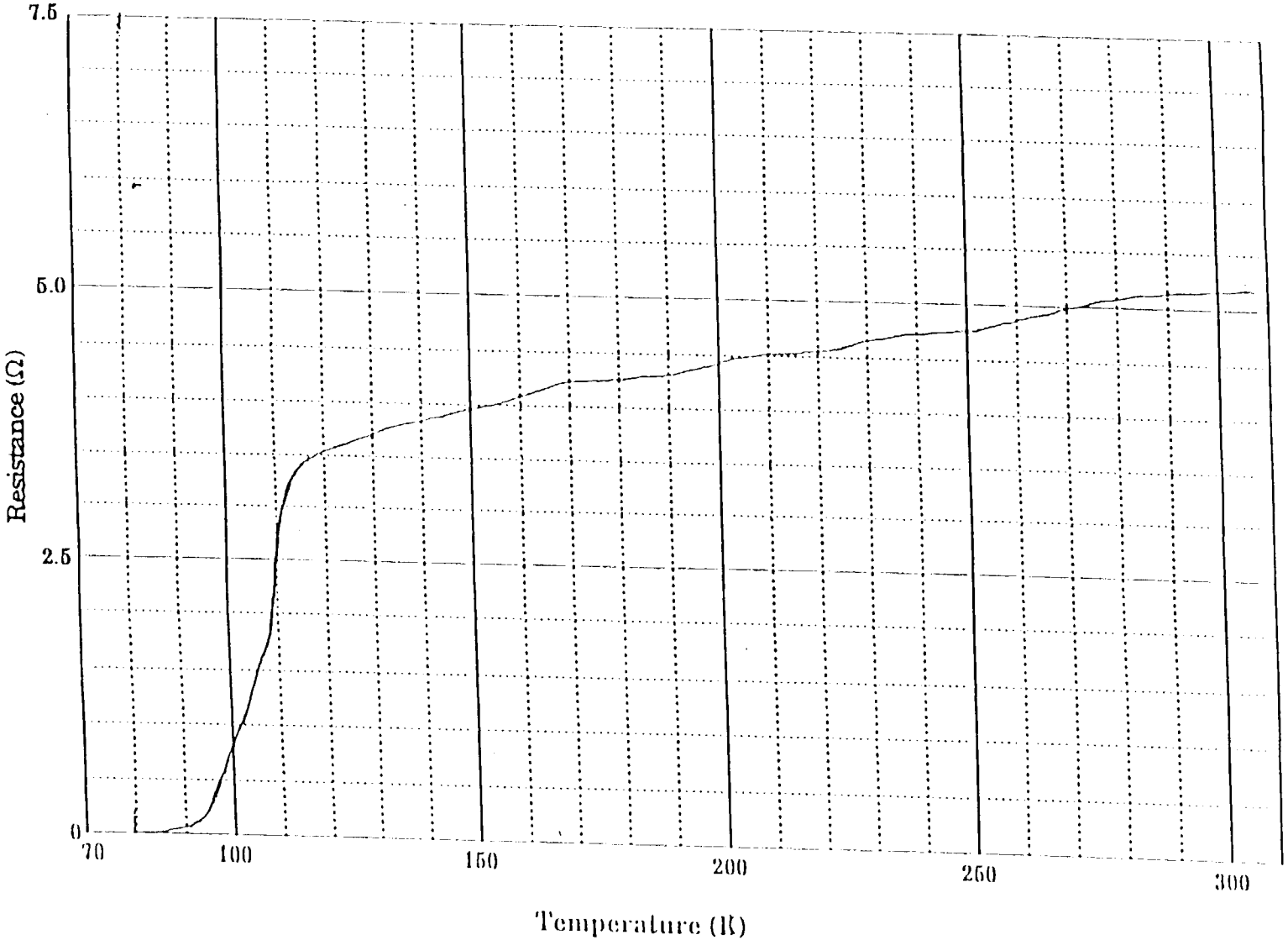

Figure 15: T_c curve of a BSCCO thick film printed on a MgO substrate. The film was annealed at 845^{0}C for 1 hour.

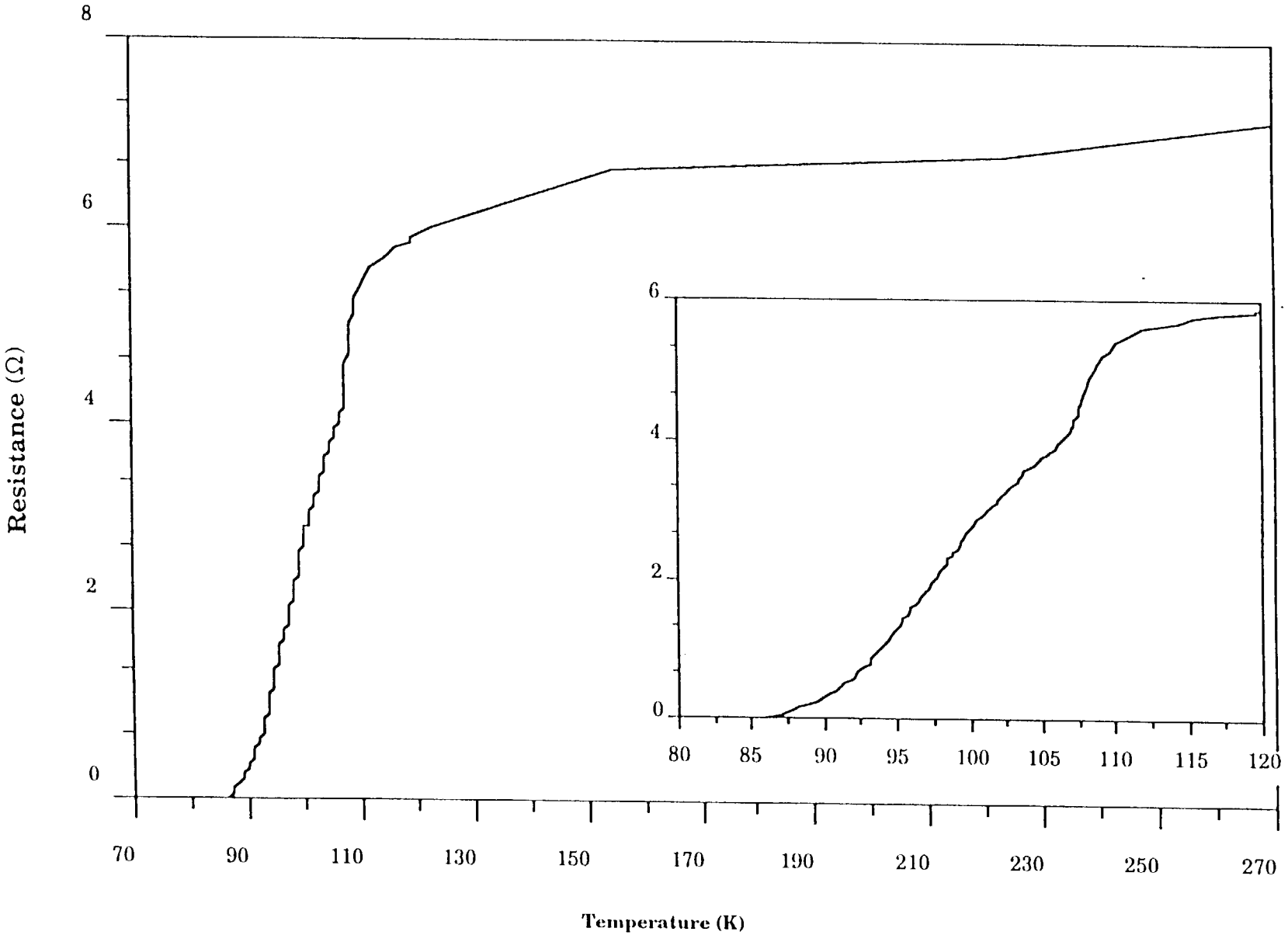

Figure 16: T_c curve of a BSCCO thick film printed on MgO substrate, T_c= 86.5K. The film was printed by co-precipitated powder and fired at 845°C for 30 minutes.

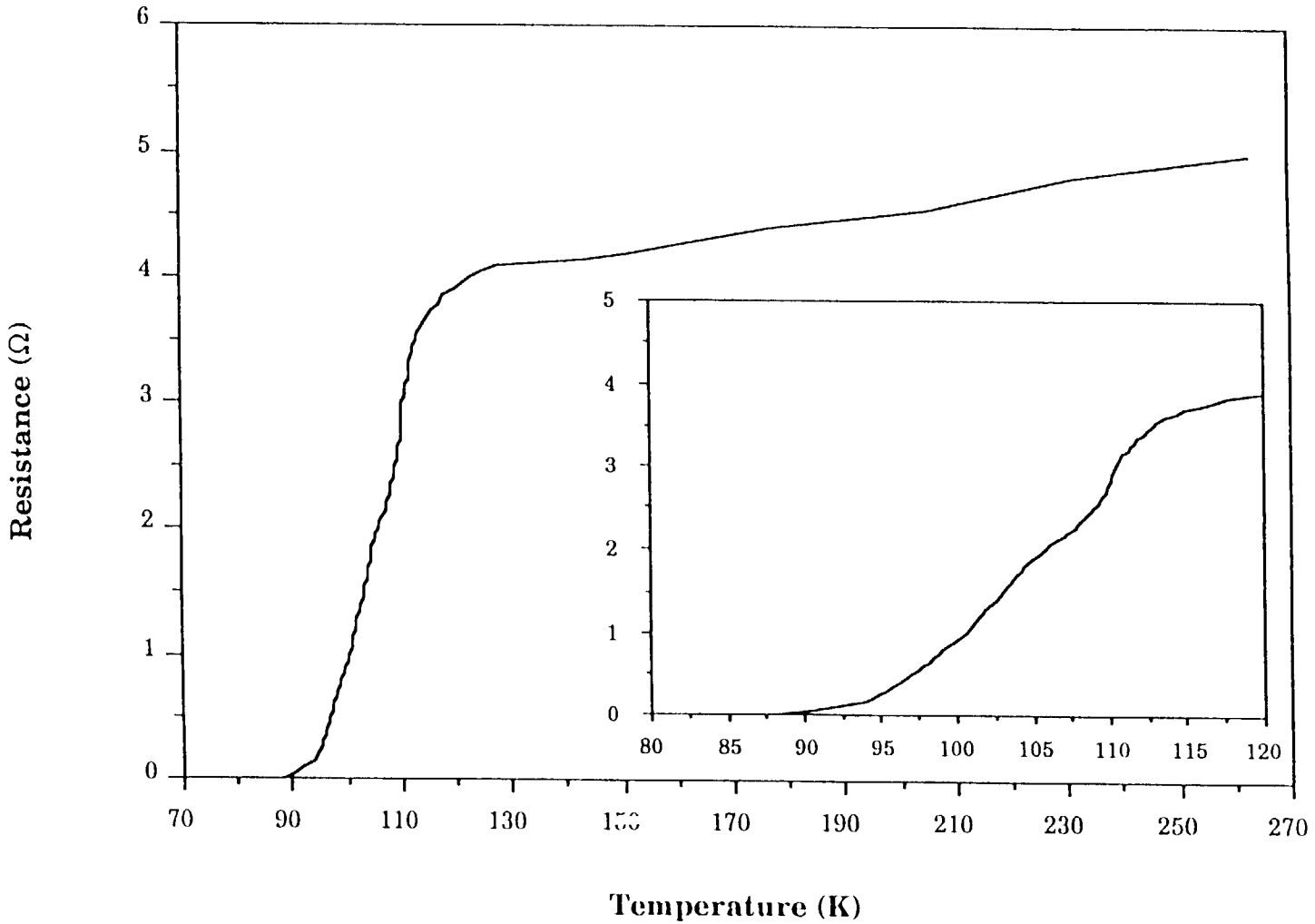

Figure 17: T_c curve of a BSCCO thick film printed on MgO substrate, T_c= 89.0K. The film was printed by co-precipitated powder and fired at 845^{0}C for 60 minutes.

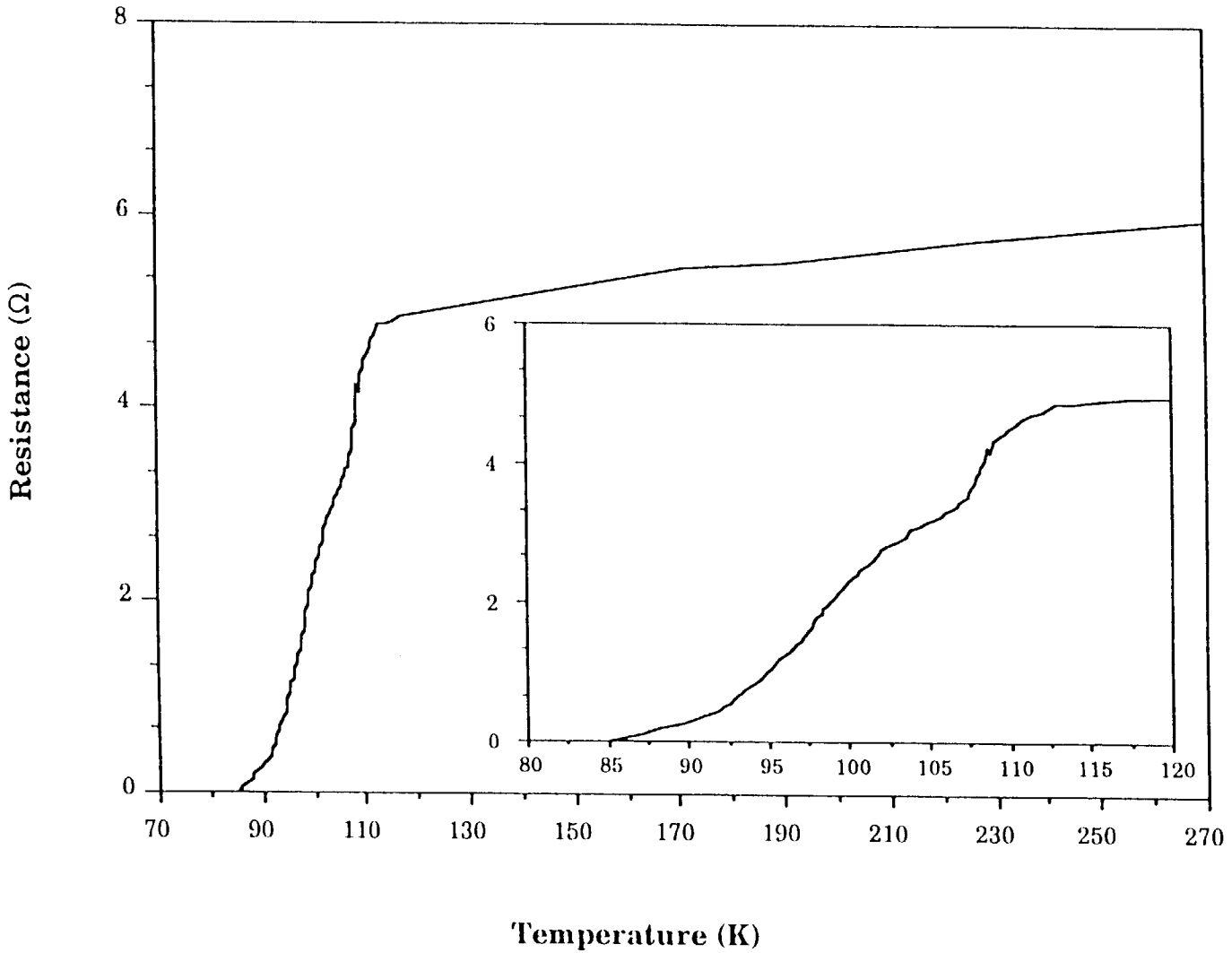

Figure 18: T_c curve of a BSCCO thick film printed on MgO substrate, T_c= 85.4K. The film was printed by co-precipitated powder and fired at 845^{0}C for 120 minutes.

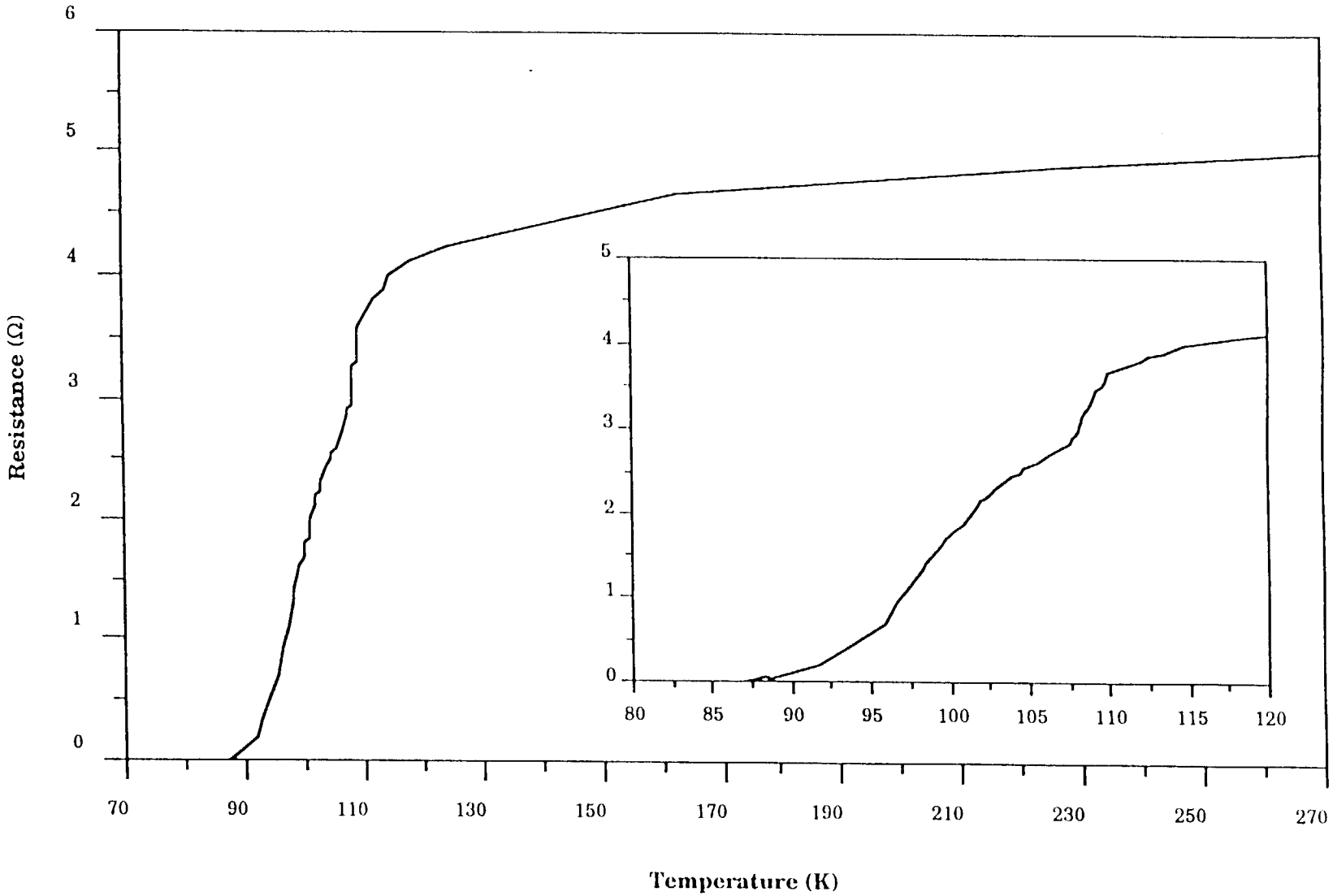

Figure 19: T_c curve of a BSCCO thick film printed on MgO substrate, T_c= 88.0K. The film was printed by co-precipitated powder and fired at 840^{0}C for 360 minutes.

minutes, as shown in Figure 20. When the film printed on YSZ substrate was fired at 840°C, it maintained metallic behavior before the onset temperature, as presented in Figure 21. So far, the BSCCO thick films printed on the YSZ substrates have not been found in the superconducting state at temperature higher than 77K.

The resistivity of the films printed on MgO substrate at room temperature were in the 10^{-2} Ω/cm range, which was in the same range as the bulk samples. The room temperature resistivity of the films printed on the YSZ substrate, however, were in the 10^{-1} range or higher. This increasing resistivity of the films at room temperature was caused by the reaction of the films and substrates. The more serious reaction the samples had, the higher room temperature resistivity it had. Therefore, a buffer layer on the YSZ substrate was necessary to obtain a superconducting thick film on it. A BSCCO buffer layer was melted on a YSZ substrate at 880°C for 10 minutes before the BSCCO thick film was printed on it. This sample presented the same room temperature resistivity range as the film printed on MgO substrate and had T_c at 88.4K, as given in Figure 22. Since the BSCCO buffer layer showed metallic behavior, it could not qualify as a buffer material for the SAFIRE project. MgO buffer layers coated on YSZ or MSZ substrates were applied by a dip coating process. Because the MgO layers had serious cracks, as shown in Figure 23 , interaction between the BSCCO thick film and the substrate was observed, as shown in Figure 24.

The T_c curves of the BSCCO thick films printed on MgO or BSCCO coated YSZ substrates showed two steps after the onset temperature. This was caused by the weak link between BSCCO particles in the films, as presented in Figure 25. In order to obtain a BSCCO thick film with higher T_c value, a dense and low interaction with substrate BSCCO thick film must be prepared. Presently, the best processing conditions of MgO buffer layer on YSZ or MSZ (Magnesium Stabilized Zirconia) substrates, which can prepare cracks free microstructure, are under investigation in order to achieve a solid MgO buffer film on the ZrO_2 substrate. The BSCCO thick films will be printed on the zirconia based substrate after the coating conditions are determined.

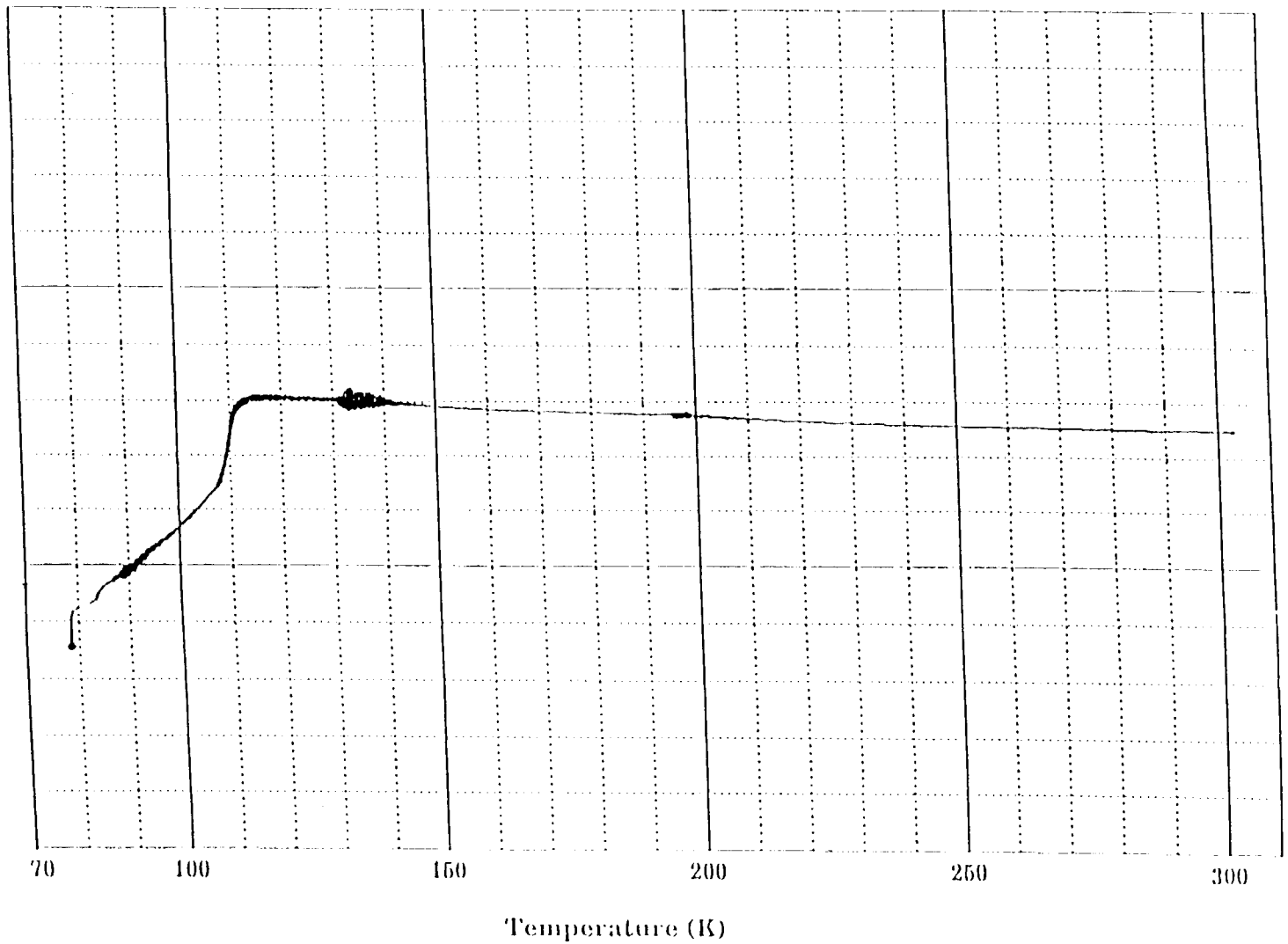

Figure 20: T_c curve of a BSCCO thick film printed on YSZ substrate. The film was printed by co-precipitated powder and fired at 850^{0}C for 5 minutes.

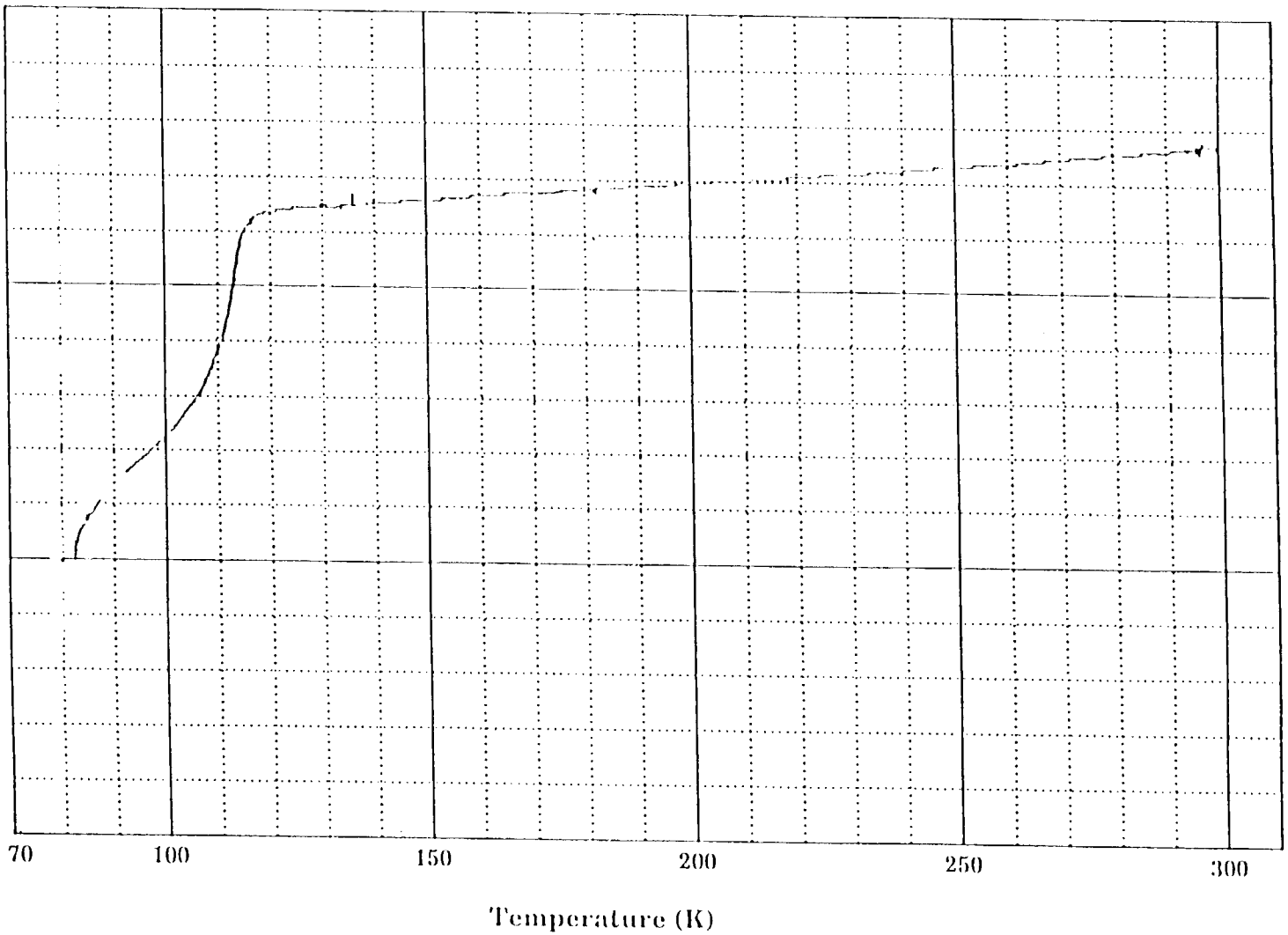

Figure 21: T_c curve of a BSCCO thick film printed on YSZ substrate. The film was printed by co-precipitated powder and fired at 840^{0}C for 240 minutes.

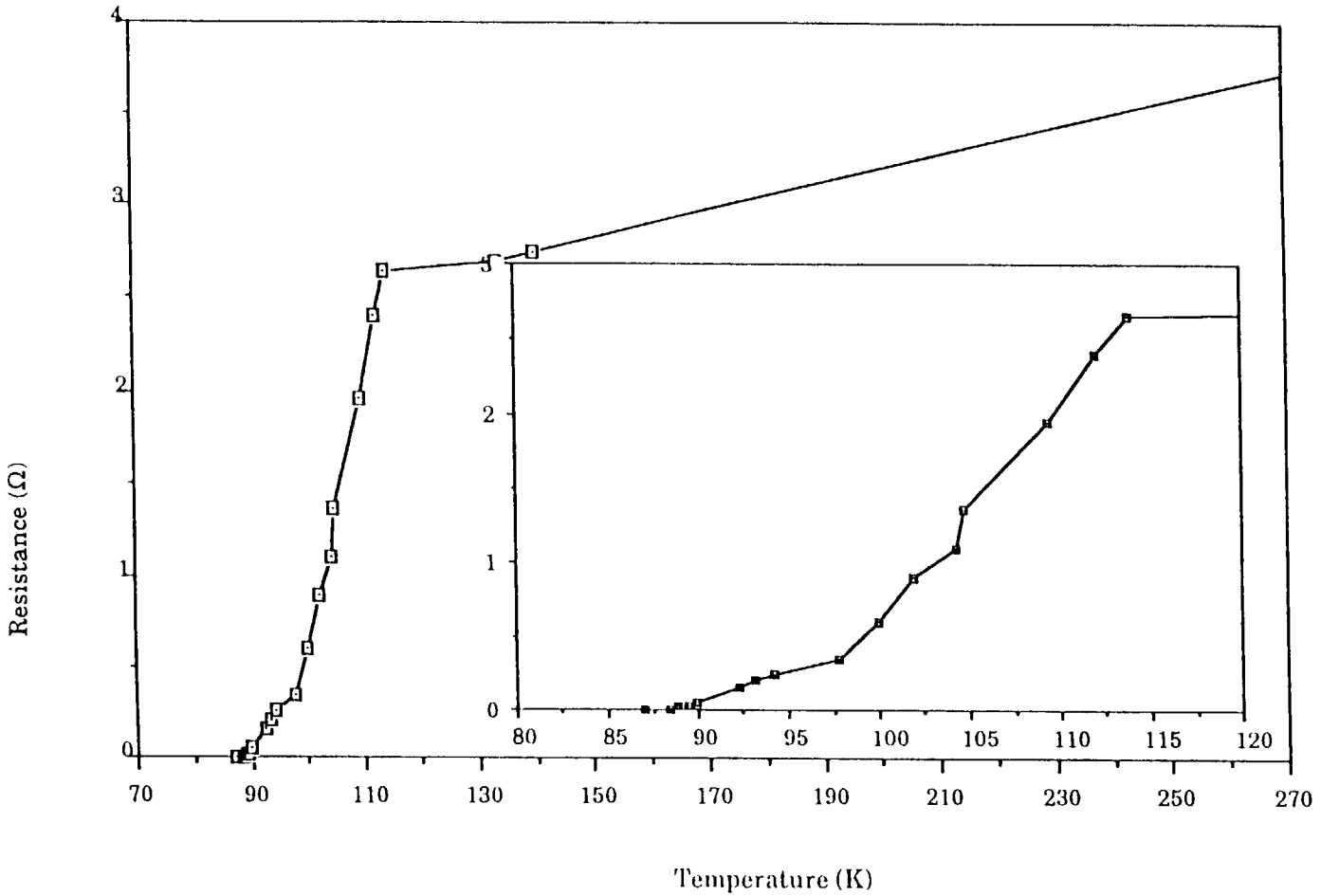

Figure 22: T_c curve of a BSCCO thick film printed on BSCCO/YSZ substrate. The film was printed by co-precipitated powder and fired at 845^{0}C for 60 minutes.

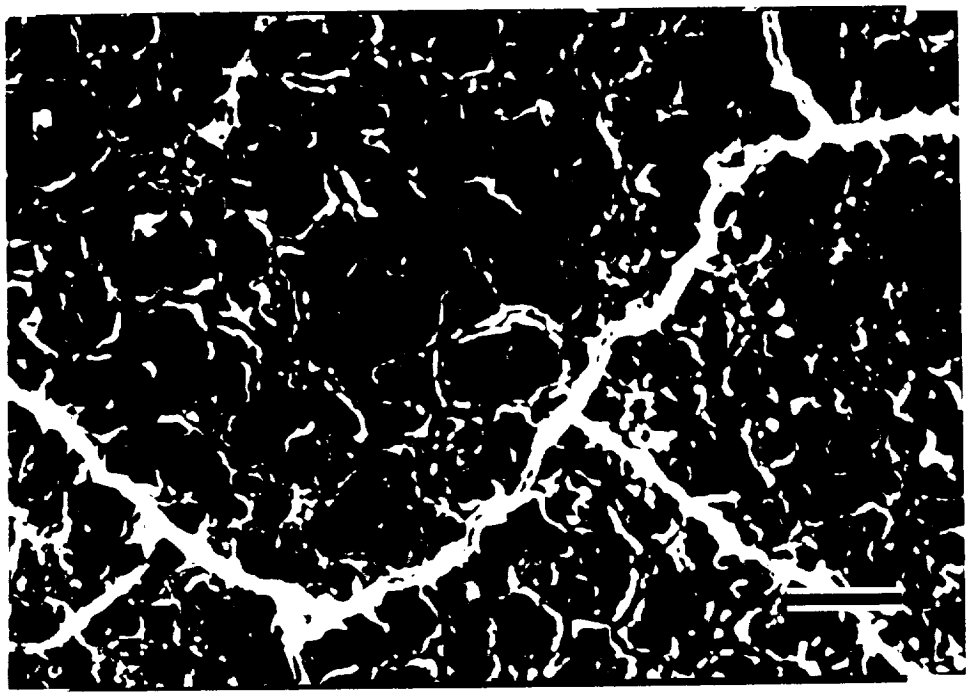

Figure 23: Microstructure of MgO buffer layer after 1500^{o}C annealing. Bar equals to 10 μm.

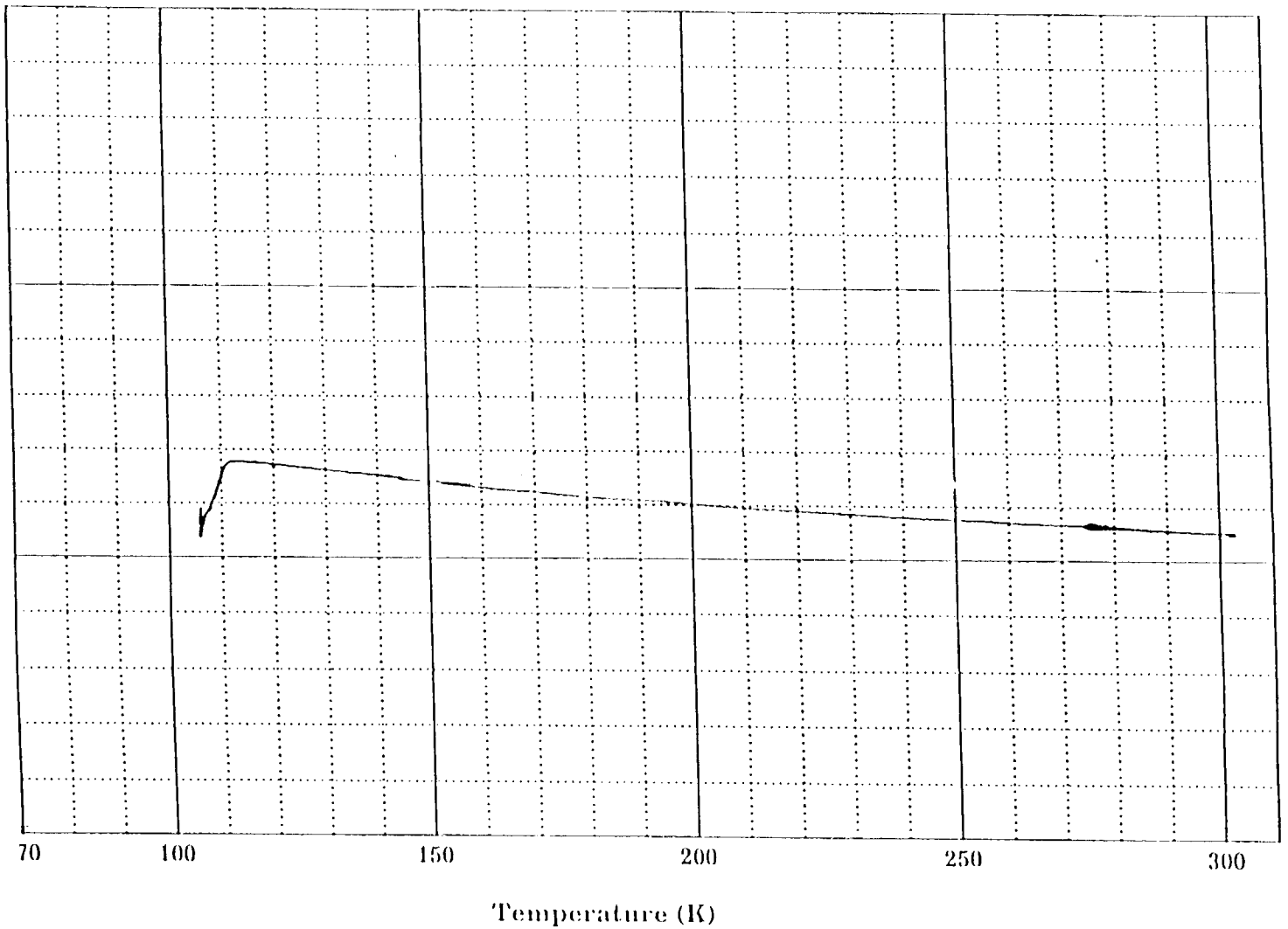

FIgure 24: T_c curve of BSCCO thick film on 10 layers MgO coated YSZ substrate. The film was printed by co-precipitated powder and fired at 850^0C for 60 min[illegible].

Figure25: Microstructure of BSCCO thick film on MgO substrate. The film was printed by co-precipitated powder and fired at 845°C for 120 minutes. Bar equals to 10 μm.

IV. Summary.

1. Critical temperatures (T_c) of $YBa_2Cu_3O_{7-x}$ superconductor thick films were influenced by the densification of the films.
2. Cracking of the $YBa_2Cu_3O_{7-x}$ superconductor thick films and adhesion of the films to the substrates were improved by adding Ag_2O into the film.
3. Higher Critical current density (J_c) $YBa_2Cu_3O_{7-x}$ superconductor thick films with preferred orientation in the (001) direction were obtained from the films with 20wt% Ag_2O deposited on the YSZ substrates and fired at 990°C for 5 to 10 minutes.
4. Mutiple-lead $YBa_2Cu_3O_{7-x}$ superconducting thick film with T_c= 82 K was deposited on YSZ substrate. The J_c of the sample, however, was relatively low in comparison to the plain samples.
5. A pure high-T_c BSCCO (2223) powder was obtained via an oxalate co-precipitation process.
6. A BSCCO thick film printed on a MgO substrate and fired at 845°C for 60 minutes had T_c value at 89.0K. Because of poor interconnection, the film had a relatively low J_c value.
7. A buffer layer was found to be necessary to deposit the BSCCO thick films onto YSZ substrates.

Acknowledgement

The authors would like to express their appreciation to Ms. Joan Hudson and Andy Nelson of the Electron Microscopy Laboratory at Clemson University for their assistance in SEM observation and Dr. Eric C. Skaar of the Ceramic Engineering Department for his valuable discussion.

References

1. P. Stastny, R. Kuzel, and V. Skacel, J. Less-Common Metals, 164-165, 464-469, 1990.
2. M. V. S. Lakshmi, K. Ramkumar, and M. Satyam, J. Mater. Sci., 26, 4092-4094, 1991.
3. R. C. Budhani, S. M. Tzeng, H. J. Doerr, and R. F. Bunshah, Appl. Phys. Lett., 51, 1277-1279, 1987.
4. N. L. Corah, Jr., R. L. Wahlers, S. J. Stein, I. Perez, J. Schwegler, G. H. Myer, and J. E. Crow, ISHM '89 Proceeding.
5. C. Wu, Y. Tzeng, R. P. Hunt, M. A. Belser, and T. A. Roppel, J. Electrochem. Soc., 136, 1570-1571, 1989.
6. M. Itoh and H. Ishigaki, Jpn. J. Appl. Phys., 27, L420-L422, 1988.
7. N. P. Bansal, R. N. Simons, and D. E. Farell, Appl. Phys. Lett., 53, 603-605, 1988.
8. M. Senda and O. Ishii, J. Appl. Phys., 69, 6586-6589, 1991.
9. J. Tabuchi and K. Utsumi, Appl. Phys. Lett., 53, 606-608, 1988.
10. K. Yoshiara, K. Kagata, S. Yokoyama, T. Hiroki, H. Higuma, T. Yamazaki, and K. Nakahigashi, Jpn. J. Appl. Phys., 27, L1429-L1494, 1988.
11. I. Dhingra, G. K. Padam, S. Singh, R. B. Tripathi, S. M. U. Rao, D. K. Suri, K. C. Nagpal, and B. K. Das, J. Appl. Phys., 70, 1575-1579,1991.
12. A. Bailey, S. L. Town, G. Alvarez, G. J. Russell, and K. N. R. Taylor, Physica C, 161, 347-350, 1989.
13. N. P. Bansal, R. N. Simons, and D. E. Farrell, High T_c Superconductor I, Am. Ceram. Soc., p 474-482, 1989.
14. Y. Matsuoka, E. Ban, and H. Ogawa, J. Phys. D: Appl. Phys., 22, 564-565, 1989.
15. J. M. Aponte and M. Octavio, J. Appl. Phys., 66, 1480-1482, 1989.
16. K. Przybylski, J. Koprowski, J. Oblakowski, and M. Wierzbicka, J. Less-Common Metals, 164-165, 470-477, 1990.
17. T. Tabuchi, Y. Shimakawa, A. Ochi, and K. Utsumi, High T_c Superconductor I, Am. Ceram. Soc.,p 464-473, 1989.
18. S. E. Dorris, M. T. Lanagan, D. M. Moffatt, H. J. Leu, C. A. Youngdahl, U. Balachandran, A. Cazzato, D. E. Bloomberg, and K. C. Gretta, Jpn. J. Appl.

Phys., 28, L1415-1416, 1989.
19. L. F. Goodrick and S. L. Bray, Cryogenics, 30, 667-677, 1990.
20. T. Brousse, R. Retoux, G. Poullain, J. Provost, H. Murray, D. Bloyet, and B. Raveau, Appl. Phys. A, 49, 217-220, 1989.
21. A. Uusimaki, I. Kirschner, J. Levoska, J. Levoska, G. Zsolt, Gy. Kovacs, T. Projesz, I. Dodony, S. Leppavuori, E. Lahderanta, and R. Laiho, Cryogenics, 30, 593-598, 1990.
22. T. Hashimoto, T. Kosaka, Y. Yoshida, K. Fueki, and H. Koinuma, Jpn. J. Appl. Phys., L384-L386, 1988.
23. K. Hoshino, H. Takahara, and M. Fukutomi, Jpn. J. Appl. Phys., L1297-L1299, 1988.
24. T. Nakamori, H. Abe, Y. Takahashi, T. Kanamori, and S. Shibata, Jpn. J. Appl. phys., L649-L651, 1988.
25. E. Gmelin, in Studies of High Temperature Superconductors, pp. 114-117, edited by A. Narlikar, Novva Sci. Publishers,1989.
26. W. D. Kingery, M. K> Bowen, and D. R. Uhlmann, Introduction to Ceramics, Wiley, New York.

Appendix I. Literature reviews of YBCO screen printed thick films.

Substrate	Binder	Firing Cond.	T_c(K)	J_c(A/cm^2)	Film Thickness(μm)	Reference
211	terpineol	930-960°C	83	-	50	1
MgO		10 min.	88	-		
YSZ		O_2	79	120		
$SrTiO_3$			50	-		
Al_2O_3			68			
Al_2O_3/Ag	Triethanolamine	950°C		0.012	100	2
		10 min.				
Al_2O_3	Du-Pont 9180	1000°C	70	-	10	3
Sapphire		30 min	79	9		
		O_2				
96% Al_2O_3	-	980 °C	68	90*	30-50	4
99.6% Al_2O_3		air	79	5*		
MgO			77	230*		
YSZ			86	30*		
Al_2O_3		1040°C	82	12.4	150	5
		10 min.				
		O_2				
Al_2O_3/		925°C	46		25	6
Y-Ba-Cu-O		1h./ air	88.5		100	

Substrate	Binder	Firing Cond.	T_c(K)	J_c(A/cm^2)	Film Thickness(μm)	Reference
Al_2O_3 Spinel		1000°C 15 min. O_2	66 81	-		7
YSZ/Ag		1050°C 10 min/O_2	88.5	700		8
YSZ MgO Sapphire		970-990°C 1-6 min. O_2	89 75 57	70	40 40 40	9
211 YSZ	diethylene terpineol	950°C 1 hour	86 85	3000	40 40	10
ZrO_2(MgO)	ethyl - cellulose	980°C 1-2 h/ O_2	90	20	25	11
Al_2O_3		1000°C 15 min./ O_2	66	-	40	13
YSZ		980°C 6min O_2	90(27% Ag) 87(Ag_2O) 77(pure)	190 3.5 0.013	- - -	14

Substrate	Binder	Firing Cond.	T_c(K)	J_c(A/cm^2)	Film Thickness(μm)	Reference
$SrTiO_3$		970-1000^{0}C	82	10	-	15
Sapphire			52	-	-	
$Zr(Ca)O_2$			80	0.1	-	
ZrO_2		1000^{0}C 6 min./ O_2	82	22	-	16
YSZ		970-990^{0}C	89	70	40	17
MgO		1-6 min	50	-	10	
Sapphire			43	-	10	

*: J_c was measured at 4.2 K.

AppendixII

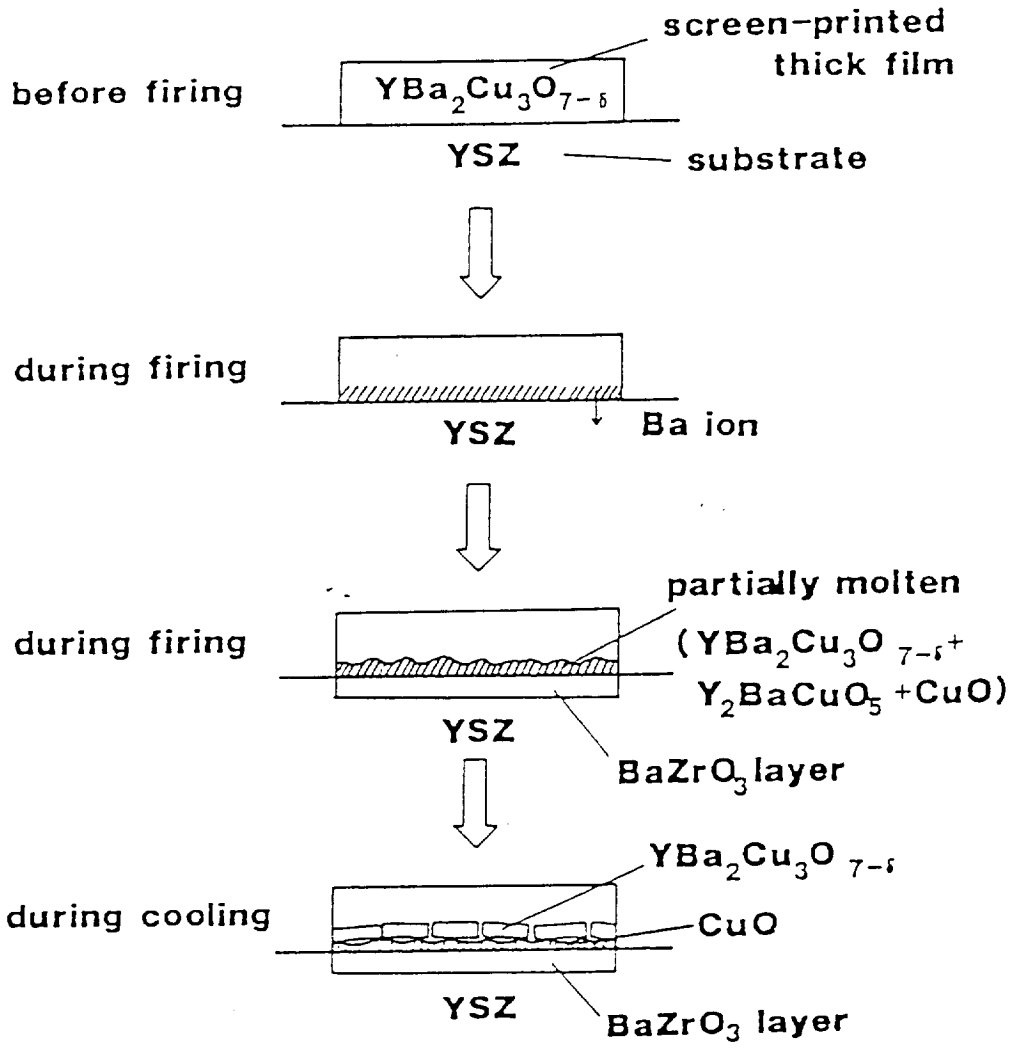

Figure A1: Schematic drawing of preferred orientation caused by interface reaction[17]. (after J. Tabuchi)

Appendix III.

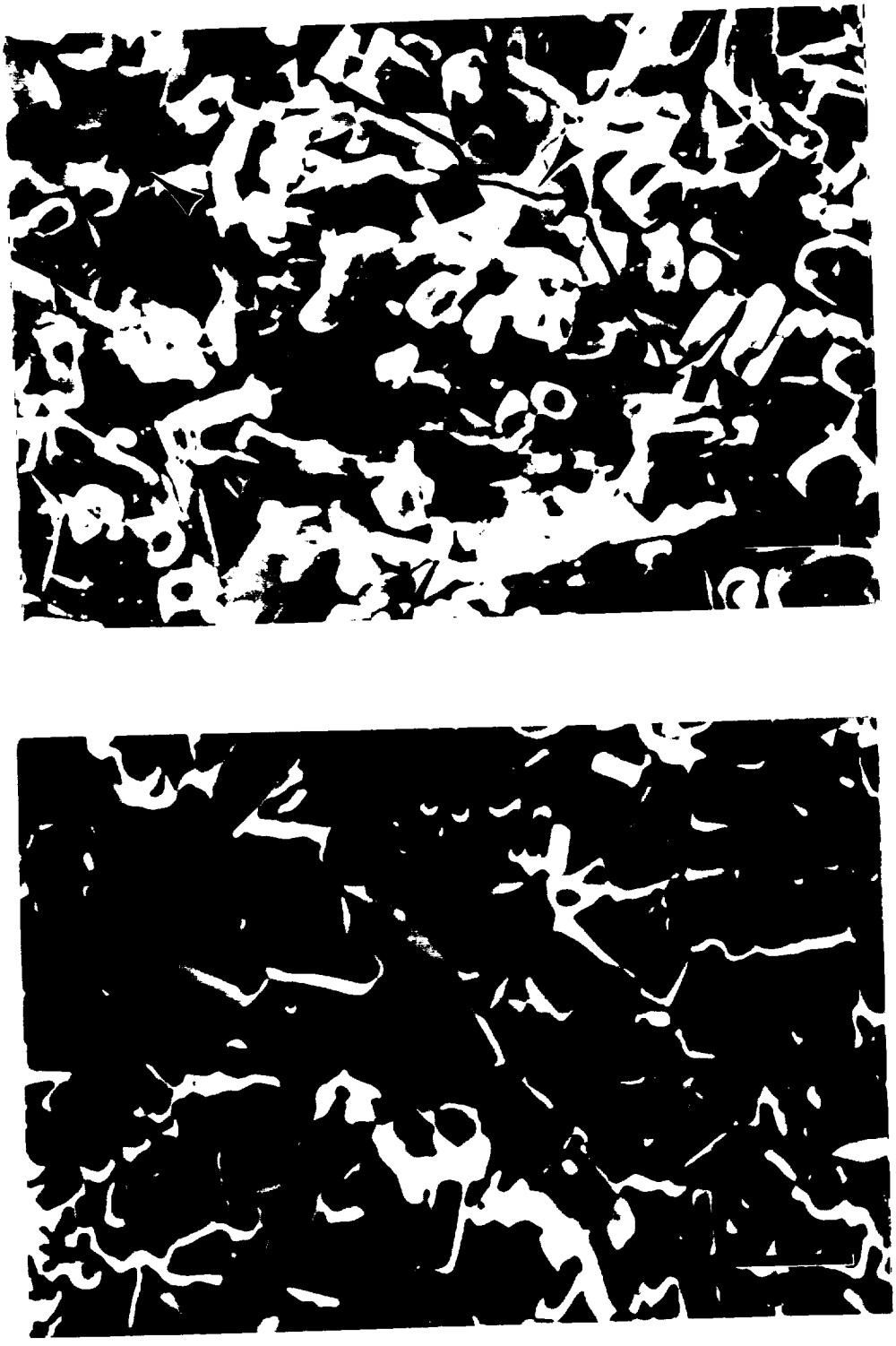

Figure A2: Microstructure of $YBa_2Cu_3O_{7-x}$ superconductor thick films with 10 (top) and 20wt% (bottom) Ag_2O on YSZ substrates. The films were fired at 970°C for 60 minutes. Bars equal to 10 μm.

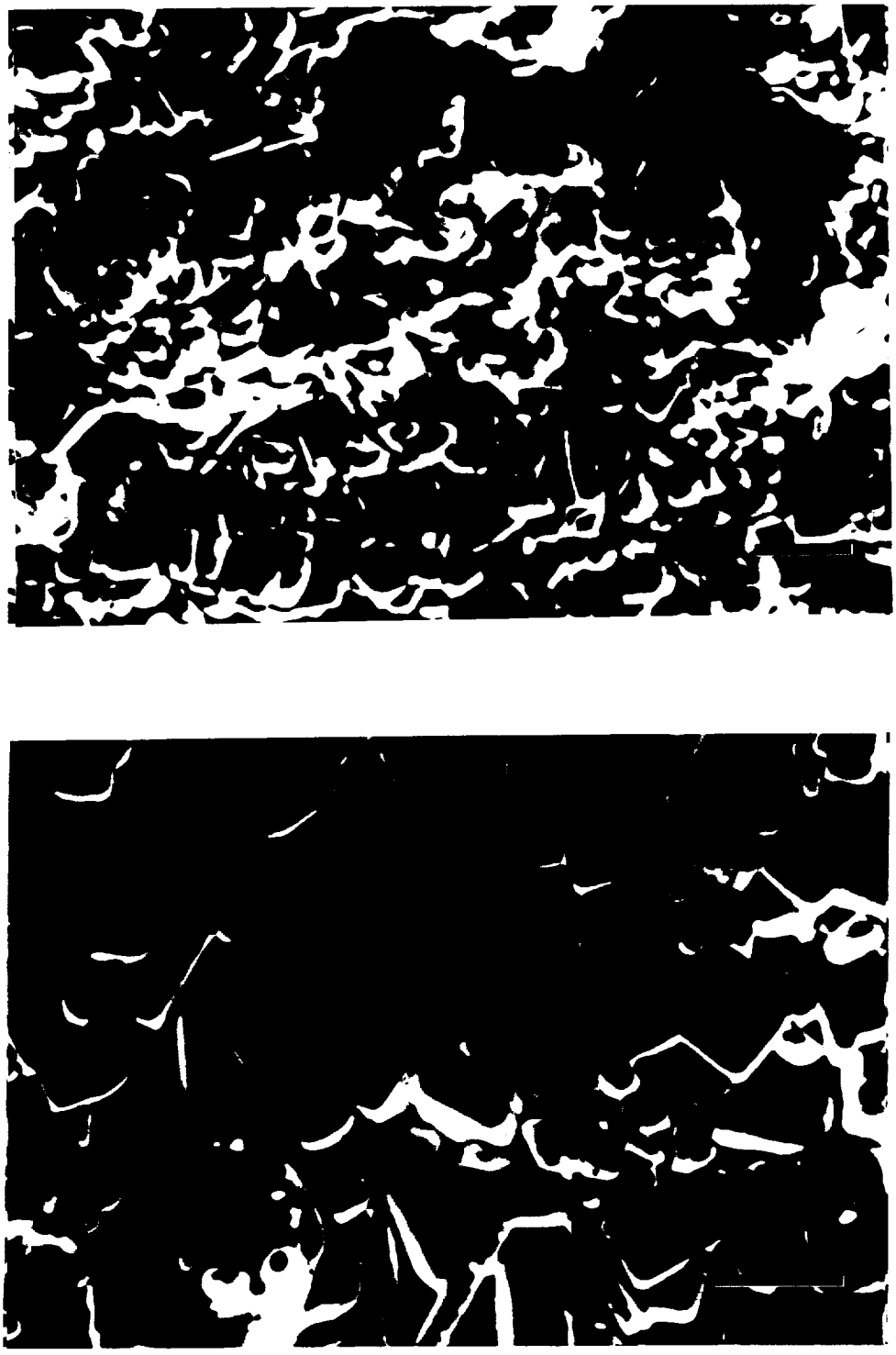

Figure A3: Microstructure of $YBa_2Cu_3O_{7-x}$ superconductor thick films with 10 (top) and 20wt% (bottom) Ag_2O on YSZ substrates. The films were fired at 980°C for 30 minutes. Bars equal to 10 μm.

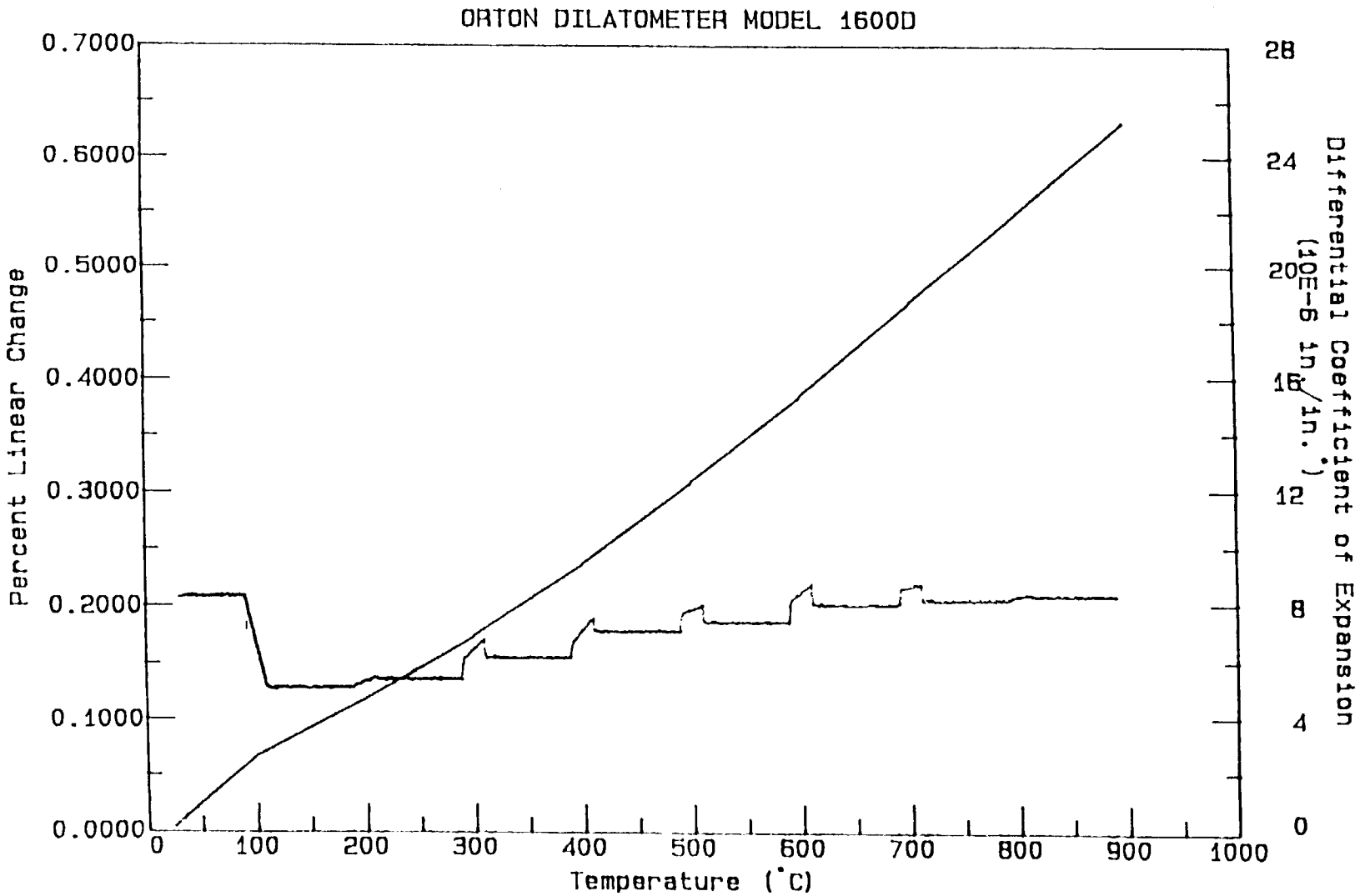

Figure A4:Thermal expansion of the YSZ substrate.

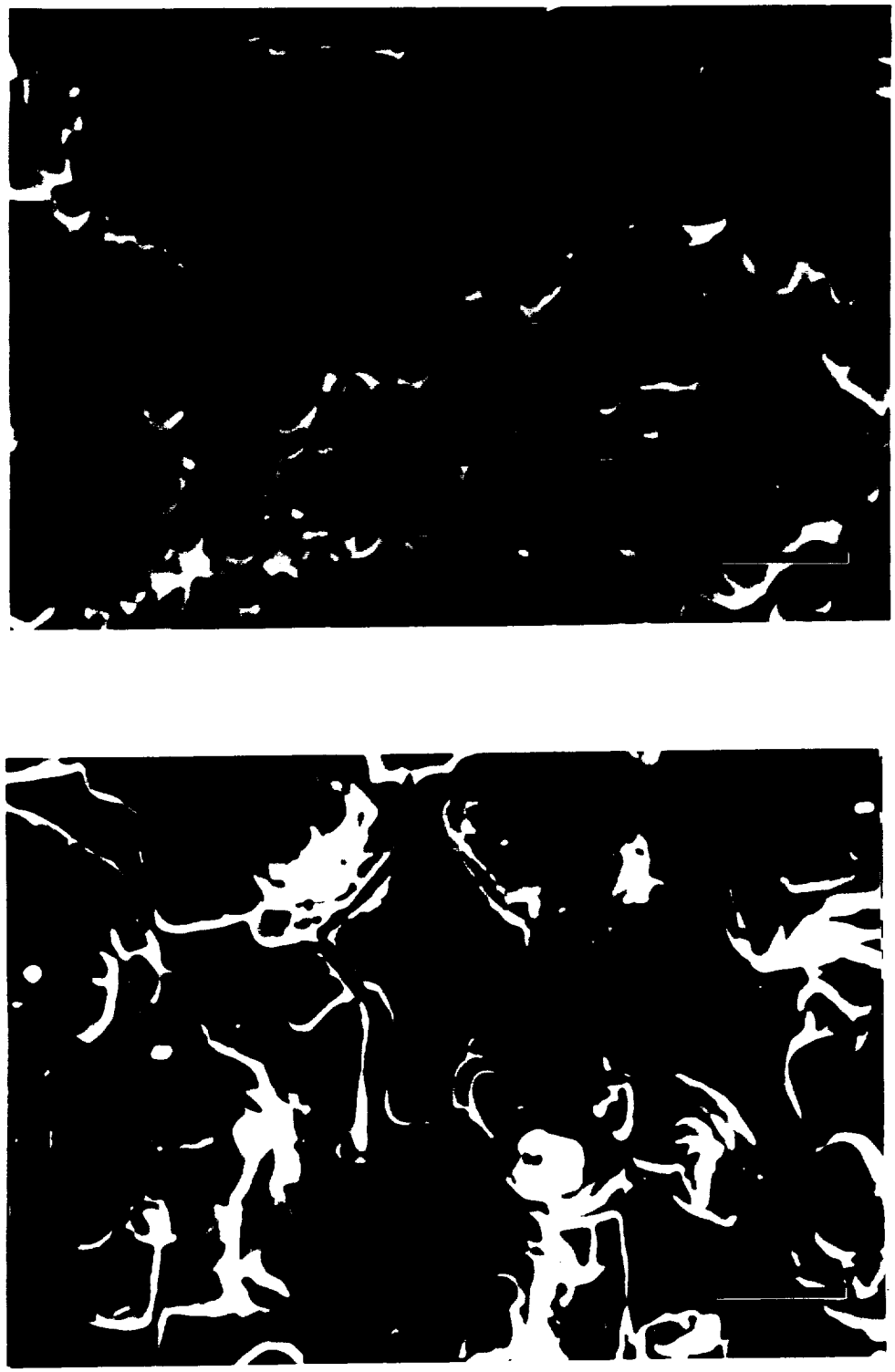

Figure A5:Microstructure of $YBa_2Cu_3O_{7-x}$ superconductor thick films with 10 (top) and 20wt% (bottom) Ag_2O on YSZ substrates. The films were fired at 990°C for 10 minutes. Bars equal to 10 μm.

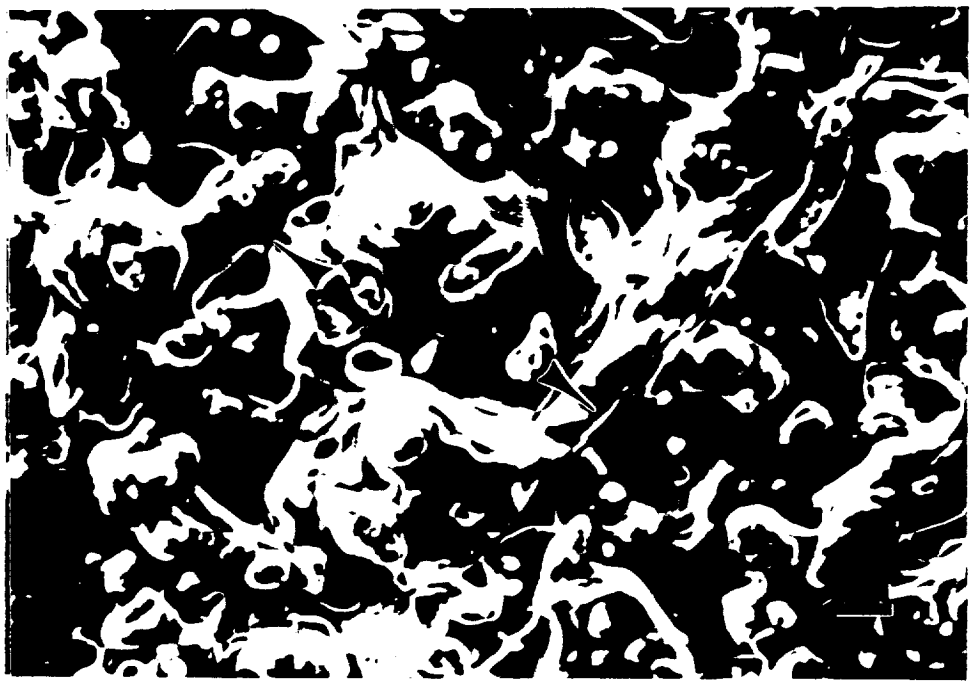

Figure A6: Microstructure of $YBa_2Cu_3O_{7-x}$ superconductor thick films with 20wt% Ag_2O on YSZ substrates. The films were fired at 980°C for 40 minutes. Bar equals to 10 μm.

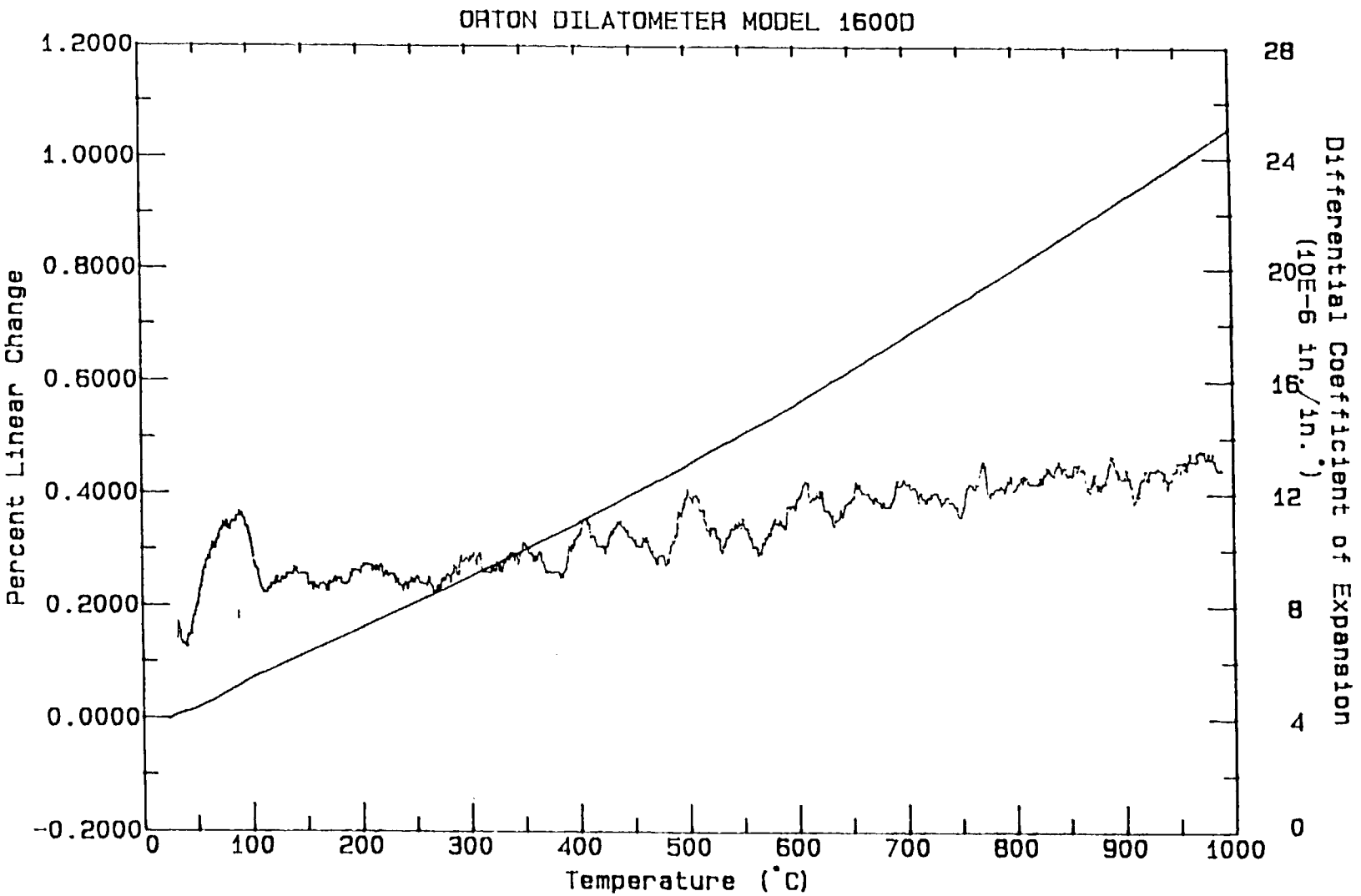

Figure A7: Thermal expansion of 12 mole% MgO-ZrO_2 substrate.

Appendix VII. Literature reviews of BSCCO screen printed thick films.

Substrate	Film Composition	Firing Cond.	T_c(K)	J_c(A/cm^2)	Reference
MgO	$Bi_{1.6}Pb_{0.4}Sr_{1.6}Ca_{2.4}Cu_3O_{10}$	865°C, 5h	101	10	20
MgO(100)	$Bi_{1.9}Pb_{0.4}Sr_{1.9}Ca_{2.1}Cu_{3.2}O_{10}$	895°C, 2h- 850°C, 80h	105	2000	21*
MgO(100)	$Bi_2Sr_2Ca_2Cu_3O_{10}$	900°C, 5 min.	62	-	17
YSZ		900°C, 1h	72	-	
YSZ	$Bi_2Sr_2Ca_2Cu_3O_{10}$	850°C, 1h	68	-	22
MgO(100)	$Bi_2Sr_2Ca_2Cu_3O_{10}$	885°C, 1h- 872°C, 72h	107	-	23*
Ag		880°C, 10 min.	76	-	
MgO(100)	$Bi_2Sr_2Ca_2Cu_3O_{10}$	890°C,1h- 870°C, 40h	<80	-	24*

*: Samples were annealed by two steps firing program.

Part II.

Annual Report

SUPERCONDUCTIVITY DEVICES: COMMERCIAL USE OF SPACE

Development of PBZT Ceramics for Electrostrictive Actuators

to

National Aeronautics and Space Administration
Langley Research Center
Hampton, VA 23665-5225

Principal Investigator:
Gene Haertling - Clemson University

Supporting Investigator:
Guang Li - Clemson University

Contract No. NAG-1-1301

August, 1992

1. Introduction

In recent years much attention has been paid to ceramic materials with large electrostrictive effects. Electrostriction, which exists in all materials, exhibits many potential applications in electronic and optically controlled system as well as precision machinery. Among the materials available so far, however, few possess electrostrictive effects large enough to be of practical usefulness. The development of new materials with high electrostrictive coefficients has been a major impetus of much research in this area. The $(Pb_{1-x}Ba_x)_{1-3z/2}Bi_z\,(Zr_{1-y}Ti_y)O_3$ ceramic system (PBZT) appears to be a very promising candidate because the electrostrictive effects of PBZT 27/70/30* in the system are among the largest discovered today [1].

A review of the present state of the technology in ceramic actuators is given in Figure 1. As seen from this figure, a variety of direct motional modes, composite structures and bending modes are employed to produce a given displacement. The maximum displacement per input volt is obtained with composite or bender structures, however, this is usually accomplished at the expense of (1) less load bearing capability, (2) greater complexity, (3) higher cost and (4) lesser reliability. It should be noted that in the simpler direct modes, both piezoelectric and electrostrictive materials are usable; however, the electrostrictors can be driven to higher fields (and hence, higher strains) because they are not limited by ferroelectric domain switching. For example, piezoelectric materials are limited to less than 25 volts/mil (10 kV/cm) due to domain switching which leads to 'walk off', but the electrostrictive materials can be used to much higher (50 – 100 volts/mil) fields.

Examples of the strain characteristics of two high strain materials: i.e., PMN:PT and PBZT, are given in Figure 2. Of these, the PBZT materials possess higher intrinsic total strain; and thus, were selected for further investigation.

In this report we will present the results of an investigation of $(Pb_{1-x}Ba_x)_{1-3z/2}Bi_z\,(Zr_{1-y}Ti_y)O_3$ ceramic system with $0.25 \leq x \leq 0.43$, $0.28 \leq y \leq 0.53$ and $0 \leq z \leq 0.02$ extending from the composition 27/70/30. The preparation and sintering of samples as well as the measurement of the electros-

* in this report the notation commonly used to describe the compositions of PLZT ceramics is used for PBZT, where 27 represents the mole percentage of barium content in A–site of perovskite structure and 70/30 the Zr/Ti radio in B–site.

trictive and related properties are described. We will also discuss the characteristics of the PBZT phase diagram on the basis of the results obtained. In addition, the preparation and evaluation of two PMN:PT compositions are included for comparison with the PBZT materials.

2. Sample Preparation and Sintering

The compositions of PBZT ceramics chosen to be investigated in this report are situated along two lines in $BaZrO_3$–$BaTiO_3$–$PbZrO_3$–$PbTiO_3$ phase diagram, which is depicted in Figure 3; i.e., the vertical line along which the Pb/Ba ratio is changed while the Zr/Ti is kept constant, and the horizontal line where, conversely, the Pb/Ba is constant and the Zr/Ti changed. The two lines intersect at the composition 27/70/30.

All the PBZT samples were prepared and sintered in terms of conventional mixed–oxide processing of electronic ceramics. A flowchart of the processing is given in Figure 4. Reagent grade PbO, ZrO_2, TiO_2, $BaCO_3$ and Bi_2O_3 additive were used as starting raw materials. Weighed components were first mixed for 30 minutes, and then calcined at 925 °C for two hours. The calcined powder was milled in distilled water using Al_2O_3 balls for 6 hours. Sample pellets were obtained by pressing the milled powder with distilled water into plates of about 30x30x4 mm at a pressure of 7000 psi. The samples were sintered at 1250–1280 °C for 4 hours in a closed alumina crucible with a flowing oxygen atmosphere. To avoid the loss of PbO from samples during sintering, a PbO–rich atmosphere was maintained by placing an equalmolar mixture of PbO and ZrO_2 in the crucible. Sintered samples were then lapped to dimensions of 10x10x0.76 mm. The opposite sides of the lapped samples were electroded with electroless nickel electrodes.

The PMN:PT samples, PMN:PT1 (0.8375PMN–0.1375PT–0.025BT) and PMN:PT2 (0.986PMN–0.0889PT–0.0125BT), were also prepared via a mixed–oxide method. Reagent grade $MgCO_3$ and Nb_2O_5 were mixed for 1 hour and calcined at 1100 °C for 15 hours to synthesize the columbite structure $MgNbO_6$. This step is believed to be helpful in order to minimize the concentration of undesirable pyrochlore phase in the final PMN:PT product [2]. The $MgNbO_6$ powder was then mixed with PbO, TiO_2 and $BaCO_3$ for 1 hour, and calcined at 800°C for 4 hours to produce

PMN:PT. The remaining preparation procedures employed for PMN:PT were identical to those for PBZT expect that PMN:PT samples were sintered at 1185 °C for 3 hours. The sintered PMN:PT samples were examined by an X–ray diffractometer to confirm the perovskite structure expected. An example of PMN:PT X–ray diffraction pattern is shown in Figure 5. As seen in the figure, the pyrochlore phase was constrained to less than 3 volume percent. Lapped samples were deposited with electroless nickel or sputtered copper electrodes for the evaluation of properties.

Some of PBZT and PMN:PT samples were also fabricated by hot–pressing.

3. Sample Measurements

The dielectric properties of samples were measured at 1 kHz with an LCR meter (LEADER, LCR–7450–01). The temperature dependence of dielectric constant and loss factor were obtained by placing samples in an environmental chamber (DELTA DESIGN, 1740) in which samples were first cooled down to –20 °C and then measured at a heating rate of 2–3 °C/min up to 140 °C. The measurement of relationship between polarization (P) and electric field (E) was carried out using conventional P–E hysteresis loop equipment. The submersion method in distilled water was employed to evaluate sample density.

An experimental device using an LVDT as a displacement sensor, was made to detect the change of electrostrictive strains with electric field, which is depicted in Figure 6. Electroded samples were placed in line with the movable core of the LVDT which was held in place with a light spring in compression. Sample electrodes were parallel or perpendicular to the movable core depending on the measurement of lateral or longitudinal strain. A liquid holder was employed to contain Freon into which samples were immersed so that electric shorting during the application of electric field could be avoided. An electric field was applied to the samples continuously between negative and positive maxima. The measured results were recorded on a X–Y plotter. The sensitivity of the displacement detection was limited basically by electronic and background vibration noises. The sensitivity of the device was estimated to be 0.1 μm at a signal/noise ratio of 1.

3. Results and Discussion

The important data of PBZT samples of different compositions obtained in this study are illustrated in Table 1. The values of the dielectric constant at room temperature lie in the range from 2250 to 7790 depending on the composition of the samples. The dielectric constant of the compositions along the vertical line in the phase diagram experienced a maximum as the barium content in the A–site of the perovskite structure increased across the boundary of the rhombohedral and cubic phases, which were plotted in Figure 7. As is often the case, the maximum dielectric constant signified the phase boundary, which appeared at a composition somewhere between 29/70/30 and 32/70/30. Figure 7 also shows a similar situation occurring along the horizontal line, where the maximum in dielectric constant indicates the rhombohedral and tetragonal phase border which is located near the composition 27/68/32.

The temperature dependence of dielectric constant and loss factor for a number of selected PBZT compositions was studied. These results are given in Figures 8 and 9. All the compositions shown in the figure were characterized by a diffuse phase transition (also called relaxor transition), a type of transition that occurs at a broad range of temperatures and is manifested as a corresponding broad maximum in the change of dielectric constant with temperature. The temperatures at which the dielectric constants reached the maxima were considered to be the temperatures of transition from the rhombohedral or tetragonal ferroelectric to the paraelectric phases. The transition temperature for the compositions along the vertical line decreased, as expected, with increasing barium content.

The sample densities exhibited no significant change for the compositions studied. The slight reduction in densities with increasing barium concentration could be interpreted as due to the decrease of lead content. Higher sintering temperatures were required for the compositions with less lead. Scanning electron photomicrographs of fractured surfaces, as seen in Figure 10, show that the sintered samples were well densified with few pores and possessed homogeneous grain sizes of approximately 5 μm. It was found experimentally that the samples with smaller Zr/Ti ratio were more easily sintered to maturity, which is indicated by their higher densities.

The relationships between polarization and electric field for the samples with constant Zr/Ti ratio

are demonstrated in Figure 11. A slim–loop characteristic was found for all these samples. Hysteresis became narrow with increasing barium content. At the same time P_{10}, the polarization at an electric field of 10 kV/cm, decreased monotonically, as shown in Table 1. Nearly linear P–E relationships with negligible hysteresis were obtained at the compositions having barium concentrations larger than 32 mol% suggesting that the samples were in the paraelectric cubic phase region. As clearly illustrated by the P–E curves in Figure 12, the characteristics of the samples with constant Pb/Ba ratio changed successively from diffuse phase to the rhombohedral phase and then to the tetragonal phase as the Zr/Ti ratio decreased. In all cases, the P–E curves could be divided into two parts. At low electric field, polarization increased rapidly with electric field. After reaching a certain magnitude, which depends on composition, polarization became saturated. The temperature dependence of P–E relationship for the composition 27/70/30 was measured. As seen in Figure 13, it looks similar to the corresponding compositional dependence. But the reoccurrence of large hysteresis shown in the figure above a certain temperature is beyond expectation and worthy of further study since it is concerned with temperature characteristics of electrostrictive properties. It will be seen in the following discussion that electric field induced strains have a close relation with polarization.

Both longitudinal and lateral electrostrictive strains were investigated. The curves of strains vs. electric field for various PBZT compositions are presented in Figures 14, 15 and 16. $S_{1,10}$ and $S_{2,10}$ (the magnitudes of longitudinal and lateral strains, respectively, at an electric field strength of 10 kV/cm), which are representative of the potential applications of electrostrictive materials, were evaluated and are listed in Table 1. As anticipated, it was found that strains were intimately related to polarization induced by electric field. Large strains generally corresponded to large polarization; strains appeared saturated at high electric field and the hysteresis of strains was also considered to be attributed to that of polarization. In addition, the strain(S)–electric field(E) relationship was observed to be strongly compositionally dependent. The butterfly–like S–E curve for the composition 27/47/53 was generated from a tetragonal ferroelectric phase. For the compositions whose strain–electric field hysteresis was small, the strains were plotted against the square of the electric field, which is shown in Figure 17. As seen in the figure, the S and E^2 approach a linear relationship in

low electric field region, which is typical of electrostrictive materials. The electrostrictive coefficients, m_{11} (longitudinal) and m_{12} (lateral), for those compositions shown in Figure 17 were calculated according to the slope of the linear curves in the figure, and are displayed in Table 1. The longitudinal electrostrictive coefficients were found to be between 2–3 times as large as the lateral. The PBZT hot–pressed sample exhibited larger saturated strains and slightly smaller hysteresis, as shown Figure 18, compared with those under normal sintering due to the smaller grain size of the former. More discussion about this will be taken up later.

For comparison, two PMN:PT compositions with large electrostrictive strains were studied. The results are given in Table 2 and Figures 19 and 20. Although the shape and magnitude of the P–E relationship for the PMN:PT samples resemble those of PBZT ceramics in the vicinity of the composition 27/70/30, the PMN:PT values of $S_{2,10}$ are much lower than PBZT. This result clearly shows that PBZT ceramics are superior to PMN:PT in electrostrictive properties. Hot–pressing appeared to have no effect on the magnitude of electrostrictive strain but dramatically reduced dielectric constants, probably because of the smaller grain size of the hot–pressed samples. The increase of hysteresis for the hot–pressed PMN:PT2 sample is not fully understood.

The earliest systematic investigation of pure $PbZrO_3$–$PbTiO_3$–$BaZrO_3$–$BaTiO_3$ system was preformed by Ikeda [3]. His work mainly focused on the phase diagram near $BaTiO_3$ with small amounts of Pb and Zr concentrations as well as on the F_R (rhombohedral ferroelectric) and F_T (tetragonal ferroelectric) phase boundary. The phase diagram shown in Figure 3 was extracted from Ikeda's publication. A significant difference was observed between the boundaries for both the F_R–F_T and F_R–P_C (paraelectric cubic phase) as given by Ikeda and those based on our results (the composition with a maximum dielectric constant). A reason for this difference is discovered to be due to the small amount of dopant (2 atom % Bi_2O_3) added to the pure PBZT system in our investigation. The influence of the Bi_2O_3 additive on the physical properties of several PBZT ceramics are demonstrated in Table 1, Figures 21, 22 and 23. It can be seen in Figure 21 that the additive not only shifted the Curie points to lower temperatures but also significantly enhanced dielectric constants of the pure PBZT ceramics. Besides, a small amount of the additive reduced the hysteresis

of P–E curves by modifying sample microstructures, and increased sample density. In studying electric field induced strains of PBZT ceramics near the F_R and F_T boundary, Hagimura et al [4] also discovered that a few percent additive of other rare earth elements could remarkably change the strain properties which were related to the phase structures. Further investigation is needed for better understanding of the significant effect of additives on the PBZT ceramic properties.

Grain size is not supposed to have any effect on the electrostrictive strains of relaxor materials because the relaxor phenomenon originates from the compositional fluctuation in 10 nm dimensional regimes. But it was found, as was mentioned previously, that smaller grain size obtained by hot–pressing could reduce strain hysteresis in the composition 26/70/30, even though the temperature dependence of dielectric constant in this composition exhibited a broad maximum characterized by relaxor materials. Based on this grain size effect and the variation of electric field induced strain properties (magnitude and hysteresis) with composition, it is believed that there exists a region in the PBZT phase diagram where rhombohedral phase and diffuse phase coexist. This region at least covers the dark shadowed area shown in Figure 3. It could be much larger. The large strains found in this compositional region could be explained as resulting from the combined consequence of electrostrictive effects and domain reorientation of the rhombohedral phase under electric field. A similar result was also discovered by J. von Cieminiski et. al. [5]. It is this region in the PBZT phase diagram that provides greatest practical high strain compositions.

4. Conclusions

The main objective of this study was to exploit the potential applications of PBZT ceramics as actuators. A compositional region was identified in the Bi_2O_3 doped PBZT phase diagram where large electrostrictive strains and small hysteresis exist simultaneously. The $S_{1,10}$ could be as high as 12.5×10^{-4} and strain hysteresis may be small enough to be negligible depending on the composition involved. The excellent electrostrictive properties in this compositional region is considered as to be caused by the combined consequence of electrostrictive effects and ferroelectric domain wall motion. The Bi_2O_3 additive was found to play a dominant role in improving the properties of

pure PBZT ceramics. A small amount of the additive can significantly enhance the electrostrictive and dielectric properties of PBZT ceramics probably by means of improving sinterability and microstructures. In addition, large displacements for both the F_R–F_T and F_R–P_C phase boundaries resulting from the additive were discovered.

It was found that PBZT ceramic materials are superior to PMN:PT in many aspects if used as actuator materials. First, PBZT ceramics possess much larger intrinsic electrostrictive strains than PMN:PT. Secondly PBZT ceramics are easy to fabricate and relatively insensitive to sintering conditions whereas PMN:PT requires complicated preparation procedures and the undesirable pyrochlore phase in PMN:PT is hard to eliminate, which significantly degrades material properties. Finally much lower dielectric constant in PBZT compared with PMN:PT is also considered as another major advantage of PBZT ceramics from the viewpoint of electrical to mechanical energy conversion

The electrostrictive properties of PBZT ceramics can be further improved after a better understanding of the system is obtained. Further investigation is thus of practical as well as theoretical significance.

5. References

[1] K. M. Leung, S. T. Liu and J. Kyonka, Ferroelectrics, vol. 27, p41 (1980).

[2] S. L. Swartz and T. R. Strout, Mat. Res. Bull., vol. 17, p1245 (1982).

[3] T. Ikeda, J. Phys. Soc. Japan, vol. 14(2), p168 (1959).

[4] A. Hagimura and K. Uchino, IEEE International Symposium on Applications of Ferroelectrics, p185 (1990).

[5] J. von Cieminski and H. Beige, J. Phys. D: Appl. Phys., vol. 24, p1182 (1991).

Table 1. Properties of the $(Pb_{1-x}Ba_x)_{1-3z/2}Bi_z(Zr_{1-y}Ti_y)O_3$ ceramics.

z=0.02

Ba/Zr/Ti	Dielectric constant	Loss factor (%)	Density (g/cm^3)	P_{10} ($\mu C/cm^2$)	$S_{1,10}$ x 10^4	$S_{2,10}$ x 10^4	Electrostrictive Coeff.* m_{11}	m_{12}
25/70/30	5830	9.5	7.28	25.6	11.2	4.47		
26/70/30	6110	9.7	7.22	21.4		3.46		3.85
27/70/30	6400	10.0	7.19	18.0	8.0	3.10	8.5	3.25
29/70/30	7680	12.8	7.07	11.3	2.9	1.20	3.7	1.35
32/70/30	7790	6.6	7.05	9.1		0.65		0.75
35/70/30	6230	2.3	6.99	6.8		0.33		
43/70/30	5940	2.0	6.94	5.3		0.33		
27/72/28	6480	10.1	7.18	16.5	8.5	2.57	8.9	3.25
27/68/32	7450	11.1	7.19	16.5		2.47		2.75
27/64/36	6090	10.8	7.26	18.0		2.73		
27/60/40	5230	8.4	7.30	21.5		3.75		
27/57/43	5140	8.0	7.36	24.2		5.67		
27/55/45	4760	7.8	7.34	24.1	12.5	5.67		
27/47/53	2250	4.0	7.36					

Hot–pressing

26/70/30	6370	9.4	7.49	19.3		3.13		3.75

z=0.00

27/70/30	3670	5.4	6.88	16.2		2.67		
27/60/40	4270	5.4	6.92	21.0		3.75		
32/70/30	5780	4.8	6.84	8.9		0.95		

Table 2. Properties of the PMN:PT ceramics.

	Dielectric constant	Loss factor (%)	Density (g/cm^3)	P_{10} ($\mu C/cm^2$)	$S_{1,10}$ x 10^4	$S_{2,10}$ x 10^4	Electrostrictive Coeff.* m_{11}	m_{12}
PMN:PT1	17020	5.3	7.68	16.7	3.75	1.75		2.2
PMN:PT2	19100	5.6	7.79	14.9		1.35		1.4

Hot–pressing

PMN:PT2	12750	3.5	8.25	16.4		1.35		1.4

* $x10^{16}$ (m^2/V^2)

CERAMIC ACTUATOR TECHNOLOGY

Type	Configuration	Load Cap. (lbs.)#	Actuator Movement w/voltage	Actuator Behavior (P or E)*	Actuator Strain (%)**	
					25	100
Monolithic (d_{33} mode)	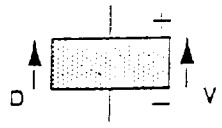	800	Expansion	P	.07	N/A
Monolithic (d_{31} mode)	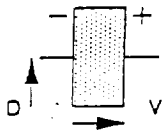	800	Contraction	P	.03	N/A
Monolithic (s_{11} mode)	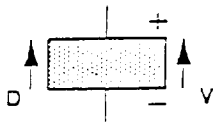	800	Expansion	E	.07	.20
Monolithic (s_{12} mode)	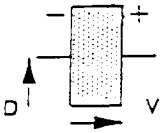	800	Contraction	E	.03	.08
Composite Structure (d_{33} mode) (flexten.)	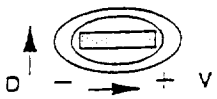	350	Contraction	P	.54	N/A
Composite Structure (d_{33}/d_{31}) (moonie)	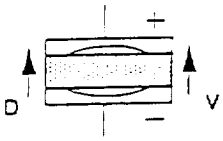	30	Expansion	P	.80	N/A
Monomorph (Bender)	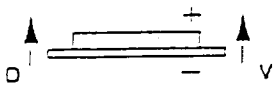	<1	Expansion/ Contraction	P	1.5	N/A
Bimorph (Bender)	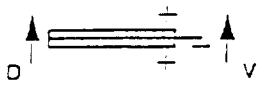	<1	Expansion/ Contraction	P	15.0	N/A

Notes: V = Voltage, D = actuator displacement
\# Maximum load on a 3/4 inch diameter rod
* P = Piezoelectric, E = Electrostrictor
** Strain values at ±25 V/mil (10 kV/cm) & ±100 V/mil (40 kV/cm)

Figure 1.

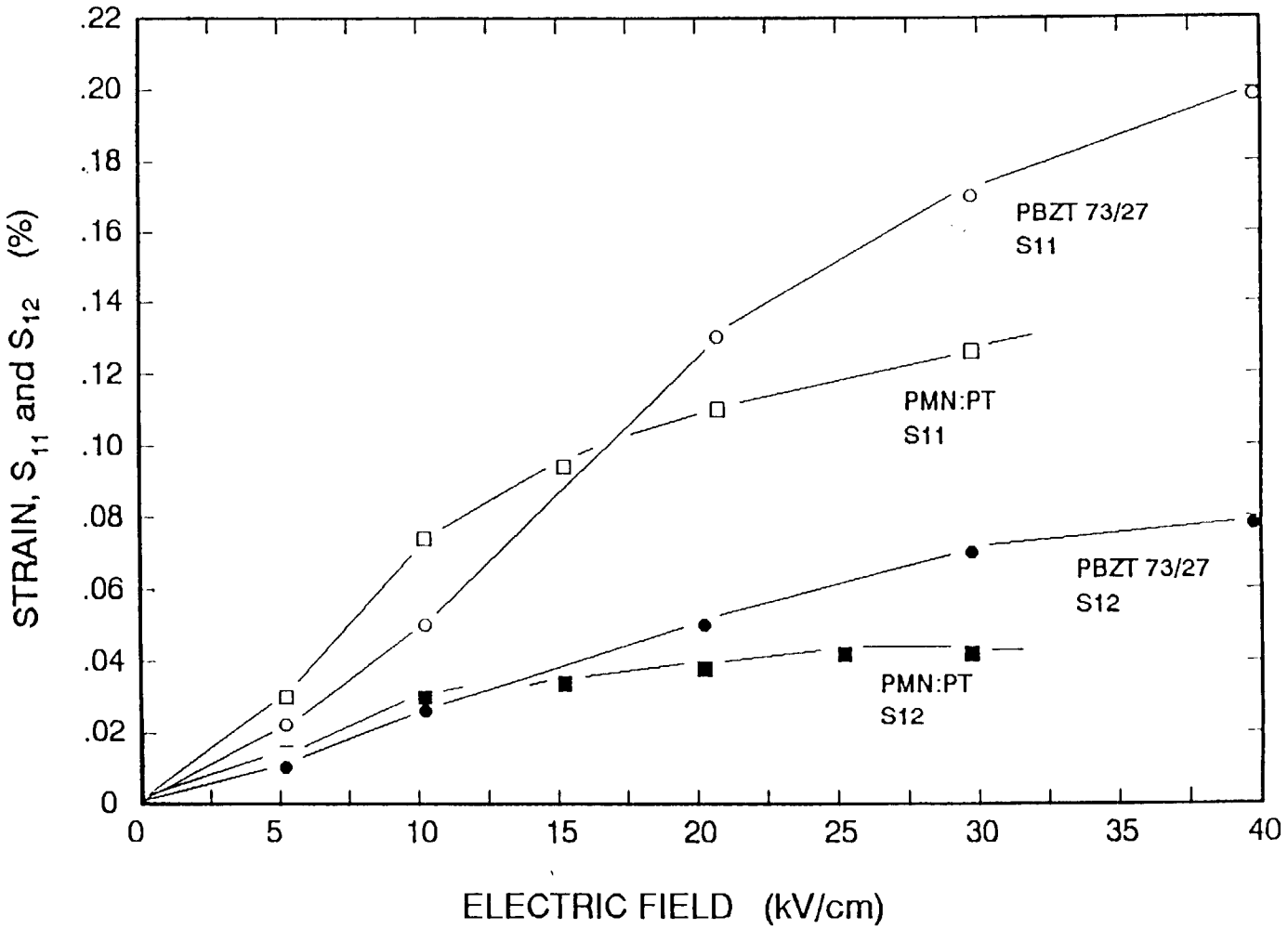

ELECTROMECHANICAL STRAIN BEHAVIOR OF ELECTROSTRICTIVE ACTUATORS .

Figure 2.

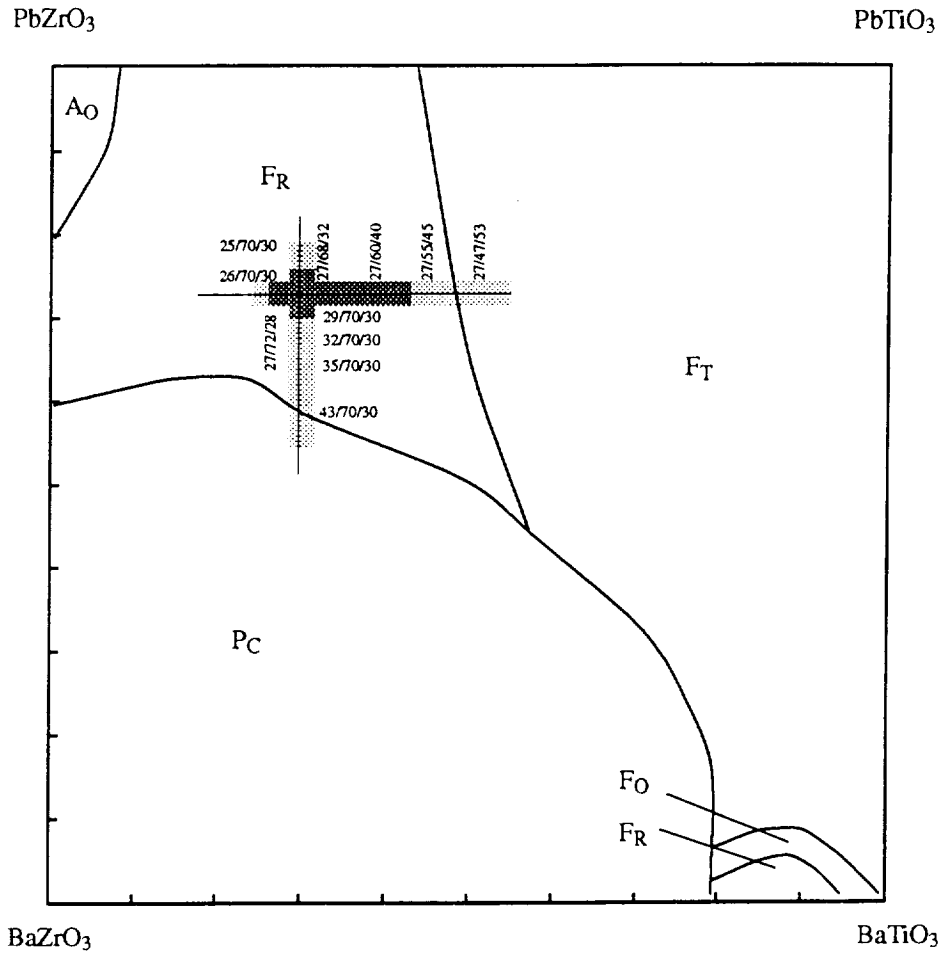

Figure 3. Room temperature phase diagram for the system $PbZrO_3$–$PbTiO_3$–$BaZrO_3$–$BaTiO_3$ (PBZT). where F_R denotes rhombohedral phase, F_T tetragonal phase and P_C paraelectric phase [3].

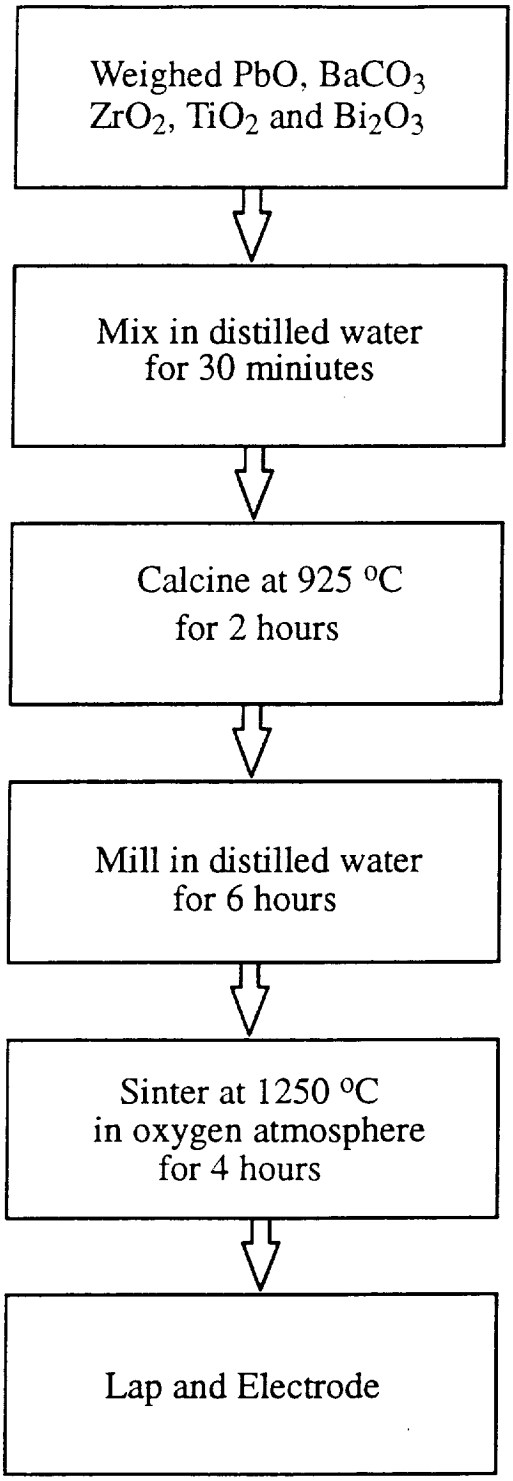

Figure 4. Flowchart of PBZT processing.

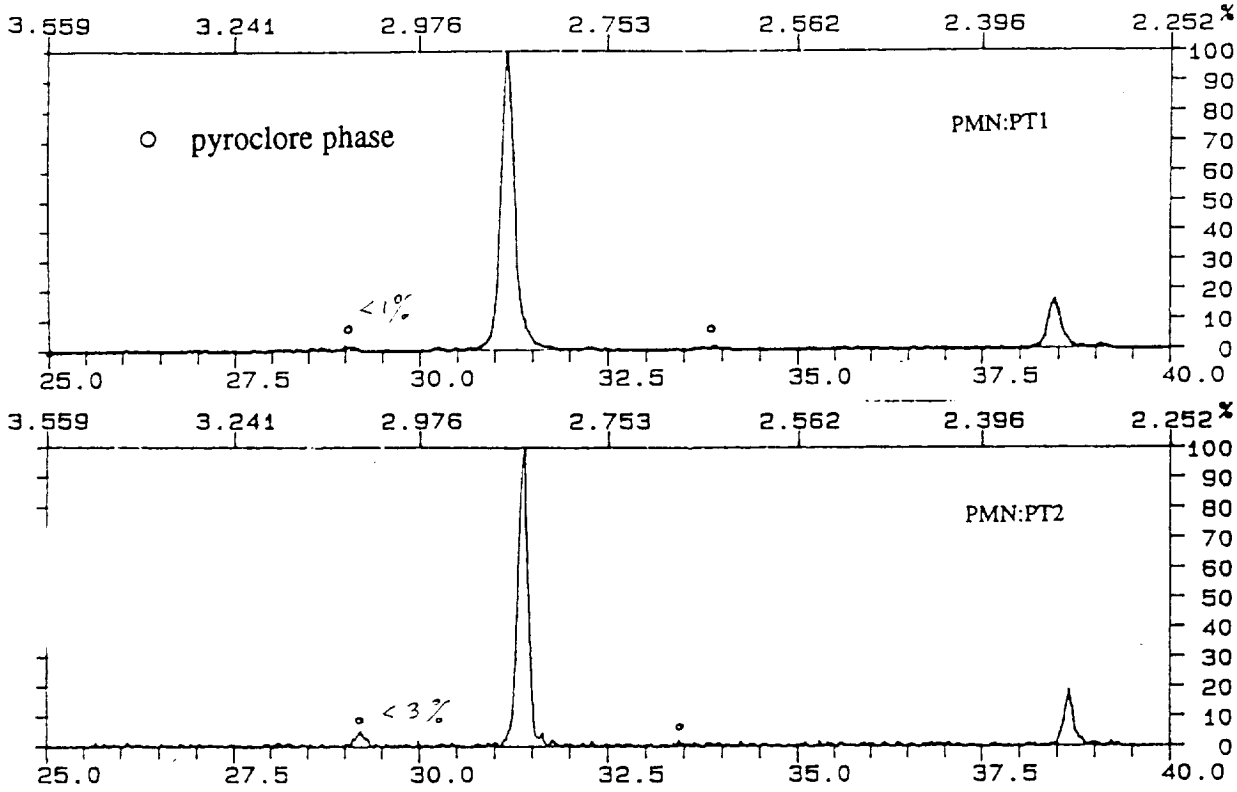

Figure 5. X–ray diffraction pattern of PMN:PT ceramics.

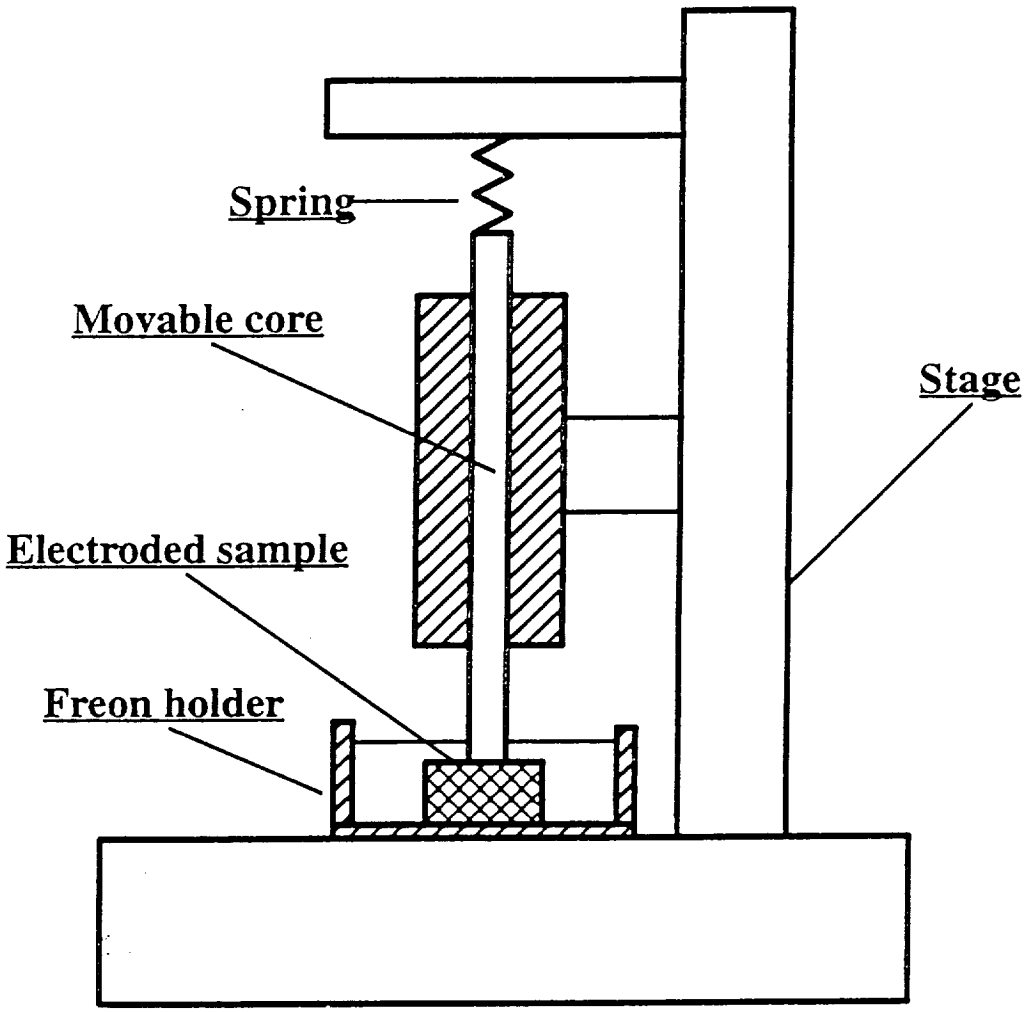

Figure 6. The LVDT device for measurement of electrostrictive strains

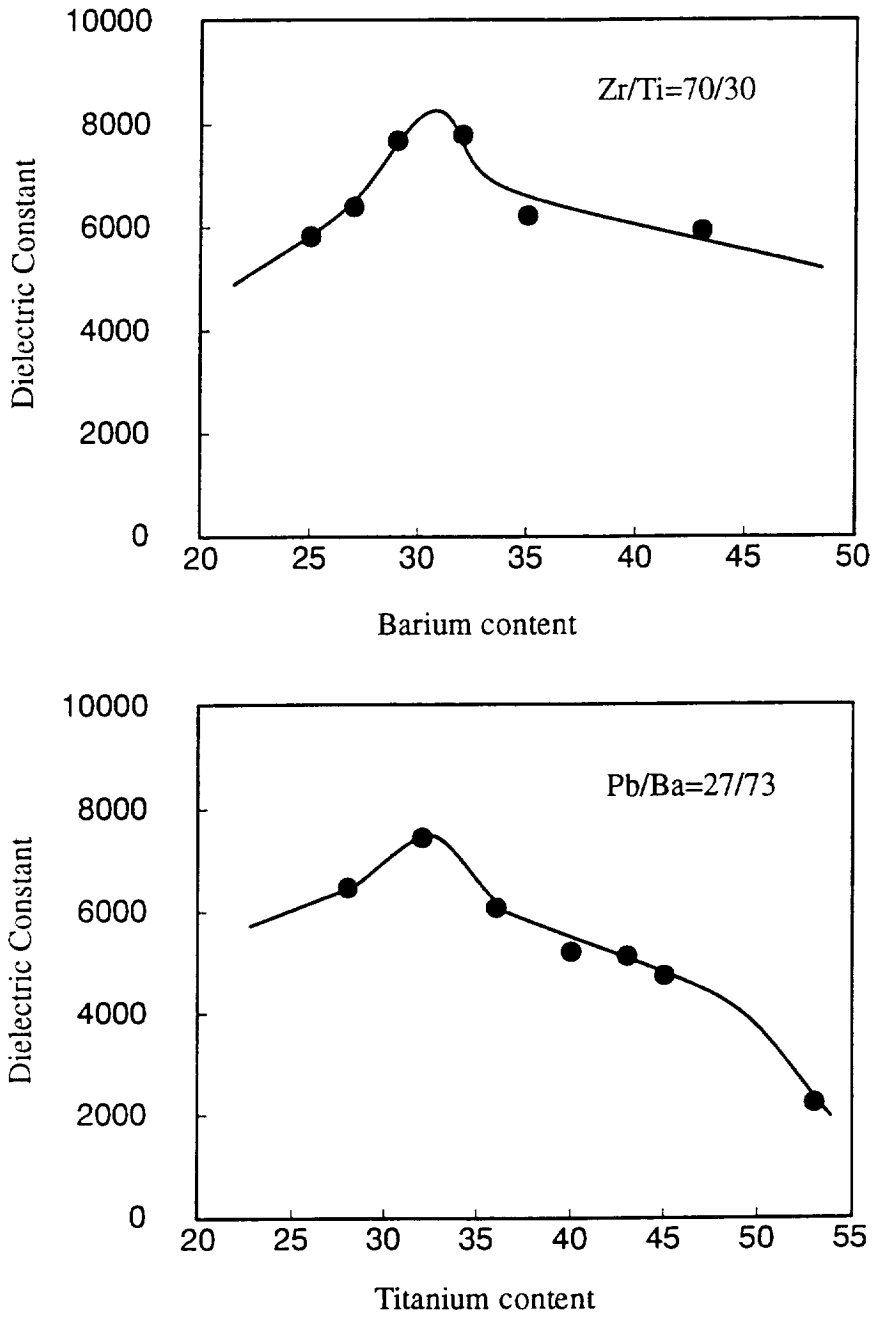

Figure 7. Variation of dielectric constant with PBZT composition.

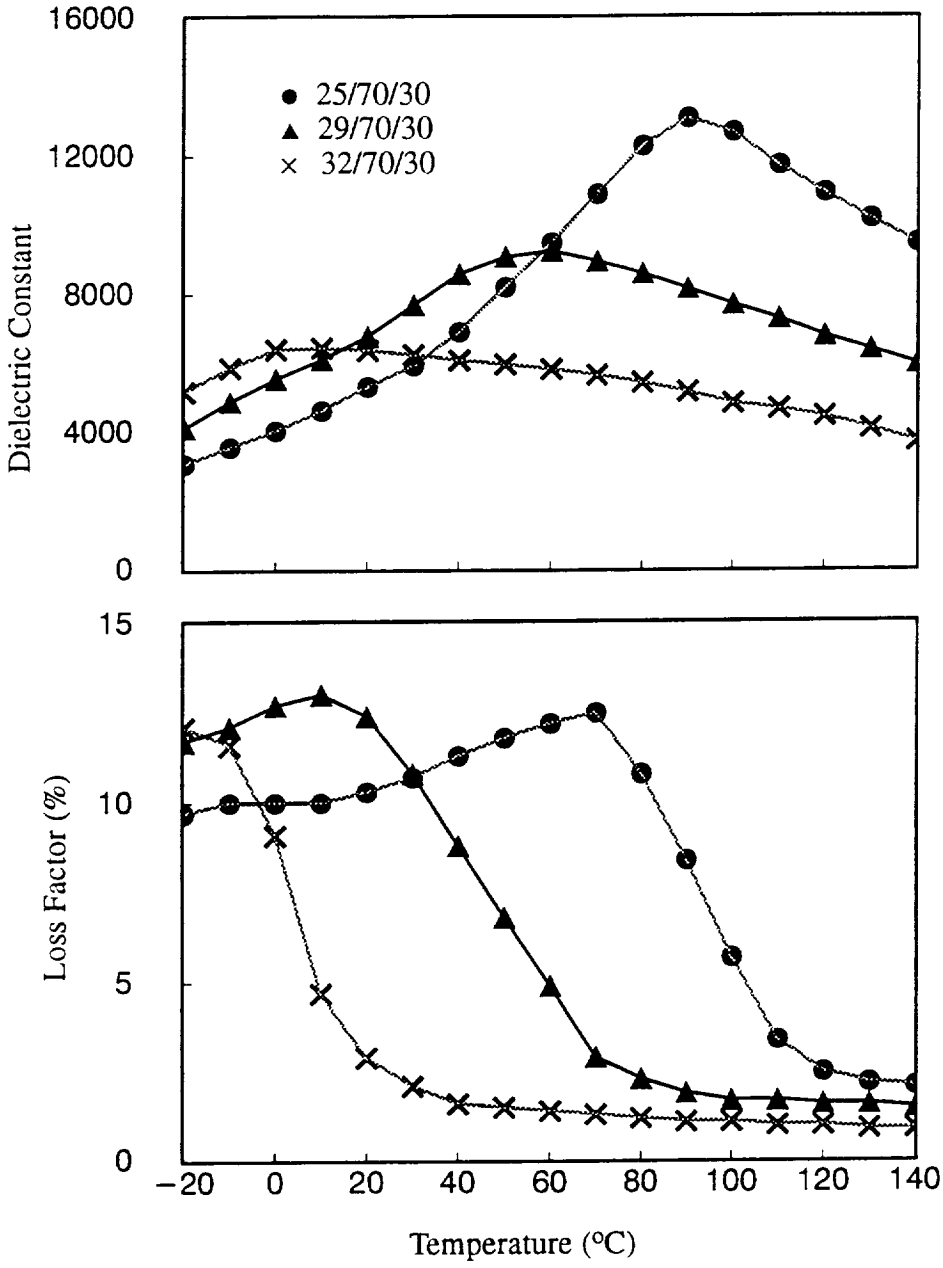

Figure 8. Temperature dependence of dielectric constant and loss factor for various PBZT compositions with constant Zr/Ti ratio.

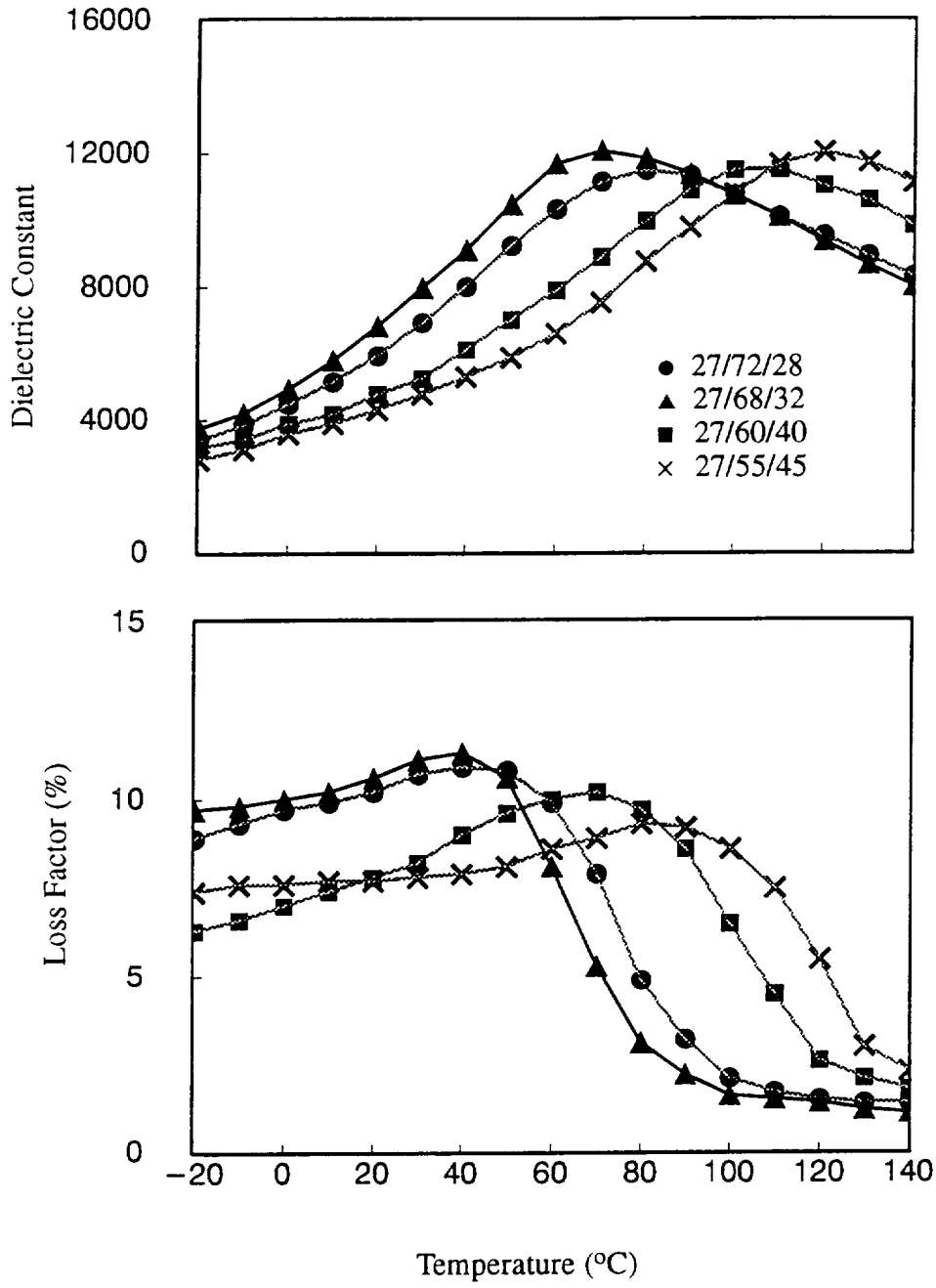

Figure 9. Temperature dependence of dielectric constant and loss factor for various PBZT compositions with constant Pb/Ba.

Figure 10. SEM photomicrographs of PBZT ceramics.

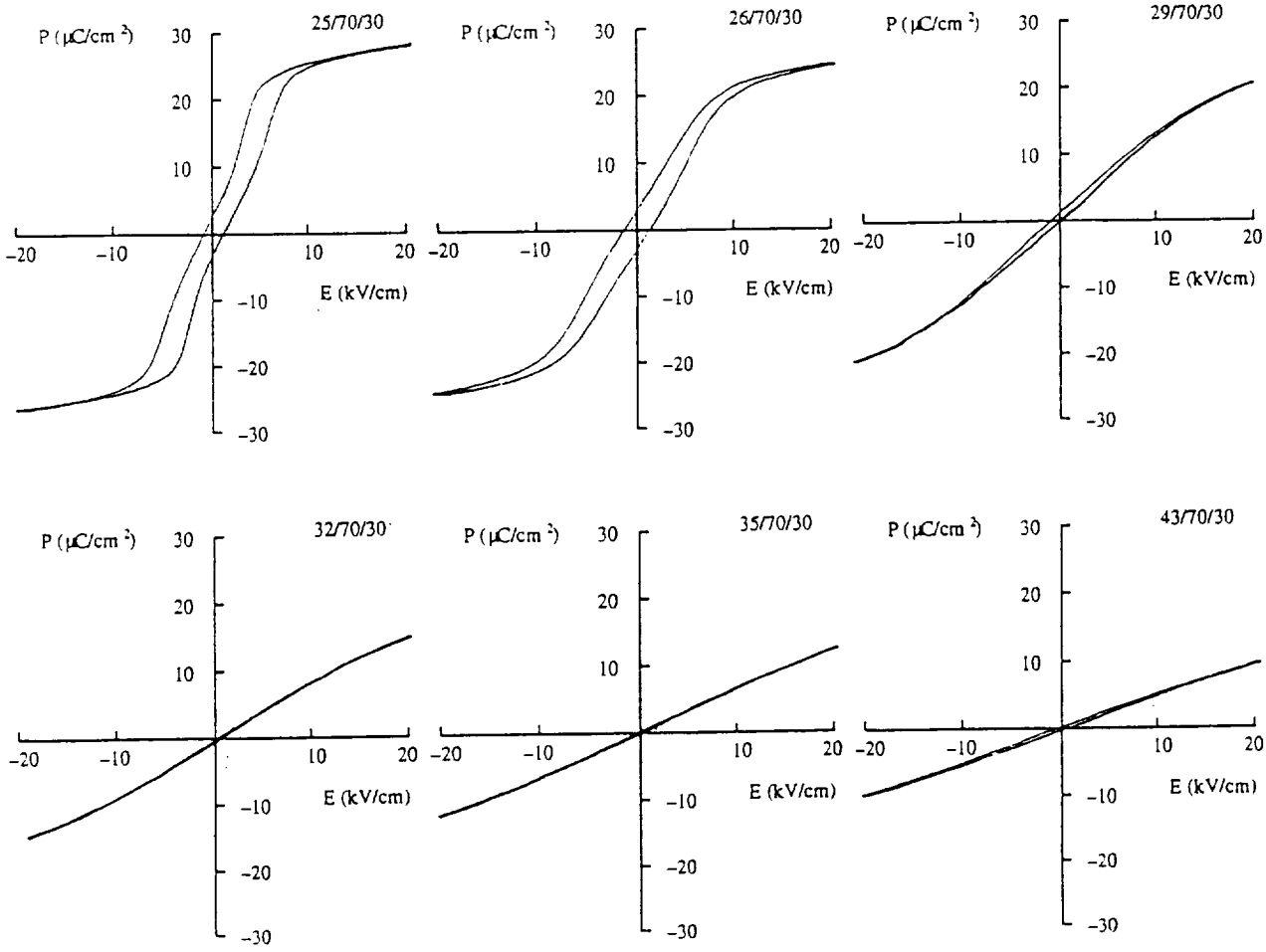

Figure 11. Relationship between polarization and electric field for the PBZT ceramics with constant Zr/Ti ratio.

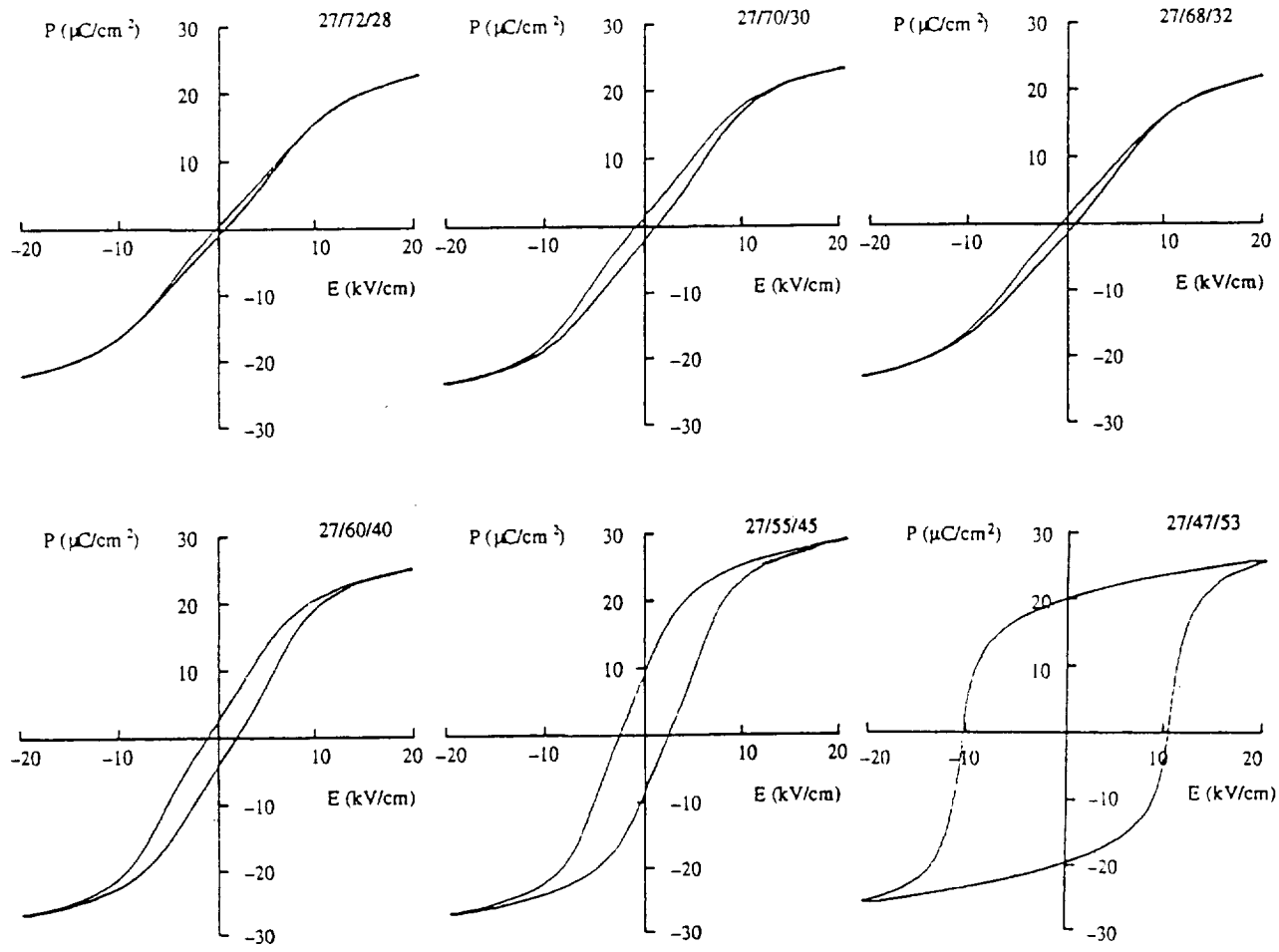

Figure 12. Relationship between polarization and electric field for the PBZT ceramics with constant Pb/Ba ratio.

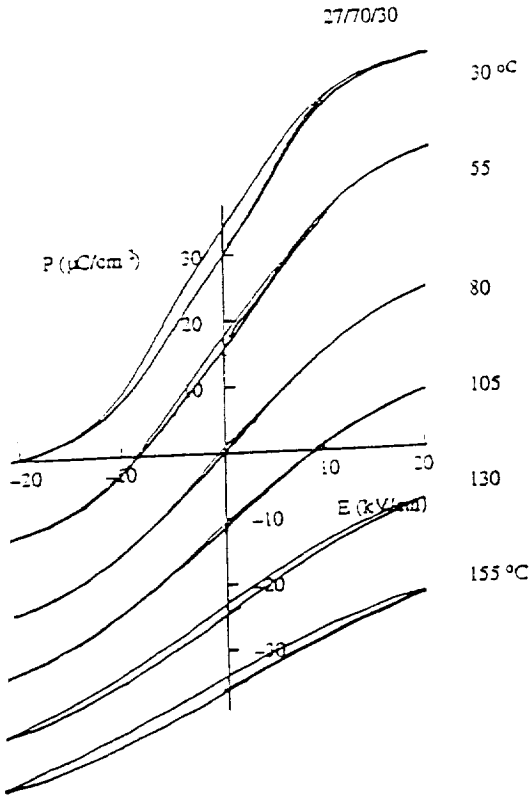

Figure 13. Variation of P–E relationship with temperature.

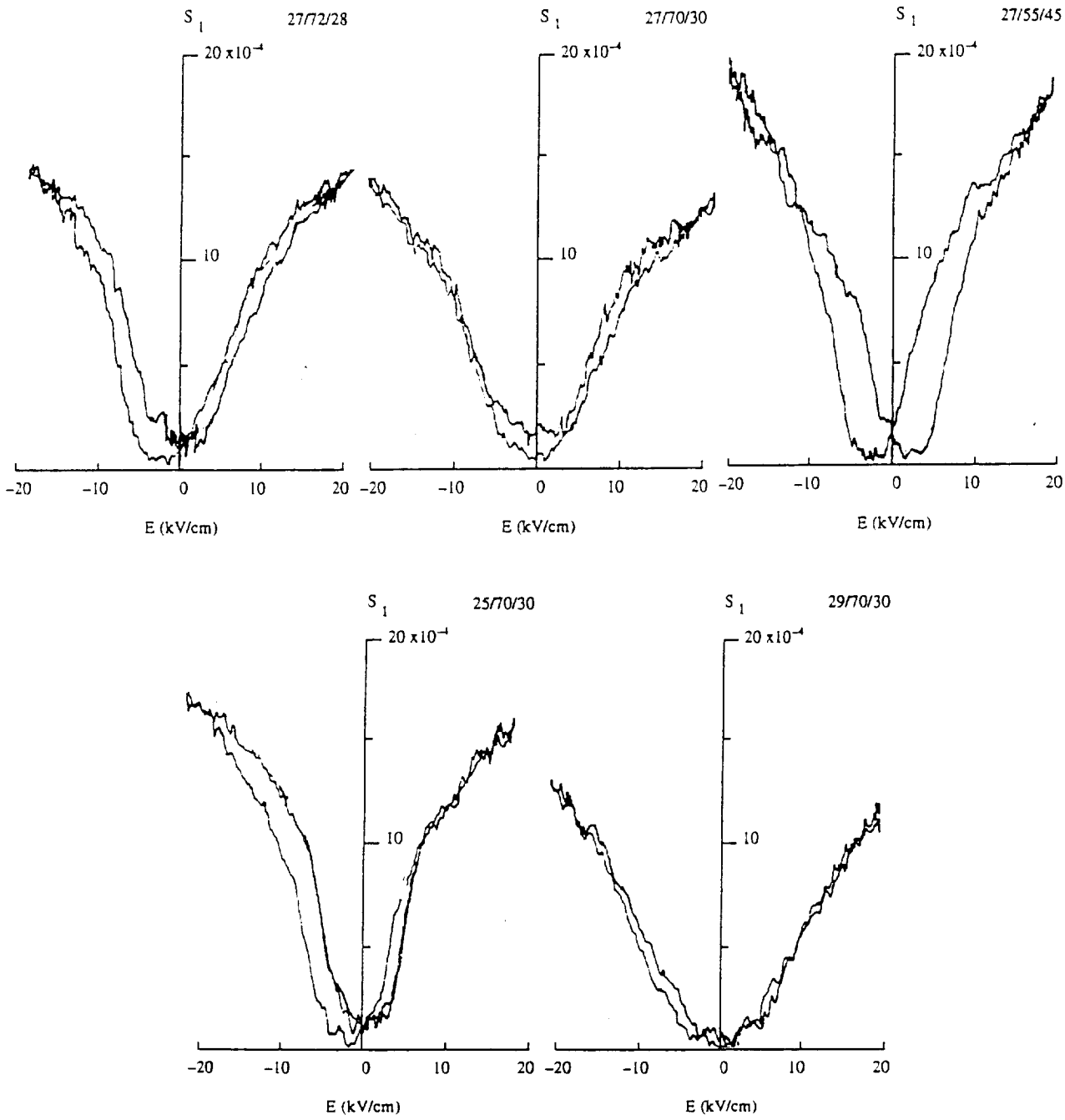

Figure 14. Variation of longitudinal strain with electric field for PBZT ceramics.

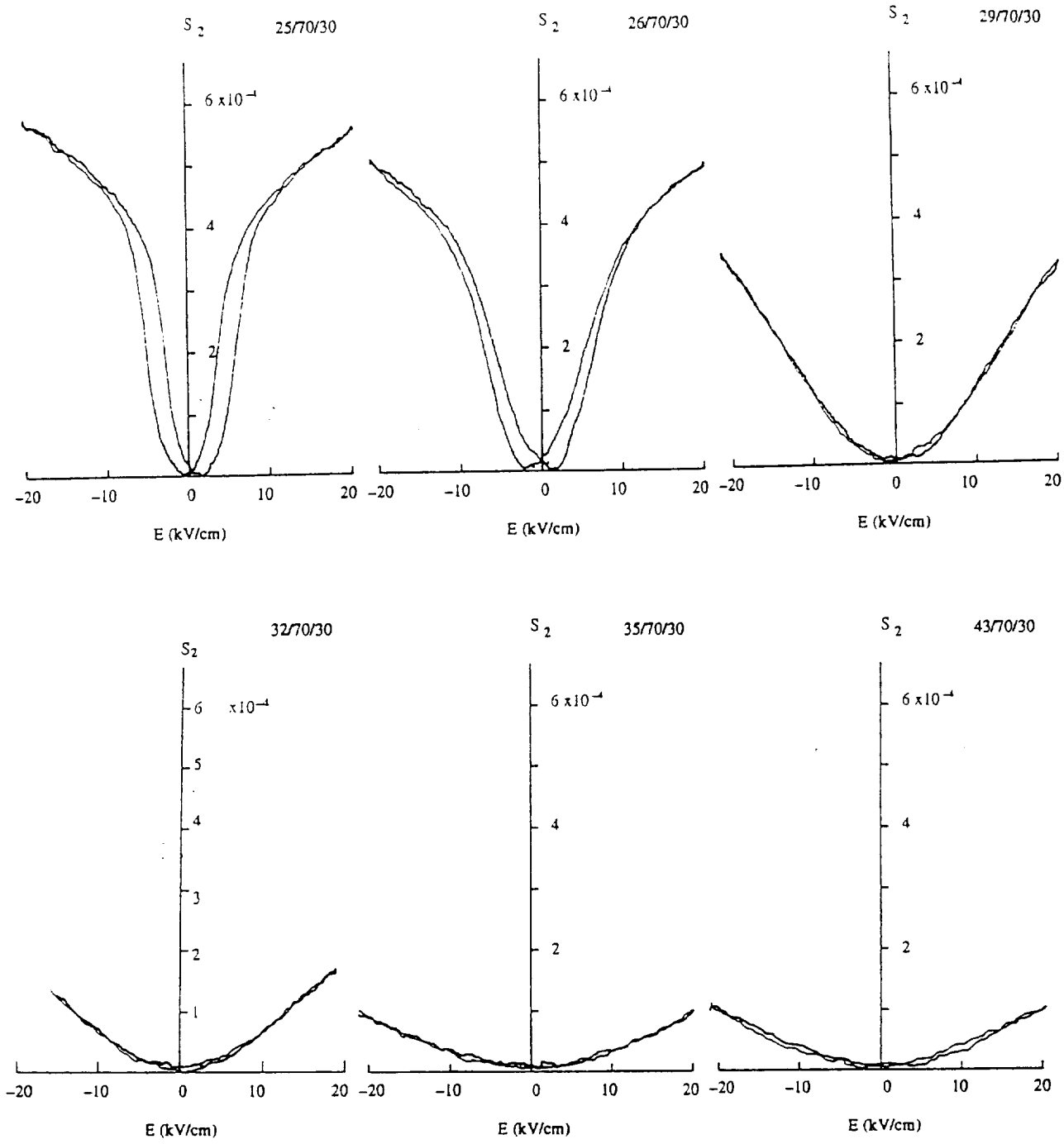

Figure 15. Variation of lateral strain with electric field for PBZT ceramics with constant Zr/Ti ratio.

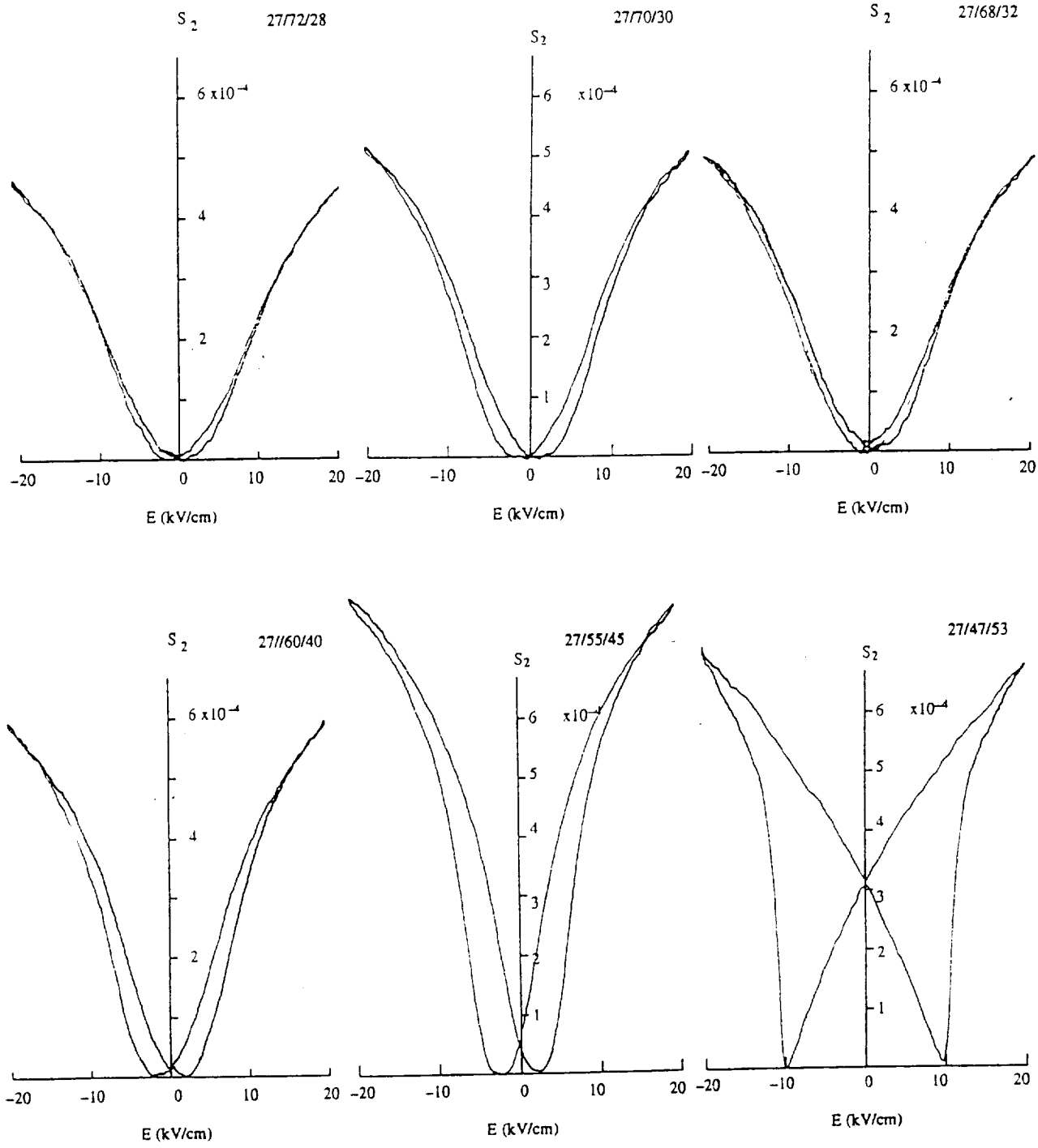

Figure 16. Variation of lateral strain with electric field for PBZT ceramics with constant Pb/Ba ratio.

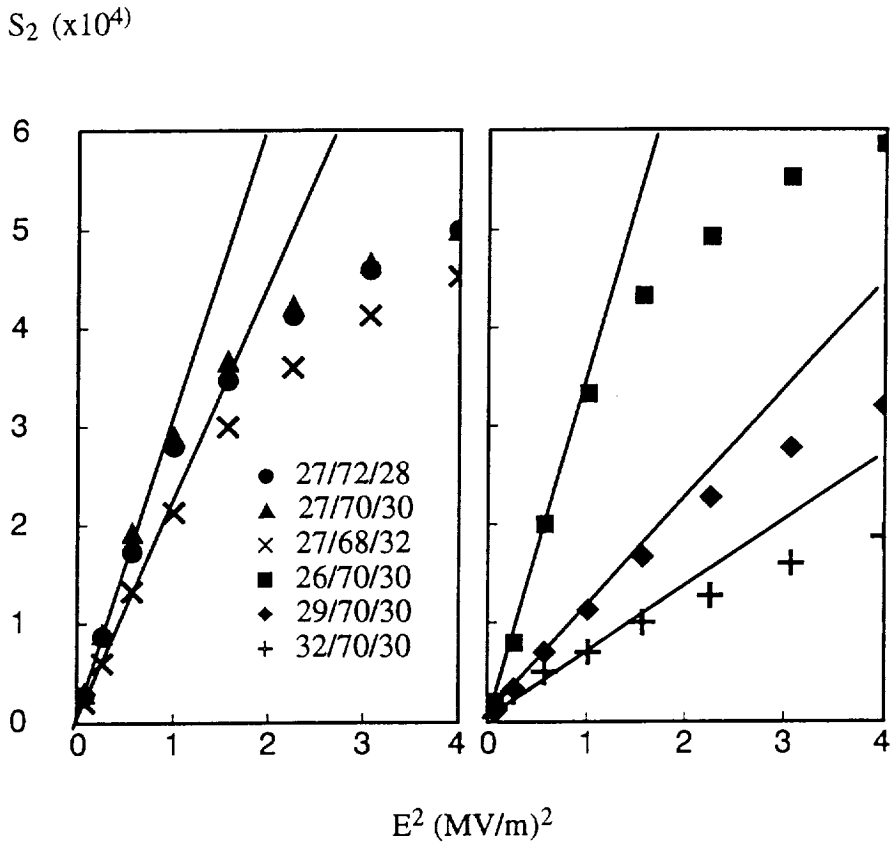

Figure 17. Plot of lateral strains against the square of electric field.

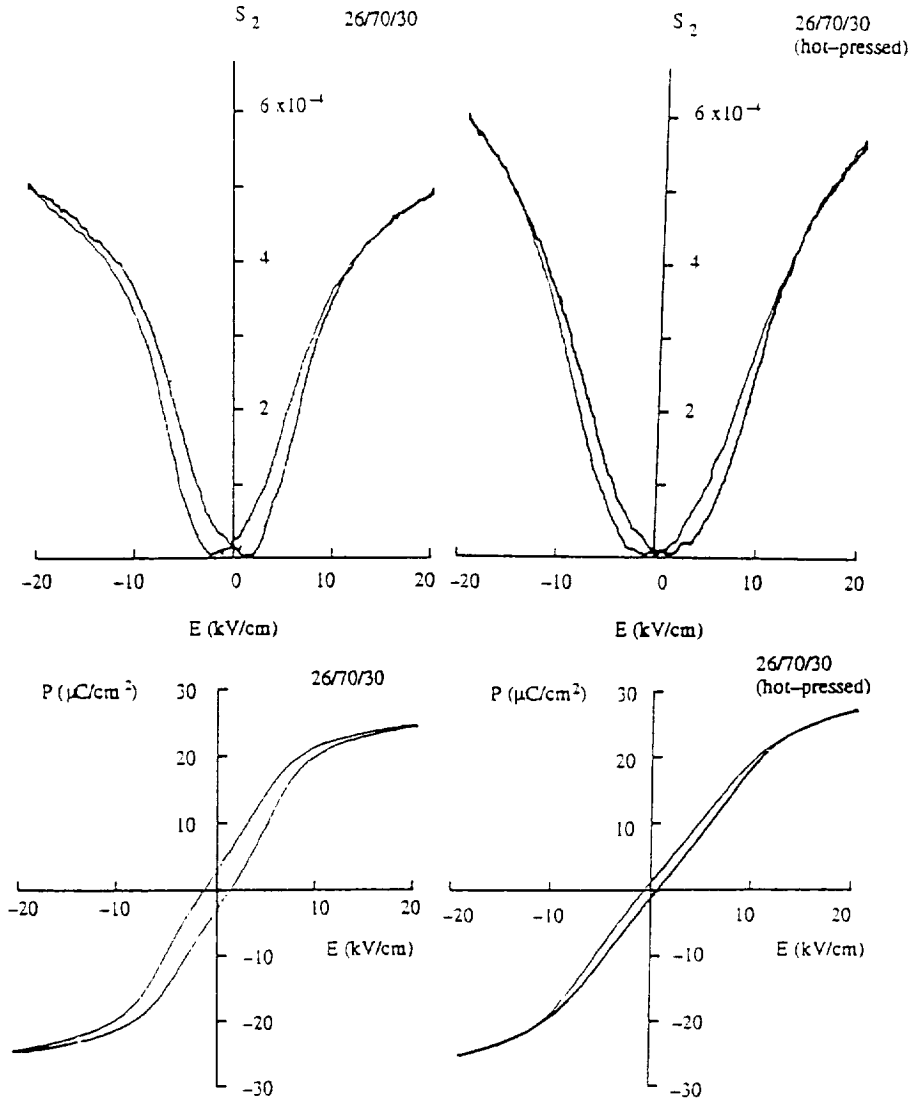

Figure 18. Influence of hot–pressing on the properties of PBZT ceramics.

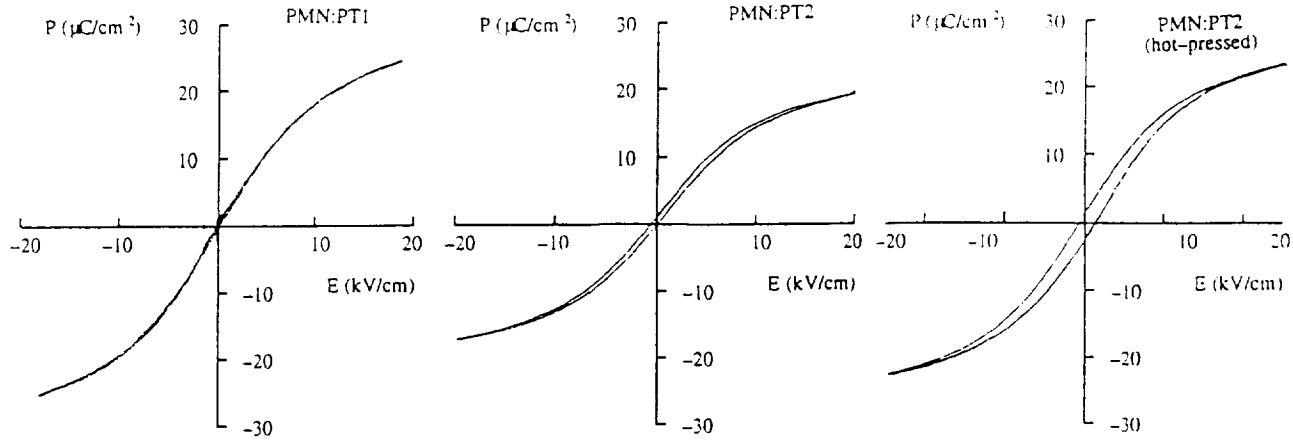

Figure 19. Relationship between polarization and electric field for PMN:PT ceramics.

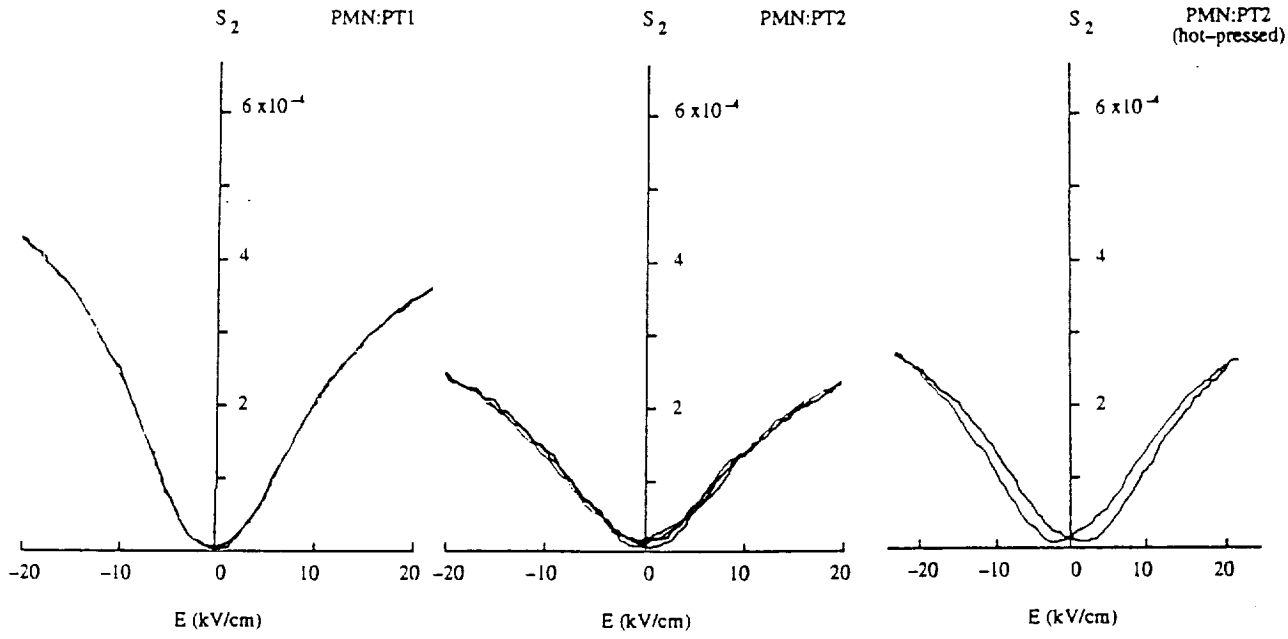

Figure 20. Variation of lateral strain with electric field for PMN:PT ceramics.

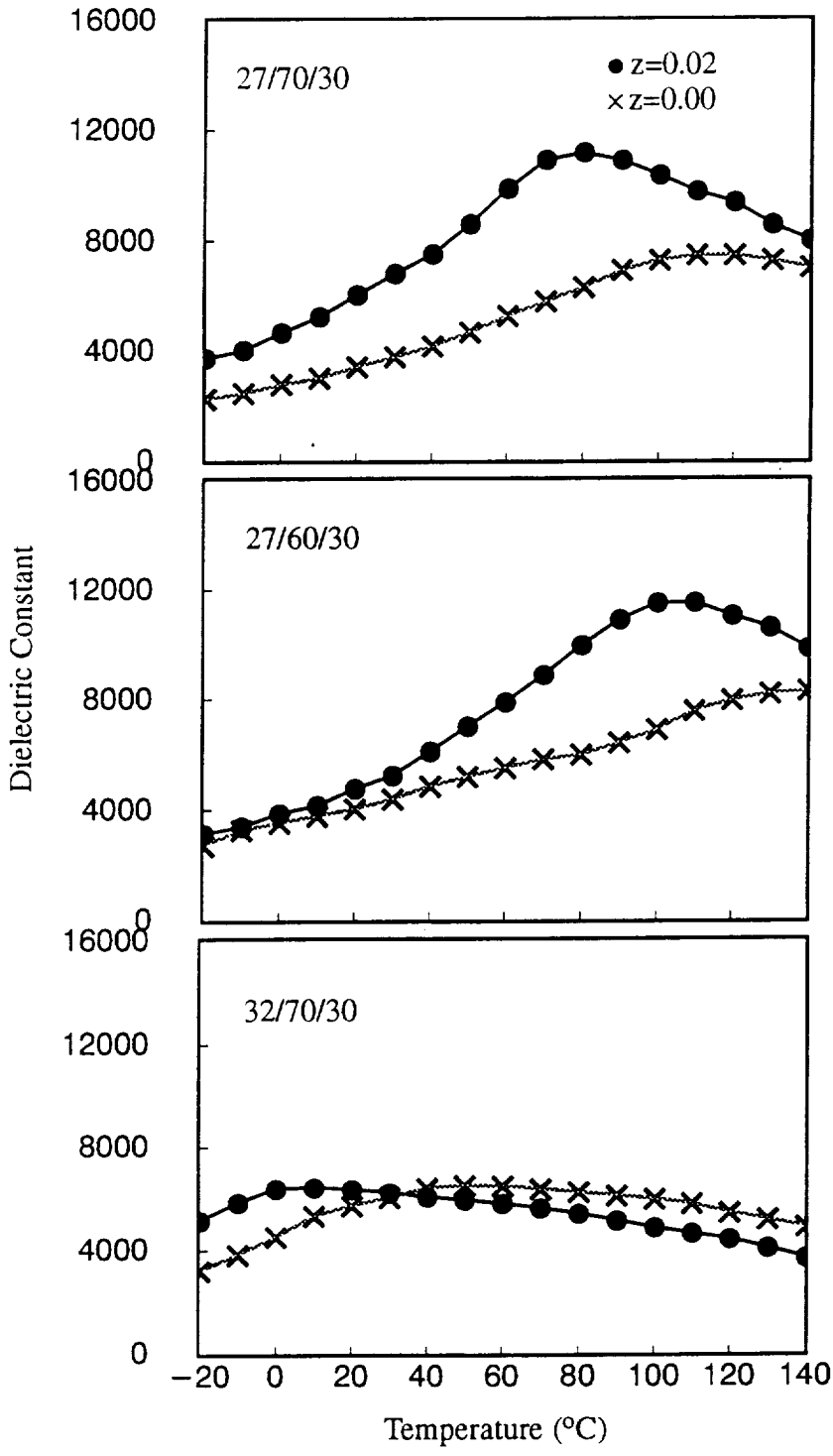

Figure 21. Influence of Bi_2O_3 additive on pure PBZT ceramics.

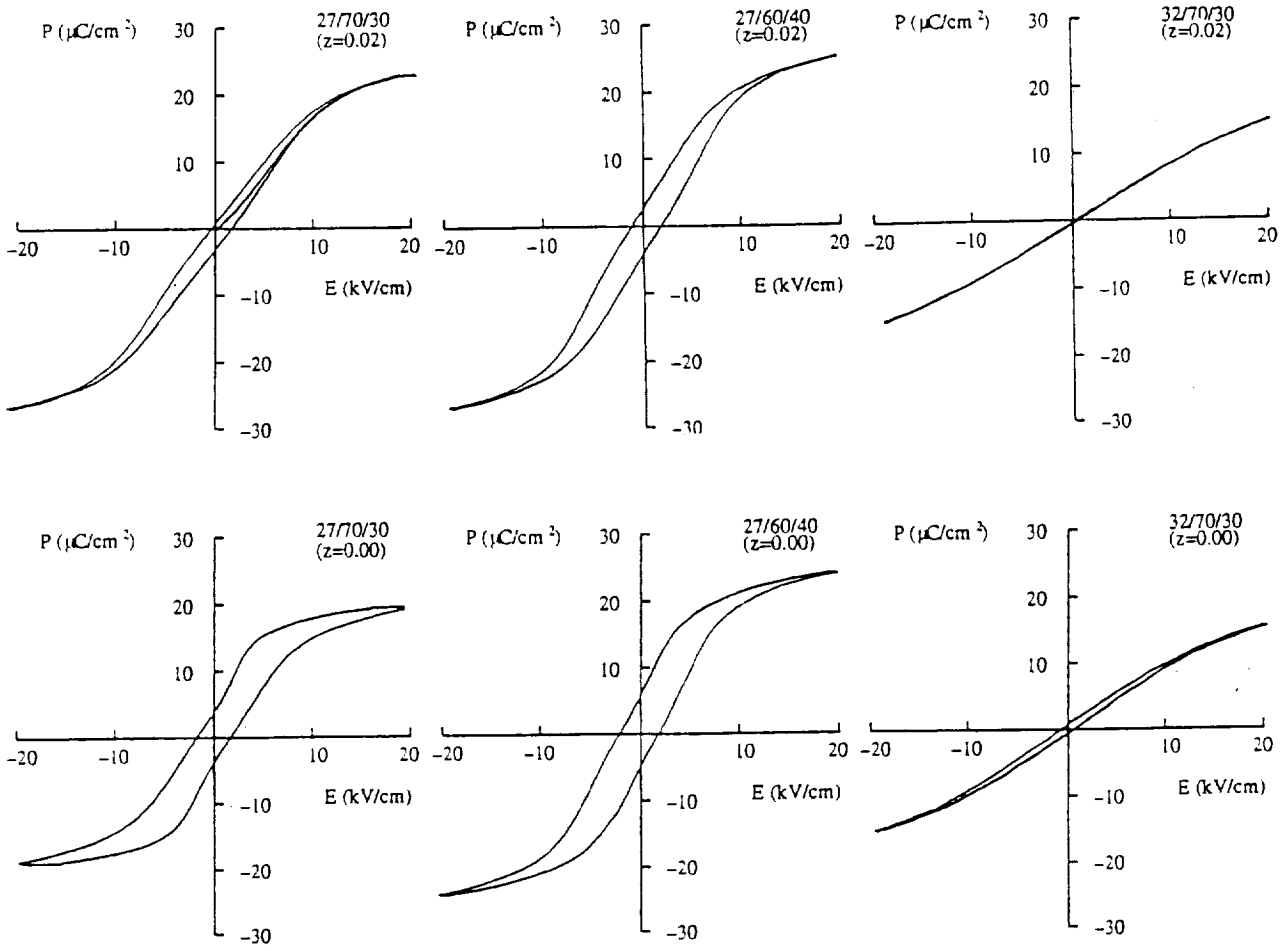

Figure 22. Comparison of P–E relationship of pure PBZT with Bi_2O_3–doped PBZT ceramics.

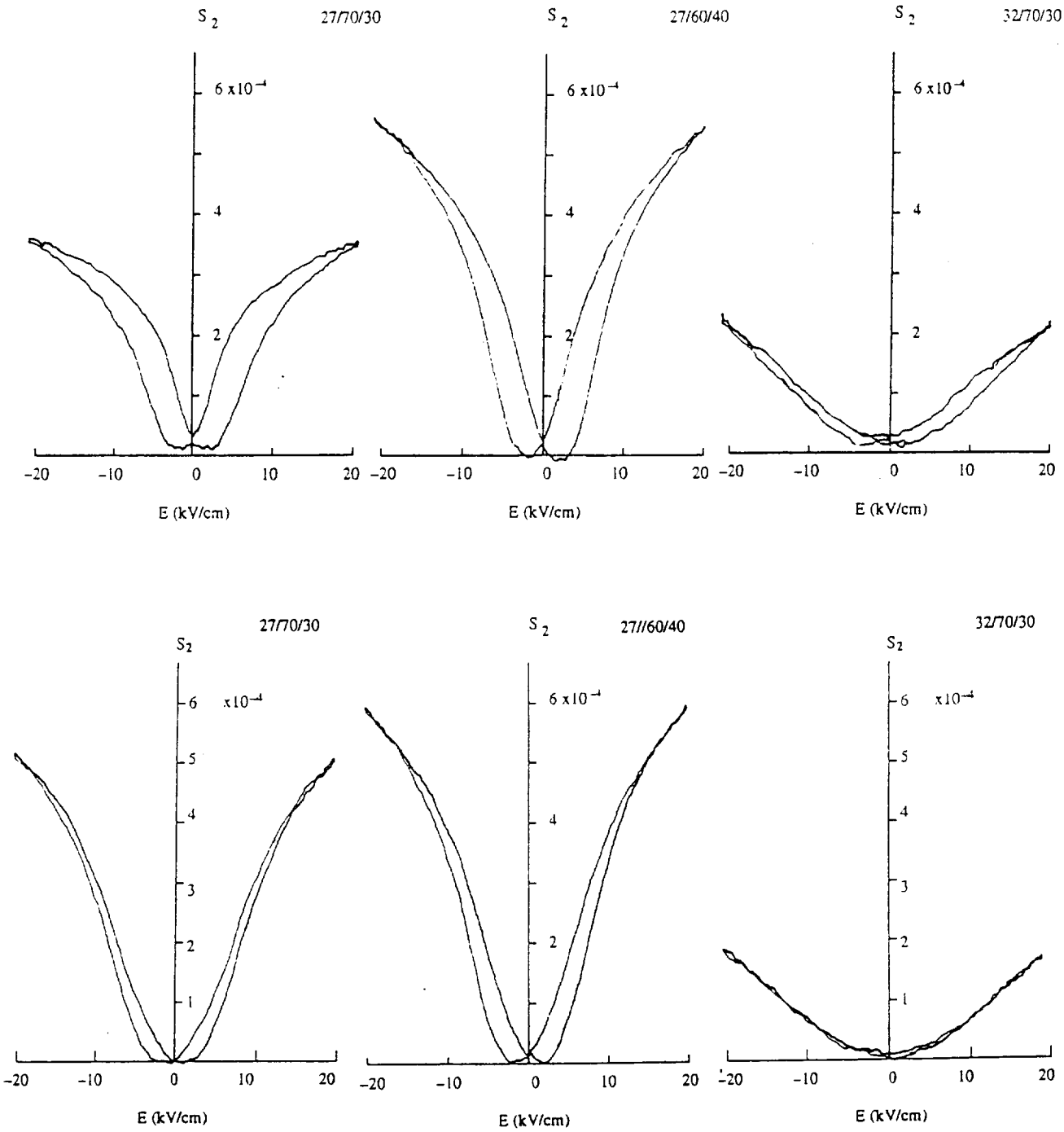

Figure 23. Comparison of S–E relationship of pure PBZT (above) with Bi_2O_3–doped PBZT ceramics.